Interfacial and Electrode Modifications in P$_3$HT:PC$_{61}$BM based

Organic Solar Cells:

Devices, Processing and Characterization

by

Sayantan Das

A Dissertation Presented in Partial Fulfillment
of the Requirements for the Degree
Doctor of Philosophy

Approved July 2015 by the
Graduate Supervisory Committee:

Terry Alford, Co-Chair
William Petuskey, Co-Chair
Daniel Buttry
Stephen Krause

ARIZONA STATE UNIVERSITY

August 2015

ABSTRACT

The inexorable upsurge in world's energy demand has steered the search for newer renewable energy sources and photovoltaics seemed to be one of the best alternatives for energy production. Among the various photovoltaic technologies that emerged, organic/polymer photovoltaics based on solution processed bulk-heterojunctions (BHJ) of semiconducting polymers has gained serious attention owing to the use of inexpensive light-weight materials, exhibiting high mechanical flexibility and compatibility with low temperature roll-to-roll manufacturing techniques on flexible substrates. The most widely studied material to date is the blend of regioregular P_3HT and $PC_{61}BM$ used as donor and acceptor materials. The object of this study was to investigate and improve the performance/stability of the organic solar cells by use of inexpensive materials. In an attempt to enhance the efficiency of organic solar cells, we have demonstrated the use of hexamethyldisilazane (HMDS) modified indium tin oxide (ITO) electrode in bulk heterojunction solar cell structure The device studies showed a significant enhancement in the short-circuit current as well as in the shunt resistance on use of the hexamethyldisilazane (HMDS) layer. In another approach a p-type CuI hole-transport layer was utilized that could possibly replace the acidic PEDOT:PSS layer in the fabrication of high-efficiency solar cells. The device optimization was done by varying the concentration of CuI in the precursor solution which played an important role in the efficiency of the solar cell devices. Recently a substantial amount of research has been focused on identifying suitable interfacial layers in organic solar cells which has efficient charge transport properties. It was illustrated that a thin layer of silver oxide interfacial layer showed a 28% increase in power conversion efficiency in comparison to that of the control

cell. The optoelectronic properties and morphological features of indium-free ZnO/Ag/MoOx electrodes was also studied. Organic solar cells on these composite electrodes revealed good optical and electrical properties, making them a promising alternative indium free and PEDOT:PSS-free organic solar cells. Lastly, inverted solar cells utilizing zinc oxide and yttrium doped zinc oxide electron transport was also created and their device properties revealed that optimum annealing conditions and yttrium doping was essential to obtain high efficiency solar cells.

DEDICATION

To my parents and my wife

ACKNOWLEDGMENTS

I consider it my privilege to acknowledge the help, assistance and support of the many individuals without whom this dissertation would not have been possible.

It is my honor to thank my research advisor Prof. Terry Alford for his constant guidance, support and invaluable suggestions during the course of my graduate study. I would also like to thank my co-advisor Prof. William Petuskey and for his support, assistance and guidance throughout my thesis work as well as being the chair of my thesis defense committee. I express my gratitude to Prof. Daniel Buttry and Prof. Stephen Krause for being in my committee, and taking the time and interest for evaluating my thesis work provide constructive feedback.

I thank Emmanuel Soignard, Barry Wilkens, David Wright, Kenneth Mossman and Tim Karcher at LE-CSSS for training and assistance with instrument usage. I would also like to thank my group members and ex-group members Zhao Zhao, Nazmul Hossain, Rajitha Vemuri, Jea-Young Choi, Hyung Woo Choi, Mandar Gadre and Anil Indluru. They have helped me with various discussions and experiments and have been a terrific group of graduate students to be with.

My special thanks to Sabarna Choudhuri, Prithwish Chatterjee, Joydeep Banerjee, Mrinmoy Saha, Tirthankar Bhattacharjee, Soumyawrit Manna, Baisravan HomChoudhuri, Arnab Dutta, Souvik Roy, Manas Chakrabarty and all my friends who have always been there to share my joys and sorrows along the way.

Last but not the least: I will never be able to thank in words those who are my immediate and extended family. My father Shyamal Kumar Das, mother Nupur Das, sister Nabamita Das, wife Ipsita Basu and many more who have always been there to support,

encourage and guide me. It is because of their love, that I have been able to achieve anything, if at all.

TABLE OF CONTENTS

LIST OF TABLES

LIST OF FIGURES

CHAPTER 1

INTRODUCTION

1.1   Fossil Fuels

The depreciating supply of today's main energy sources (oil, coal) will eventually lead us to replace most of the currently used power plants with renewable energy sources [1]. According to estimates, the global production of conventional oil will drop within the next few decades [2]. As a consequence, worldwide oil prices will then increase significantly thus favoring the utilization of various renewable energy sources such as solar energy, hydroelectric, tidal and wind energy systems [3].
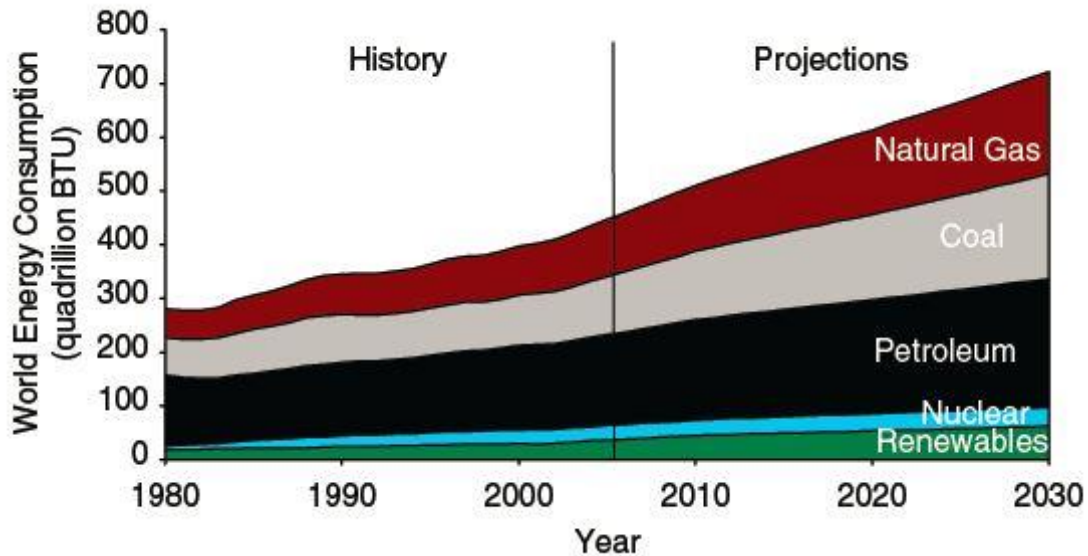
Figure 1.1   Estimation of world's energy consumption by the year 2030.

Reprinted with permission from Ref. 4.

Moreover, the significant rise of greenhouse gases like CO_2 in earth's atmosphere can be largely attributed to human activities, mostly by the use of fossil-fuels [4]. Every year, tonnes of carbon dioxide are put into the atmosphere, mainly by burning fossil fuel.

As a result of this increased concentration of carbon dioxide in the atmosphere the global mean surface temperature will rise by another 0.6-0.7°C by the year 2100 [5-7].
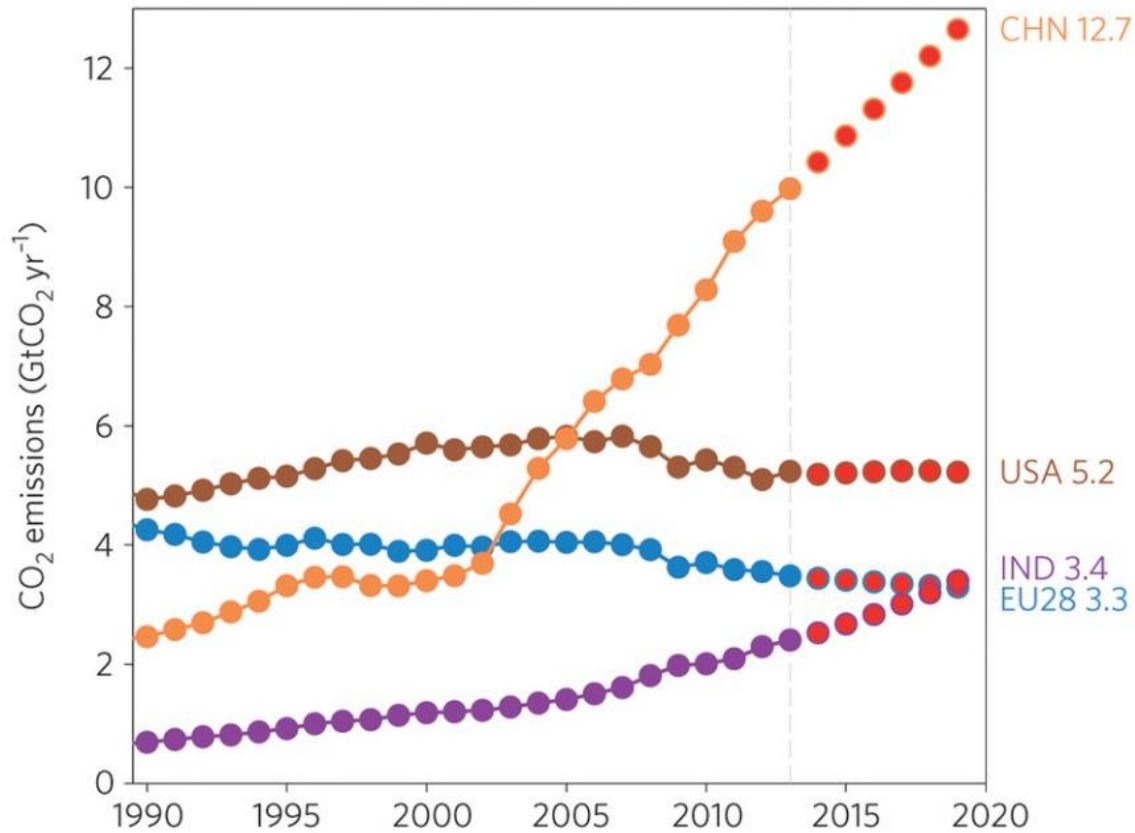
Figure 1.2   Carbon dioxide emissions from top four emitters of the world (China, USA, EU28 and India). Reprinted with permission from Ref 8.

1.2   Renewable energy sources

It turns out that renewable energy sources which neither run out nor have any significant adverse effects on our environment is the answer to the problems created by fossil fuels which unlike the latter is both abundant and environment friendly. The power plants which use wind, tidal or wave energy of water, geothermal energy or solar radiation completely rely on the local supply of their primary energy source. Thus, the amount of

power they can supply over a longer period often depends on geographical as well as weather conditions. It has become necessary to realize that the installation of these power systems should be favored only if they supply more energy throughout their lifetime than they have consumed during their production, installation and maintenance. Therefore it has become imperative to come up with low cost technologies for harnessing energy from renewable sources. Compared to hydro, wind, tide, and geothermal energy sources, solar energy is the most important renewable energy source due to the large amount of energy originating from the sun and availability of sun's light in most of the places on earth.

1.3   Inorganic solar cells

Ever since the first silicon solar cell was recognized in 1954, an enormous amount of effort has been put to improve their power conversion efficiency. The best laboratory efficiency of mono-crystalline silicon solar cells reported to date is 25.6 % [9]. Currently, 90 % of the solar cell market involves silicon solar cells which includes monocrystalline, polycrystalline and amorphous silicon. The technology for manufacturing high efficiency silicon solar cells has already been established, and therefore future research interest lies in the field of cost reduction these modules. Crystalline silicon (indirect band gap material) requires thickness of around 100 µm to efficiently harvest about 90% of the incident solar radiation [10, 11]. Moreover, efficient charge collection requires the thick silicon to have high purity and few structural defects. Hence, intensive energy input is required to produce extremely pure and mono-crystalline or multi-crystalline silicon, which results in the costly module price.

On the contrary CdTe and $CuInGaSe_2$ (direct band gap semiconductor) requires a thickness of only 1 µm [10]. The best laboratory efficiencies of CdTe and CuInSe2 cells is

around 21% [9]. Nevertheless, these cells are fabricated using a vacuum process and requires high temperature processing of around 400~600 °C. The maximum thermodynamic efficiency for a single absorber solar cell was estimated to be around 31 % by Shockley and Queisser in 1961 [12]. However, multi-junction solar cells consisting of multiple absorbers is developed and the best efficiency reported to date is 46 % [9]. These high efficiency multijunction solar cells are mostly used for advanced satellite application owing to their high production cost.

1.4   Organic solar cells

Organic solar cells (OSC) based on organic molecules/polymers have become an important field of research in the recent times because of their simpler processing at much lower temperatures (25-200ºC) than the above mentioned silicon cells [13-15]. Another interesting alternative to inorganic cells is given by the semiconducting organic molecules/polymers, which combine the opto-electronic properties of inorganic semiconductor materials along with their excellent mechanical and processing properties [16-18]. These materials are can be processed from solution at room-temperature onto flexible substrates using simple, cheaper deposition methods like spin or blade coating or roll-to-roll printing [19-22].

Despite all the above discussed benefits that organic materials possess, a lot of challenges need to be overcome to make them commercially available. The organic molecules/polymers utilized in organic electronic devices possess a strong covalent sigma and pi bonds within individual molecules/polymers but only very weak van der Waals type interaction among each other [13]. Thus, there exists a strong orbital delocalization within molecules/ polymer chains but very slight orbital overlap between individual

4

molecules/polymers [13]. As a result, the various processes occurring in organic solar cells which includes light absorption, exciton diffusion and charge transport are all associated to the localized interactions of individual orbitals rather than delocalized bands [23]. In these materials, a photon excites electrons from the highest occupied molecular orbital (HOMO) to the lowest unoccupied molecular orbital (LUMO). The isolated nature of these molecular energy levels results in relatively lower absorption which is one of the major drawbacks in the case of organic solar cells [23].

1.5 Motivation and outline of thesis

A great deal of effort has been put by scientists and researchers to increase the efficiencies of OSC by developing and introducing new photoactive materials, owing to the availability of simple synthesis and low cost fabrication methods [24-26]. Most of these OSC devices were fabricated utilizing indium tin oxide electrodes because of their high transparency in the visible region and low room temperature resistivity [27, 28]. However, development of a new transparent electrode system for photovoltaic devices to replace indium tin oxide (ITO) is of utmost importance due to the scarcity of indium which will eventually increase the fabrication costs of future OSCs or hybrid solar cell [29-31]. Transparent composite electrode (TCE) comprising of oxide/metal/oxide thin films has been studied with an expectation to increase conductivity without major transmittance loss [32-34]. A lot of these research utilizes silver (Ag) as the embedded layer because Ag has the lowest room temperature bulk resistivity among all metals [35]. Another important material used in OSC is poly(3,4-ethylenedioxythiophene):poly(styrenesulfonate) (PEDOT:PSS) used as hole transport layer (HTL) in OSCs because of its numerous advantages including surface planarization of ITO and high optical transparency [36].

However, the acidic nature of PEDOT:PSS causes migration of indium from ITO anode into the PEDOT:PSS layer and also into the active layer of OSCs [37]. This process reduces the lifetime of the solar cells over a period of time. In order to address this problem, many studies on metal-oxide HTLs like WO_3 [38], $NiOx$ [39], V_2O_5 [40] and MoO_3 [40] as an alternative to PEDOT:PSS have been studied. Nevertheless, these oxide materials are mostly deposited under high vacuum and thus effective low cost solution processing is still unavailable.

In this dissertation, the primary focus will be about device engineering to realize efficient OSC based on regioregular poly(3-hexylthiophene) (P3HT) used as donor (D) and fullerene derivative [6,6]-phenyl-C61-butyric acid methyl ester ($PC_{61}BM$) as an electron acceptor (A). A lot of effort was taken to develop new hole transport and electron transport materials as well as a new trilayered electrode system with a potential to replace the ITO based electrodes. Chapter 2 illustrates the background and operation principle of organic solar cells. Chapter 3 discusses an attempt to enhance the efficiency of OSC by the use of hexamethyldisilazane (HMDS) modified indium tin oxide (ITO) electrodes in bulk heterojunction solar cell structure. Chapter 4 shows the effect of replacing PEDOT:PSS hole transport layer by solution processed CuI layer. Chapter 5 focusses on the utilization of a silver oxide interfacial layers in organic solar cells with improved efficiency. Chapter 6 explores the optoelectronic properties and morphological features of indium-free ZnO/Ag/MoOx electrodes and their utilization in indium free, PEDOT:PSS free OSC. Chapter 7 deals with the optimization of annealing and yttrium doping concentration in zinc oxide acting as an electron transport layer in $P_3HT:PC_{61}BM$ based organic solar cells. Finally, chapter 8 provides a summary of conclusions and future outlook.

CHAPTER 2

ORGANIC SOLAR CELLS: AN OVERVIEW

2.1   Photovoltaic effect in organic semiconductors

Before delving deep into organic semiconductors and their uses in organic solar cells the concept of photovoltaic effect needs to be understood in brief. Photovoltaic effect was first reported by Alexandre-Edmond Becquerel (1820-1891) a French physicist who studied the solar spectrum, optics electricity and magnetism. A solar cell is a photovoltaic device which converts solar energy into electric power by the generating electrons (negatively charged) and holes (positively charged) as well as transporting these charges through an external electric circuit. When light of energy higher than the band gap of a semiconducting material is absorbed by the same material, electrons are excited from lower energy states to higher energy states within the material. However, these excited electrons relax back quickly to their ground state. On the other hand in a solar cell device, these excited electrons are pulled away and fed into an external circuit before they can relax. The excited electrons thus generated possess an electron motive force (emf) and is driven through a load in the external circuit to do electrical work.

Organic semiconductors contains unsaturated carbon carbon bonds, thus they have carbon atoms which are sp^2 or sp hybridized. The sp^2 hybridized orbitals form a strong sigma bond with neighboring carbon or other elements [1]. The pure p_z orbital of carbon forms delocalized pi molecular orbitals along the backbone of organic semiconductors. In comparison to the electrons in sigma orbitals, the pi electrons are loosely bound and are highly polarizable *i.e* can move easily along the backbone of the molecules/polymers [2]. These pi molecular orbitals play an important role in determining the optoelectronic

7

properties of organic semiconductors. In organic semiconductors the energy difference of the highest occupied molecular orbital (HOMO) and lowest unoccupied molecular orbital (LUMO) states the optical bandgap energy of organic semiconductors [2, 3]. In organic semiconductors, charge carrier transport takes place along the frontier energy level (HOMO and LUMO) levels through overlapped π molecular orbitals with adjacent molecules. Intermolecular π-π overlap is governed by molecular structures, constituents, and molecular packing. Long range charge carrier transport is influenced by the crystallinity of organic semiconductor [4]. Optical bandgap of a material governs the minimum photon energy required for excitation of electrons from the HOMO to the LUMO. In most organic semiconductors, the optical band gap lies in the range of 1.4~3.0 eV [3]. Hence, their intrinsic carrier density is almost negligible at room temperature. Nevertheless, they can be doped with extrinsic dopants to improve their conductivity. Charge carrier mobility of organic semiconductors lies in the range of 10^{-7}~10^{-4} $cm^2V^{-1}sec^{-1}$, in contrast to crystalline inorganic semiconductor materials which have a charge carrier mobility in the range of 10^2 ~ 10^4 $cm^2V^{-1}sec^{-1}$ [5-7].

Light incident on a photoactive layer undergoes several processes such as absorption by the layer, reflection from the surface and transmission through the material. Reflected or transmitted light do not produce electrical power and are contemplated as losses. The light absorbed by the photoactive layer contributes to generation of electrical power. The absorption of light by different materials is calculated by Lambert-Beer law as shown by equation 2.1, where I_o is the light intensity of incident beam, c is the concentration gradient, α is the absorption coefficient of the material and t is the thickness of the material that is tested [8].

$$I = I_0 e^{-\alpha ct} \qquad\qquad 2.1$$

Organic semiconductor materials have relatively high absorption coefficients (typically$\geq 10^5$ cm^{-1}), which partly balances low mobilities, giving high absorption even in devices which are less than 100 nm thick [9]. The energy of the photon absorbed in the material is given by equation 2.2, where h is Planck constant, c is speed of light in vacuum, λ is the wavelength of the light in nm.

$$E_{ph}(eV) = \frac{hc}{\lambda} = \frac{1240(nm)}{\lambda(nm)} \approx E_g \qquad\qquad 2.2$$

The photoactive layer after absorption of light generates exciton [10]. When a light photon whose energy is higher than the band gap energy of the photoactive layer ($E_{ph} \geq E_g$) is absorbed, electrons are excited from the valence band or HOMO to the conduction band or LUMO creating holes in the HOMO level. In an exciton the electron and hole pair are still bound to each other by Coulombic force of interaction, hence it becomes obligatory to overcome the binding energy and separate the charge carriers [10]. Excitons can be of two types namely Frenkel or Wannier-Mott type exciton [11]. Frenkel excitons are firmly bound to each other and usually occurs in organic semiconductors because of their low dielectric constant [2]. The exciton binding energy values can be as high as 1 eV and localized radius range of 1 nm can be obtained in organic materials [2]. On the other hand, Wannier-Mott excitons are feebly bound to each other and are typically seen in inorganic semiconductors with high dielectric constant [11]. Their binding energies are around 100 meV and delocalized exciton radius range of 10 nm [11]. The different types of excitons are illustrated in Fig. 2.1.
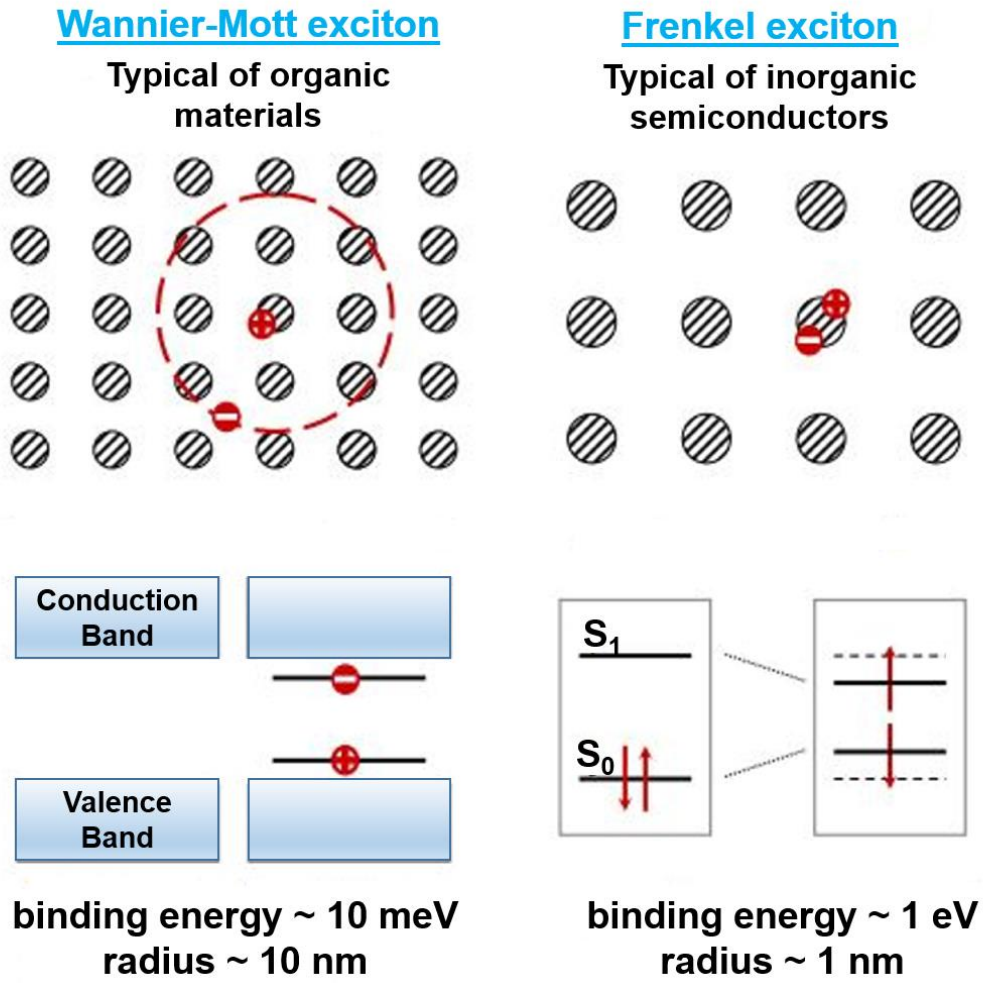
Figure 2.1   **Schematic of (a) Wannier Mott (b) Frenkel exciton [11]**

In organic solar cell devices, exciton dissociation usually occurs at donor/acceptor (D/A) interface. In organic solar cells, the exciton diffusion at the interfaces is limited by short exciton diffusion length. Exciton diffusion length L_D is given by the diffusivity D, and carrier lifetime τ of organic semiconductors as shown in equation 2.3.

$$L_D = \sqrt{D\tau} \qquad\qquad 2.3$$

In comparison to the crystalline, inorganic semiconductors, the excitons in organic semiconductors have relatively smaller diffusion length [12, 13]. These excitons constitutes a vital intermediate in the conversion of solar energy to electrical energy processes, and usually high electric fields are essential to dissociate them into free charge carriers, which are the anticipated ultimate products in photovoltaic process.

With the aim of generating free electron and hole, the exciton is required to travel to the D/A interface where they gets dissociated and then travel towards the electrode. A lot of theories have been proposed on the dissociation mechanism of electron-hole pair at donor/acceptor interfaces; however the most widely accepted one states that the electron-hole pair dissociates by the excess energy of ΔE_{LUMO}-E_B, where ΔE_{LUMO} is the difference in LUMO energies between donor and acceptor, and E_B is the exciton binding energy. [14]. It must be noted here that, strong intermolecular interaction and high crystallinity in organic materials is necessary for efficient charge dissociation. Additionally, the rate of recombination must be slow as compared to the rate of dissociation process for efficient charge carrier collection. At the D/A interfaces, exciton dissociation occurs and the charge carriers travel through each material until they reach to their respective electrodes. Thus, bound electron and hole pairs should overcome the recombination of charge carriers for efficient charge transport. Recombination is the process when electrons in the conduction band or LUMO fall back to the valence band or HOMO, and combine with holes, respectively. The different recombination processes are classified as radiative, Auger and Shockley-Read-Hall (SRH) recombination. The photo-generated charge carriers after exciton dissociation are transported by a built-in electric field or drift process as well as by

11

diffusion process. After the charge carrier dissociation process, free electrons and holes can be collected at the corresponding electrodes to generate electricity.

2.2 Organic solar cell materials

Organic semiconductor materials includes organic dyes, conjugated polymers and molecular materials which can show n or p-type semiconducting properties. They have high optical absorption coefficient and thus utilizes tiny amounts, making them suitable candidates for the production of very thin solar cells. Moreover, their expected ease of large scale manufacturing at relatively low temperatures and cost provides them with an added advantage from fabrication point of view [15-24]. Organic materials are deposited by both solution as well as vacuum assisted processes. In general, polymers are processed from solution whereas small organic molecules are vacuum-deposited. In literature, highly efficient organic solar cells are fabricated from atleast two different materials with dissimilar electron affinity. Under illumination, the material with lower electron affinity (donor) donates electron to the materials with high electron affinity (acceptor). Few examples of small molecules used in fabricating organic solar cell devices are metal phthalocyanines and pentacene which typically acts as donor materials, whereas, fullerene and perylene derivatives are typical acceptor materials [2]. Figure 2.2 illustrates the molecular structures of molecules used in organic solar cell devices deposited by thermal evaporation.
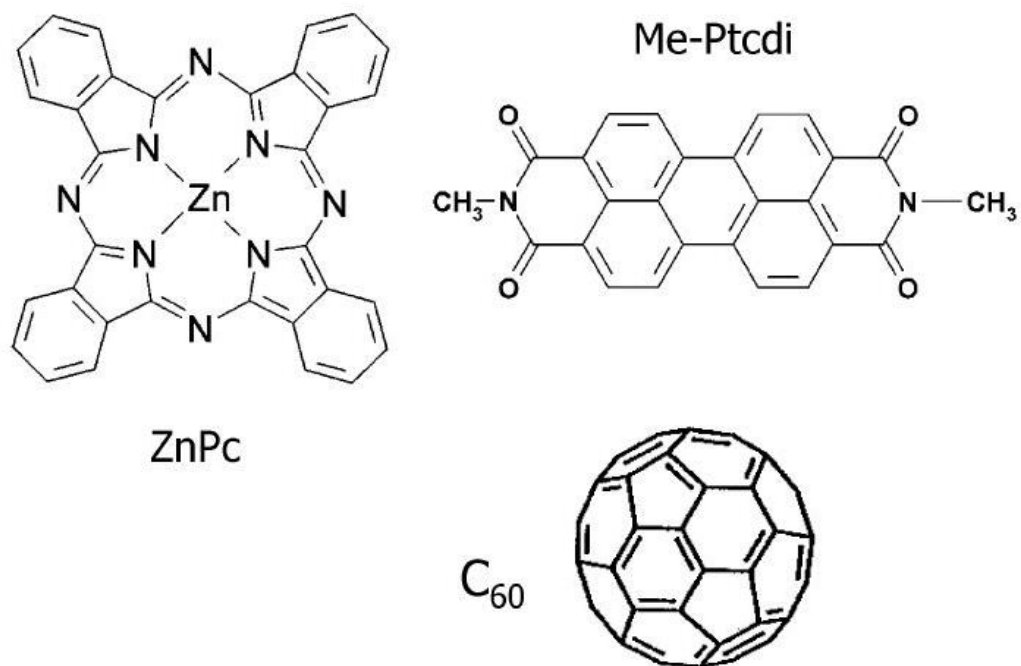
Figure 2.2 **Commonly used organic molecules deposited by evaporation in organic solar cells: ZnPc (zinc-phthalocyanine), Me-Ptcdi (N,N'-dimethylperylene-3,4,9,10-dicarboximide), and the buckminster fullerene C_{60}. Reprinted with permission from Ref 2.**

In case of polymers, poly(3-hexylthiophene) (P_3HT) and poly(2-methoxy-5-(3',7'-dimethyl-octyloxy))-p-phenylene vinylene (MDMO-PPV) are extensively used as donor material, while (6,6)-phenyl-C61-butric-acid ($PC_{61}BM$) is used as an acceptor. Figure 2.3 shows molecular structures of polymers used in organic solar cell devices.

MDMO-PPV   P3HT   PFB

CN-MEH-PPV   PCBM   F8BT
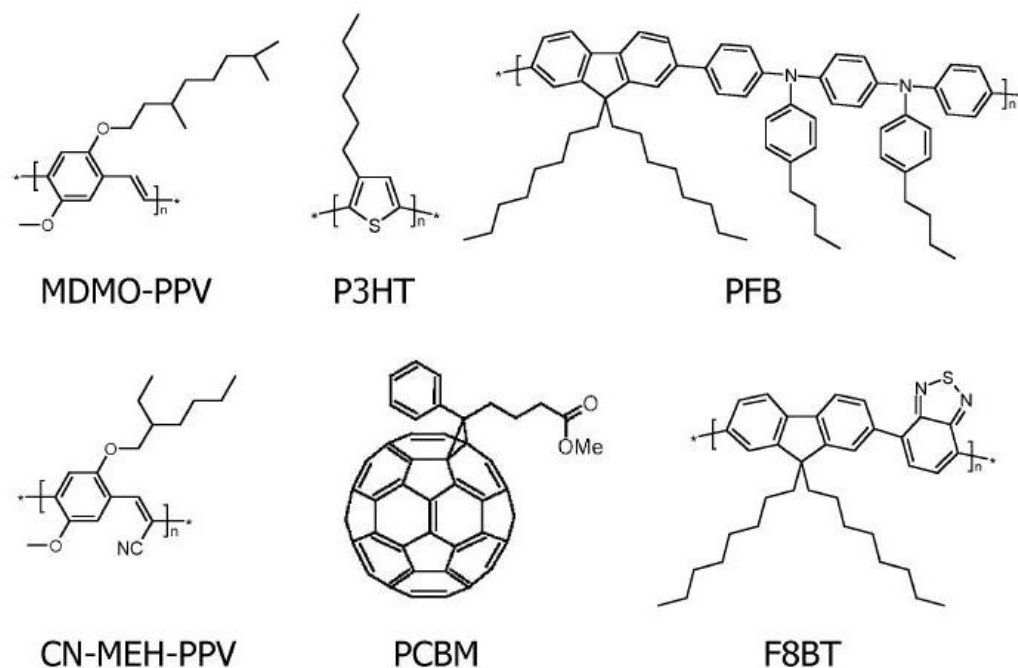
Figure 2.3   **Upper row: the *p*-type hole conducting donor polymers MDMO-PPV (poly[2-methoxy-5-(3,7-dimethyloctyloxy)]-1,4-phenylenevinylene), P3HT (poly(3-hexylthiophene-2,5-diyl) and PFB (poly(9,9'-dioctylfluorene-co-bis-*N,N'*-(4-butylphenyl)-bis-*N,N'*-phenyl-1,4-phenylenediamine). Lower row: Electron conducting acceptor polymers CN-MEH-PPV (poly-[2-methoxy-5-(2'-ethylhexyloxy)-1,4-(1-cyanovinylene)-phenylene) and F$_8$TB (poly(9,9'-dioctylfluoreneco-benzothiadiazole) and a soluble derivative of C$_{60}$, PC$_{61}$BM (1-(3-methoxycarbonyl) propyl-1-phenyl[6,6]C$_{61}$). Reprinted with permission from Ref 2.**

2.3   Testing of solar cells

The efficiency of solar cells are tested in a special laboratory environment and for that the air mass concept needs to be understood properly. The air mass concept takes into account for the light scattering and absorption of particular wavelengths of light by the different atmospheric species [25]. Air mass (AM) is defined as the equation (2.1), where θ is the zenith angle or the angle of sunlight path from an overhead sun [26]:

$$AM = \frac{1}{\cos\theta} \qquad\qquad 2.4$$

The sun is a blackbody radiating at a temperature of 5760 K [26] and the spectral radiance as a function of wavelength is characterized by Plank's radiation formula. This is the light power distribution experienced by extra-terrestrial objects and is referred to as air mass (AM) 0 distribution. Conventional standard conditions are AM 1.5 global (AM 1.5G) and AM 1.5 direct (AM 1.5D) for terrestrial uses [25]. Figure 2.4 shows the solar spectral irradiances generated by American society for testing and materials (ASTM) under AM 0, AM1.5G and AM 1.5D conditions.
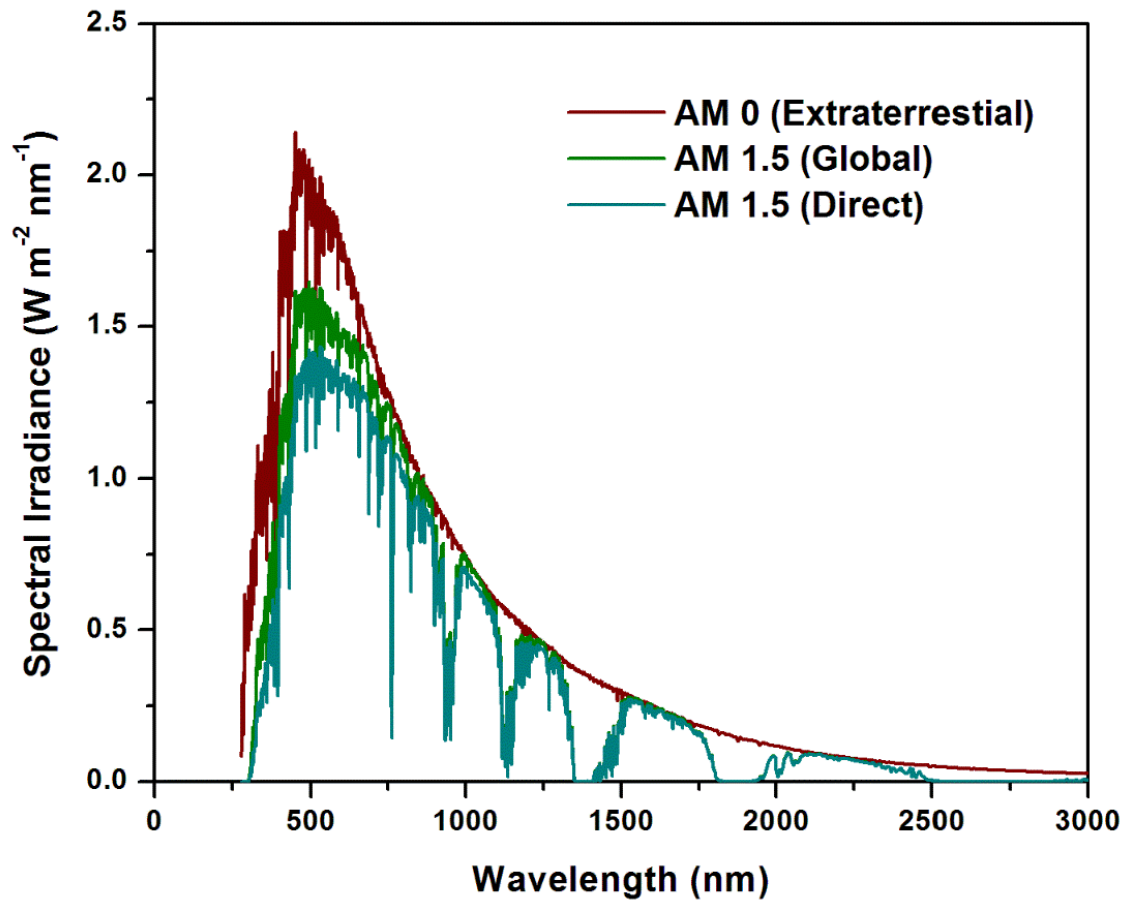
Figure 2.4   **Standard reference for solar spectral irradiances generated by American society for testing and materials (ASTM). [Courtesy of the American society for testing and materials]**

2.4 Device parameters of solar cells

The device parameters of solar cell devices are extracted from the current density-voltage (J-V) characteristics measured with simulated illumination condition [25]. Fig. 2.5 elucidates the J-V curve with device parameters under simulated illumination.
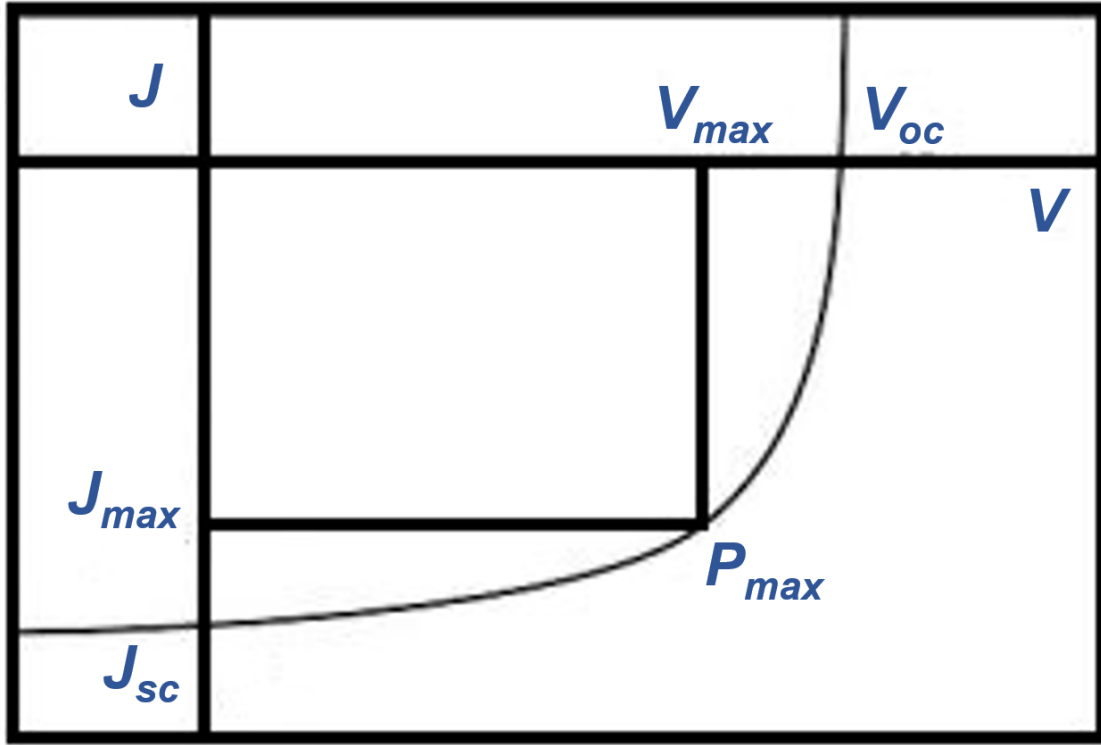
Figure 2.5 **A typical current density-voltage (J-V) characteristics of solar cells under illumination.**

Power conversion efficiency (PCE) of solar cells assesses the device performances and is defined as the ratio of the generated output power and the intensity of the incident light [25, 26]. PCE is calculated by using equation 2.4, where V_{max} is the maximum voltage, J_{max} is the maximum current at maximum output power P_{max}, and P_{in} is the incident light power

17

[27, 28]. The standard illumination intensity is 100 mW/cm^2 as one sun condition with the spectrum of AM 1.5G at constant temperature 25 ^{o}C.

$$PCE = \frac{P_{max}}{P_{in}} = \frac{P_{max} \times P_{max}}{P_{in}} = FF \times \frac{V_{oc} \times J_{sc}}{P_{in}} \qquad 2.4$$

The fill factor (FF) is calculated equation 2.5, J_{sc} is the short circuit current at V = 0 V and V_{oc} is the open circuit voltage at J = 0 mA/cm^2 condition. The fill factor recognizes the ideality of a diode or the squareness of the *J-V* curves [26]. The FF also signifies the characteristics of interfaces and the charge collection efficiency at the respective electrodes [29].

$$FF = \frac{V_{max} \times J_{max}}{V_{oc} \times J_{sc}} \qquad 2.5$$

Two other important parameters that can be derived from the J-V curves are series and shunt resistance. Their values are estimated by finding the inverse slopes at different regions on the J-V curve as shown in Fig. 2.6 [30].
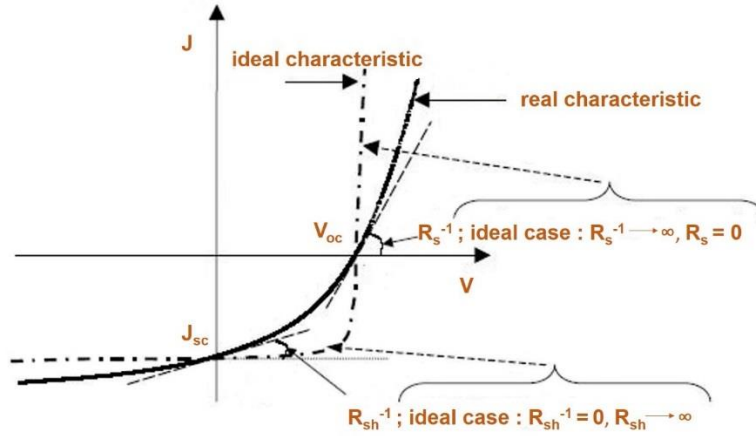
Figure 2.6   Schematic diagram of J-V characteristics representing shunt and series resistances [30]

18

In ideal solar cell devices, the series resistance is close to zero while the shunt resistance approaches a high value as indicated in Fig 2.6. The R_{sh} is due to recombination of charge carriers near D/A interface and at the electrode and is modeled as a leakage current. The charge recombination is a significant parameter and is dependent on ability of the active material to transport separated charge to the electrodes. Series resistance R_s also reflects the ease in which the carrier responds to the electrostatic field (i.e., the mobility) in each specific transport layer and is heavily influenced by the defects and scattering mechanisms. Hence the series resistance depends on the resistivities of the active layer, hole-extraction layer, metal–organic contacts and electrodes [31].

External quantum efficiency (EQE) is determined by the ratio of number of the collected electrons per number of incident photons as expressed in the equation 2.6.

$$EQE = \frac{\text{number of collected electrons}}{\text{number of incident photons}} \qquad 2.6$$

From the photo-generation process, the EQE comprises of various processes including light absorption, exciton generation, exciton dissociation, charge transfer, and charge collection steps. Therefore, EQE can be expressed as product of efficiencies of each process as shown in equation 2.7, where η_A is light absorption efficiency, η_{ED} is exciton dissociation efficiency, η_{CT} is charge transfer efficiency, and η_{CC} is charge collection efficiency.

$$EQE = \eta_A \times \eta_{ED} \times \eta_{CT} \times \eta_{CC} \qquad 2.7$$

Light absorption efficiency is defined as the ratio of number of photons absorbed to the number of incident photons. The absorption efficiency usually increases with the increase in the thickness of light absorbing layer. This efficiency is reliant on the optical band gap of the semiconducting materials. Exciton dissociation efficiency is expressed as the ratio

of number of excitons reaching the interface per number of excitons produced after light absorption. The exciton dissociation efficiency is limited by the exciton diffusion length of organic solar cells. Charge transfer efficiency is described by number of bound excitons transferring to charge carriers to the corresponding electrodes per number of charge carriers.

CHAPTER 3

SELF-ASSEMBLED MONOLAYER MODIFIED ITO IN P$_3$HT: PC$_{61}$BM ORGANIC

SOLAR CELLS WITH IMPROVED EFFICIENCY

3.1   Introduction

Ever since organic solar cells (OSCs) were developed, rigorous efforts have been

made to increase the efficiencies of the OSCs by developing new photoactive, electron and

hole transporting materials and improving properties of electrode materials in polymer,

small molecule and dye-sensitized solar cells [1-8]. OSC devices have acquired a

significant amount of attention due to their favorable properties, such as light weight,

possibility of low temperature fabrication, low cost, and mechanical flexibility in solar

energy conversion [9-11]. A photoactive layer of a blend of regioregular poly(3-

hexylthiophene)(P$_3$HT) and the fullerene derivative [6,6]-phenyl-C61 butyric acid methyl

ester (PC$_{61}$BM) is the most widely researched donor (D) and acceptor (A) materials to date

[12]. The blend of the two materials (P$_3$HT:PC$_{61}$BM) forms a phase-separated bulk-

heterojunction (BHJ) nanostructure that offers a large interfacial area for exciton

dissociation. However, it is still very challenging to fabricate and measure P$_3$HT-based

OSCs in ambient conditions due to the rapid, undesirable interactions of P3HT with

atmospheric oxygen and moisture [13, 14]. In conventional OSC structures the photoactive

layer is inserted between a layer of indium tin oxide (ITO) and a top metal electrode with

low work function (typically aluminum). In these devices, the oxidation of the top metal

electrode (Al) during air exposure leads to a decrease in efficiency of these devices over

time [15]. Moreover, corrosion of ITO by the acidic poly(3,4-

21

ethylenedioxythiophene:polystyrenesulfonate (PEDOT:PSS) layer also leads to the instability in these devices [16].

In case of organic devices, the charge transport through active layers in an organic solar cell is extremely essential to minimize charge recombination which results in low efficiency of the solar cells. Furthermore, charge injection at the organic-inorganic interface is a vital issue for proper device functioning. Thus, interfacial modifications are required for appropriate electrical contacts and to enhance the short-circuit current density (J_{sc}), open-circuit voltage (V_{oc}), and fill factor (FF) of a solar cell. In an ideal case, solar cell devices should have high shunt (parallel) resistance (R_{sh}) and a low series resistance (R_s) in order to elevate the device performance. The electrical properties of P$_3$HT are well known to sensitively depend on detailed process conditions. Recently, Cheng et al have achieved an enhancement in solar cell efficiency by using a simple DMF-involved solution process to form an acceptor rich layer near the cathode and achieve effective vertical phase separation [17]. Another prospective approach to concurrently improve the morphology as well as efficient charge transport in solar cell devices is to adjust the interface between the inorganic anode (ITO) and organic layer (P$_3$HT:PC$_{61}$BM) with a self-assembled monolayer (SAM) [18]. Substrate surface-interface modifications using SAMs have strong influence on the carrier transport in case of P3HT based organic field effect transistors, organic light emitting diodes and organic solar cells [19-21]. They have been used to increase compatibility, adhesion, charge transport properties at the interface and diminish charge recombination [22]. It has been seen that SAMs can also effectively control the immediate upper layer growth mode and distribution of phases and passivate inorganic surface trap states [21]. Our study here presents the use of hexamethyldisilazane (HMDS) on top of

ITO as an interfacial layer. The HMDS modified solar cell also shows improvement in the J_{sc} and FF.

3.2   Experimental details

3.2.1. Reagents and materials

1,1,1,3,3,3-hexamethyldisilazane (HMDS) was purchased from Air Products. PEDOT:PSS (Clevious PVP AI 4083) was purchased from H.C. Stark company. Electron donor material regioregular poly (3-hexylthiophene) (P3HT) was purchased from Reike Metals, Inc. The electron acceptor material [6,6]-phenyl C61 butyric acid methyl ester (PC61BM) and 1,2-dichlorobenzene were purchased Sigma Aldrich. All these commercially available chemicals were used as-received without further purification.

3.2.2. Electrode modification

All devices in this work were prepared on 40Ω sq^{-1} ITO coated glass substrates. The substrates were cleaned in an ultrasonic bath containing acetone, methanol, and isopropanol, followed by ultraviolet ozone (UVO) treatment. A 98 % solution of HMDS was subsequently spin coated on the plasma-treated ITO at 3000 rpm for 60 s and then heated at 75 °C under vacuum for 30 min to allow a conversion of HMDS into a SAM. After that they were sonicated in toluene and finally dried under a stream of nitrogen. The optical transmittance of the bare ITO and the HMDS modified ITO electrodes were measured using Ocean Optics double channel spectrometer (model DS200) in a wavelength range of 300–800 nm. The HMDS modified ITO was characterized by X-ray photoelectron spectroscopy (XPS) using a VG-220IXL spectrometer with monochromatic Al Kα radiation (1486.6 eV, line width = 0.8 eV). The pressure in the analyzing chamber was kept

at a level of 10^{-9} Torr while recording the spectrum. The spectrometer had an energy resolution of 0.4 eV. All the binding energies were corrected with reference to C (1s) at 285.0 eV. Surface morphology of the HMDS modified ITO and bare ITO was acquired by using atomic force microscopy (AFM). All AFM images were filtered and analyzed using Gwyddion (version 2.23) software package.

3.2.3. OSC fabrication

Electron donor material P_3HT and electron acceptor material $PC_{61}BM$ were weighed (1:1 w/w) and dissolved in 1,2-dichlorobenzene (DCB) in a nitrogen-filled glove box. The solution was stirred at room temperature for a minimum of 12h. The active layer materials were then spin coated on the freshly prepared electrodes. Photoactive layers were spin-coated from $P_3HT:PC_{61}BM$ blends at 600 rpm for 1 min, then annealed for 30 min at 120 °C on a hot plate inside the glove box. This corresponded to a layer thickness of 250 nm. Finally, each devices were completed by thermally depositing 0.7 nm LiF followed by 80 nm Al cathodes in vacuum (about 1×10^{-6} Pa). A shadow mask was used during thermal evaporation to define an active area of 0.2 cm^2. The completed were then transferred to the solar simulator for testing.

3.2.4. Device testing

Current density-voltage (J-V) measurements were performed under simulated AM 1.5 global solar irradiation (100 mW/cm^2) using a xenon-lamp solar simulator (Spectra Physics, Oriel Instruments, USA). The light source was calibrated with a standard Si photodiode reference cell (Hamamatsu Photonics, Japan) prior to measurement. The device EQE (%) as a function of wavelength was determined from the photocurrent generated in

the device from an incident monochromatic light source using an Optronic Lab OL750 series spectroradiometer. The EQE was determined by comparing this photocurrent to the monochromatic beam intensity measured using a calibrated Si photodetector.

3.3   Results and Discussion

Historically in semiconductor manufacturing, HMDS has been extensively used for improved the adhesion between photoresist and the silicon wafer. The use of HMDS to form self-assembled monolayer (SAM) requires hydroxylated ITO surfaces, obtained by treating the surface in ozone plasma prior to SAM formation. Figure 3.1 depicts the device architecture of the solar cell structures in this work.
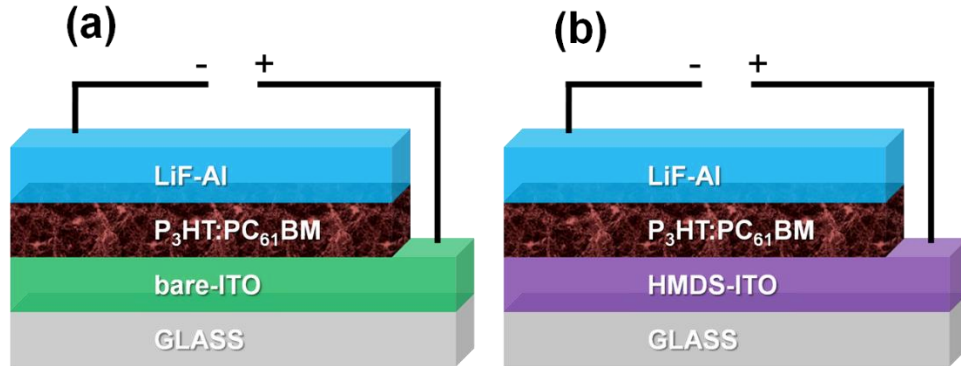
Figure 3.1   Schematic of the solar cell devices (a) bare ITO and (b) HMDS modified ITO.

The modification of the ITO electrode by SAM has mainly two effects on the heterojunction solar cell devices, first, it changes the hole injection barrier due to the work function shift of ITO, and secondly it changes in the morphology of the active layer [21]. The methyl groups in HMDS layer are electron donating in nature, which resulted in slight lowering of the work function of ITO from 4.7 to 4.5 eV and optimum active layer phase separation in $P_3HT:PC_{61}BM$ solar cells [20]. Figure 3.2a shows the schematic of reactive

25

hydroxyl groups on the ITO surface undergoing a hydrolysis reaction with HMDS to form a SAM and losing ammonia. Figure 3.2b shows the wide range XPS spectra for the bare ITO and the HMDS modified ITO sample. The intensity of the In*3d*, In*3p*, Sn*3d* and O*1s* peaks in the HMDS modified ITO reduces, indicating the formation of SAM on top of the ITO layer. However, the intensity of the C *1s* increases in the HMDS modified ITO due to the surface methyl groups. In Fig. 3.2c the appearance of Si*2p* peak related to the Si–O bond near 102 eV on HMDS modified ITO clearly demonstrated the formation of Si-O bond, while the bare ITO did not show any Si*2p* peak in the corresponding energy ranges.
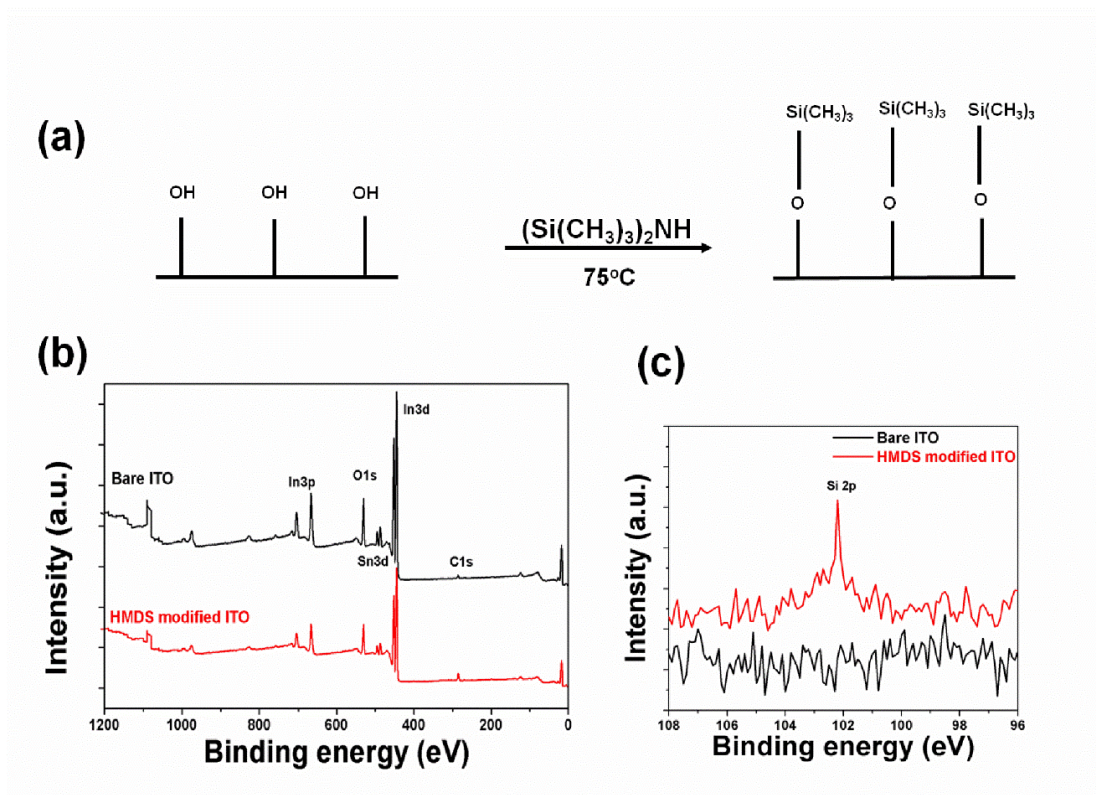
Figure 3.2   (a) Schematic diagram of the SAM formation. XPS spectra of bare ITO and HMDS coated ITO including (b) wide scan and (c) Si 1s profile.

Figures 3.3(a) and 3.3(b) shows the AFM image of bare ITO and HMDS modified ITO electrodes respectively. In our case, the typical root-mean-square (RMS) roughness

26

values over a 1µm×1µm scan for bare ITO films and HMDS modified ITO layers are1.14 nm and 1.48 nm respectively.
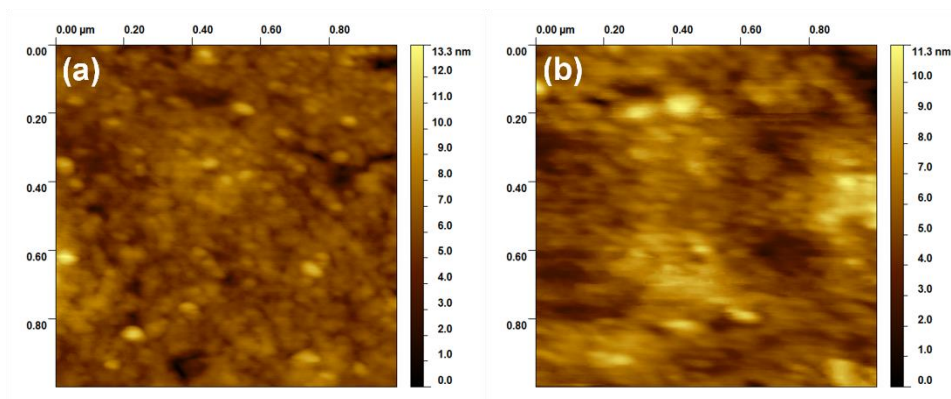
Figure 3.3   AFM surface images of (a) bare ITO and (b) HMDS modified ITO (scan size: 1µm×1µm).

This indicates that a flat monolayer is formed during the self-assembly process. Thus coating the ITO surface with HMDS did not result in any significant change on the morphology of the ITO surface. The main reason behind surface modification of ITO by HMDS monolayer was to increase the crystallinity of the P$_3$HT aggregates [23, 24]. HMDS also modifies the work function of ITO slightly by forming surface dipole moments related to the methyl (-CH$_3$) groups at the ITO surface. Figure 3.4 shows the optical transmittance of both the anodes over the UV-visible (300-800) range. For this range, the average transmittance of bare ITO is 77.6 %, while the HMDS modified ITO shows a slight reduction in the average transmittance value of 77.5 %.
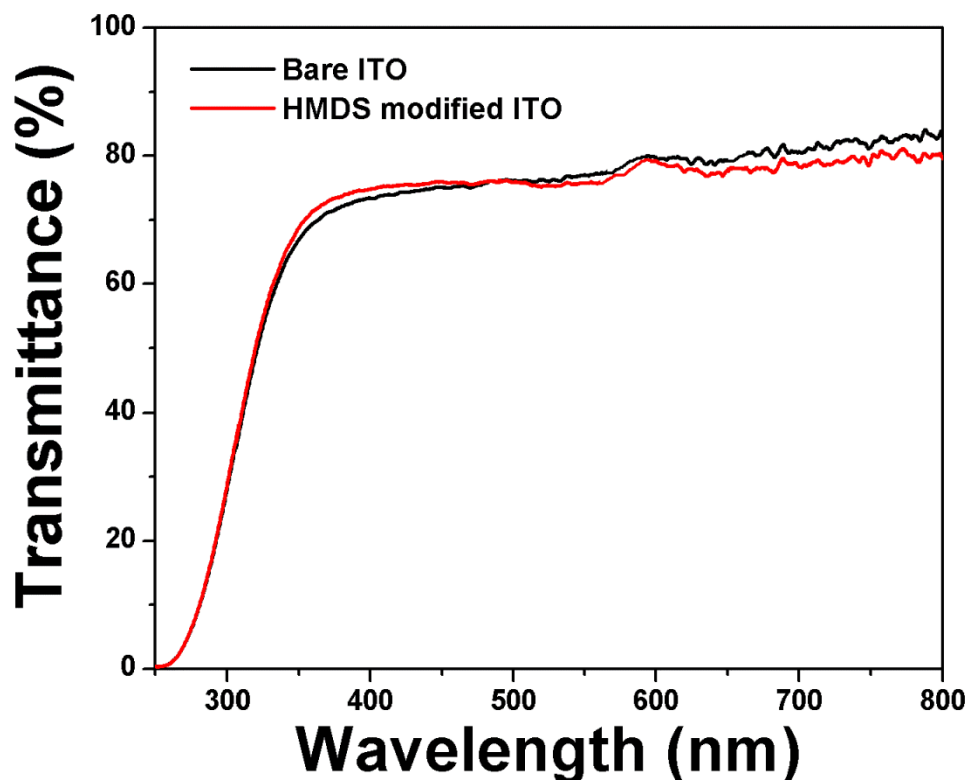
Figure 3.4 **Optical transmission spectra of ITO and HMDS modified ITO. This contributes to some reduction in number of absorbed photons passing through the ITO anode, which in turn may result in slight lowering of the photocurrent generation.**

Figure 3.5(a) shows the current density–voltage (J–V) characteristics of organic bulk heterojunction solar cells bare ITO and SAM modified ITO anodes under AM 1.5 global solar irradiation with intensity of 100 mW/cm^2. The J$_{sc}$, V$_{oc}$, FF, and power conversion efficiency (PCE) values are summarized in Table 3.1. The short circuit current density in the devices with HMDS is higher (10.1 mA/cm^2) when compared to the device consisting of bare ITO electrode with current density value measuring 7.7 mA/cm^2. The

improvement in short-circuit current density is an indication of a good contact between the organic materials and the $-Si(CH_3)_3$ groups. Devices using HMDS modified ITO exhibited slightly greater FF than devices with bare ITO anode as shown in Table 3.1.

TABLE 3.1. Device parameters of organic photovoltaic devices utilizing bare ITO and HMDS modified ITO electrodes.

Device	V_{oc}(V)	J_{sc} (mA/cm^2)	FF(%)	PCE	R_s(Ωcm^2)	R_{sh}(Ωcm^2)
Bare ITO	0.44	7.7	35.9	1.21	11	98
HMDS-ITO	0.46	10.1	37.1	1.70	10	110

This may be due to improved electrode–polymer interface formed due to surface modification. The shunt resistance (R_{sh}) is also a significant parameter which is determined by the film quality and their interfaces. Low values of R_{sh} result from the loss of charge carriers due to leakage through pinholes in the films and recombination and trapping of the carriers during their passage through the cell leading to a fall in device efficiency [18]. It is should be noted that the HMDS modified ITO device had higher R_{sh} value when compared to the bare ITO device. As expected, V_{oc} value remains almost the same since the active layer fabrication condition and the cathode layer deposition remain constant. Figure 3.5(b) shows that the devices with HMDS modified ITO electrode shows brilliant diode quality with very low leakage current and high rectification ratio.
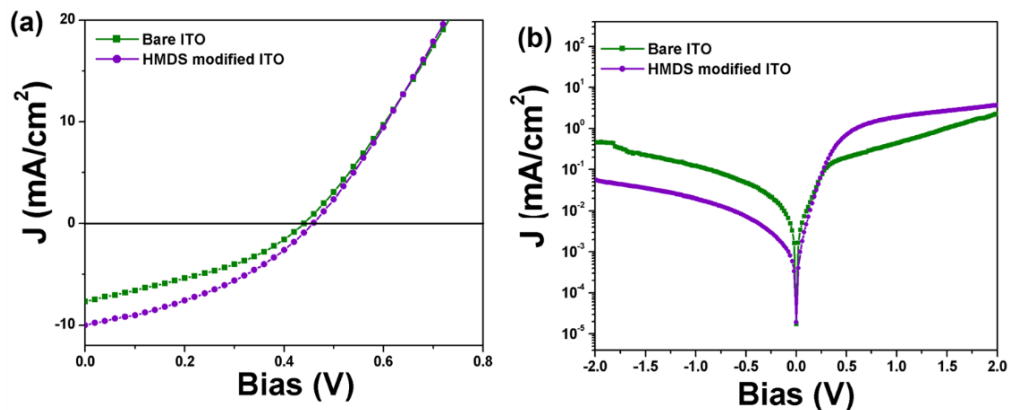
Figure 3.5   *J-V* **characteristics of the OSC devices with bare ITO and HMDS**

modified ITO substrates (a) under illumination and (b) in the dark.
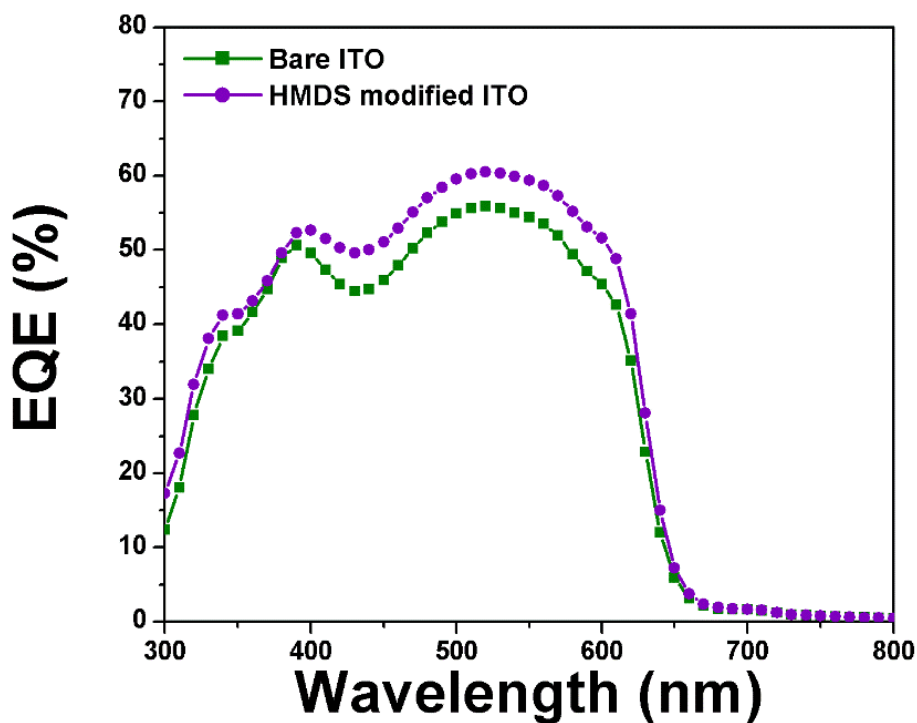
Figure 3.6   **External quantum efficiency (EQE) measurement of the**

P₃HT:PC₆₁BM devices using bare ITO and HMDS modified ITO anodes.

Figure 3.6 shows the external quantum efficiency (EQE) results of devices with

different electrodes used in our study. Both devices show efficient photoconversion

efficiency in the range between 400 and 600nm with EQE values over 50%. The data for EQE supports the improved device performance of the HMDS modified electrode.

3.4   Conclusion

Herein our preliminary work demonstrates that a HMDS modified ITO is a viable alternative as an electrode in solar cell devices with modified work function and properties. In this case, some performance enhancement was observed in OPV devices using the HMDS modified electrode when compared to bare ITO thin film. The surface morphology of the bare ITO and HMDS modified ITO are also comparable. These results encourage the use of a more efficient photoactive system to obtain higher PCEs to fabricate the organic solar cells using HMDS modified ITO electrodes.

CHAPTER 4

P3HT:PC61BM BASED SOLAR CELLS EMPLOYING SOLUTION PROCESSED

COPPER IODIDE AS THE HOLE TRANSPORT LAYER

4.1.   Introduction

The relentless increase in energy demand in today's world has led to the search for newer renewable energy sources and photovoltaics appeared to be one of the best alternatives for energy production. Ever since organic solar cells (OSCs) gained a reputation of the successful conversion of solar energy to useful electrical energy,numerous efforts have been made to increase thepower conversion efficiencies (PCE) by development of new photoactive materials, electron and hole transporting medium; as well as, designing new transparent electrode system to replace the expensive indium tin oxide [1-12]. Moreover, organic solar cells present many advantages; including the use of low-cost, light-weight materials, compatibility with flexible substrates, low-temperature and roll-to-roll manufacturing techniques [13-15]. The most widely researched photoactive layer to date is a blend of regioregular poly(3-hexylthiophene)(P$_3$HT) and the fullerene derivative [6,6]-phenyl-C61 butyric acid methyl ester (PC$_{61}$BM) [16]. Under illumination, the blend of the two materials (P$_3$HT:PC$_{61}$BM) generates excitons which are then efficiently segregated to charge carriers at the interface of the bulk-heterojunction (BHJ) nanostructure and carried towards respective electrodes.

In case of organic solar cell devices, the efficient charge transport through active layers towards the respective electrodes is extremely essential to minimize charge recombination which results in low efficiency in typical applications. However, the search for a suitable interfacial layers between electrodes and activelayer still remains. Hole

transport layers (HTLs) like poly3,4-ethylenedioxythiophene: polystyrene sulfonate (PEDOT:PSS) are widely used in BHJ cells to ensure Ohmic contacts, efficient hole collections and ITO planarization [17, 18]. At the same time, the acidic nature of PEDOT:PSS makes the indium tin oxide (ITO) surface vulnerable to degradation at elevated temperatures [19, 20]. Several metal oxides have been demonstrated as efficient hole transport layers in organic solar cell devices. However, the deposition of these oxides generally involves evaporation of the materials in high vacuum tools, which are considerably more expensive and complicated than solution-based processes [14, 21-23].

Cuprous iodide (CuI) is a wide band gap (3.1 eV) and has three crystalline phases [24, 25]. Amongst the different phases, CuI in the γ-phase with zinc-blende structure and has p-type character. Zhou *et al.* first reported the use of CuI layer in $ZnPc:C_{60}$ based bilayer organic solar cells; where, the CuI nanocrystals are evaporated onto an ITO surface at a glancing angle and is followed by deposition of ZnPc [26]. The investigators suggest that the strong interaction of ZnPc and CuI enables the formation of ZnPc nanopillar arrays. The pillar structure helps to improve light absorption and increases surface roughness induced exciton dissociation. Shao *et al.* showed that thermally evaporated CuI not only provides Ohmic contact with the active layer ($P3HT:PC_{61}BM$), but also results in vertical orientation of $\pi-\pi$ stacking planes of P_3HT with respect to the substrate [27]. They show that the hole mobility of $P3HT:PC_{61}BM$ blend film deposited on CuI surface is higher when compared to the films deposited on PEDOT:PSS because the vertical $\pi-\pi$ stacking planes of P3HT induces efficient CuI hole collection in polymer photovoltaic cells. In this work we show a solution processed CuI film as an effective HTL in $P3HT:PC_{61}BM$ solar cell. It is found that the concentration of CuI played an important role in determining the device

33

efficiency. This work implies that the inexpensive and solution processed CuI can effectively curtail the manufacturing time of low-cost organic solar cell devices in roll-to-roll fabrication.

4.2. Experimental details

4.2.1. Reagents and materials

The PEDOT:PSS and the electron donor material regioregular poly (3-hexylthiophene) (P3HT) materials were purchased from domestic chemical vendors. The electron acceptor material [6,6]-phenyl C61 butyric acid methyl ester (PC$_{61}$BM), copper iodide (CuI) and 1,2-dichlorobenzene were obtained Sigma Aldrich. All these commercially available chemicals were used as-received without further purification.

4.2.2. Device fabrication

All devices in this work were prepared on 40Ω sq^{-1} ITO coated glass substrates. The substrates were cleaned in sequential ultrasonic baths of acetone, methanol, and isopropanol, followed by ultraviolet ozone (UVO) treatment for 10 min. Electron donor material P$_3$HT and electron acceptor material PC$_{61}$BM were weighed (1:0.8 w/w) and dissolved in 1,2-dichlorobenzene (DCB) in a nitrogen-filled glove box. The solution was stirred for 12h at room temperature. The PEDOT:PSS solution was spin-coated at 5000 rpm for 60 s on the cleaned ITO substrates, followed by baking at 150 °C for 15 min on a hot plate resulting to a thickness of 30nm. Different amounts of CuI were weighed out and dissolved in acetonitrile solvent. This solution was used as the precursor solution for spin coating the CuI layer. The different concentrations of CuI solutions were then spin coated on cleaned ITO substrates at 4000 rpm for 60s, followed by baking on a hot plate at 80 °C

inside the glove box. The active layer materials were spin-coated onto the freshly prepared electrodes. Photoactive layers were spin-coated from $P_3HT:PC_{61}BM$ blends at 600 rpm for 1 min, then annealed for 30 min at 120 ^oC on a hot plate inside the glove box. This corresponded to a layer thickness of 250 nm. Finally, all device fabrication were completed by thermally depositing 15 nm BCP followed by 80 nm Al cathode deposition vacuum (~ 10^{-6}Torr). The thin BCP film acted as an exciton or hole-blocking layer (EBL or HBL).A shadow mask was used during thermal evaporation to define an active area of 0.2 cm^2. The completed device was then transferred to the solar simulator for testing.

4.2.3.   Thin film characterization and device testing

The optical transmittance of PEDOT:PSS and CuI thin films were measured using Ocean Optics double channel spectrometer (model DS200) in a wavelength range of 300–800 nm. The structural properties of the as-deposited and annealed CuI films were investigated by x-ray diffraction (XRD) on P*analytical X'PertPro* X-ray diffractometer (XRD)with monochromated Cu Kα irradiation (λ = 1.5418 Å). Surface morphology of the CuI layers on ITO obtained from different concentration of precursor solution was acquired by using atomic force microscopy (AFM). Work function of CuI layers were measured with Kelvin probe system (model KP-6500) under inert nitrogen gas atmosphere. A highly oriented pyrolytic graphite (HOPG) was used for reference work function which is known to be 4.6 eV. Current density-voltage (J-V) measurements were performed under simulated AM 1.5 global solar irradiation (100 mW/cm^2) using a xenon-lamp solar simulator (Spectra Physics, Oriel Instruments, USA). The light source was calibrated with a standard Si photodiode reference cell (Hamamatsu Photonics, Japan) prior to measurement.The device external quantum efficiency (EQE) as a function of wavelength was determined from the

photocurrent generated in the device from an incident monochromatic light source using an Optronic Lab OL750 series spectroradiometer.

4.3. Results and discussion

Figure 4.1 illustrates the transmission spectra of PEDOT:PSS film and thin films of CuI on glass substrates. It reveals that all of these films were highly transparent in the visible region between 400 and 800 nm. Moreover, all the CuI films exhibit higher transparency than the PEDOT:PSS films in the region between 500-800 nm. Interestingly, a hump is observed at about 407 nm and this is due to the excitation of electrons from the subband in the valence bands to the conduction bands of CuI [28].The size of this hump increases with increasing the amount of CuI in the films. With the increase in the concentration of the CuI precursor solution the transmittance decreases due to increase in thickness of the CuI layer.
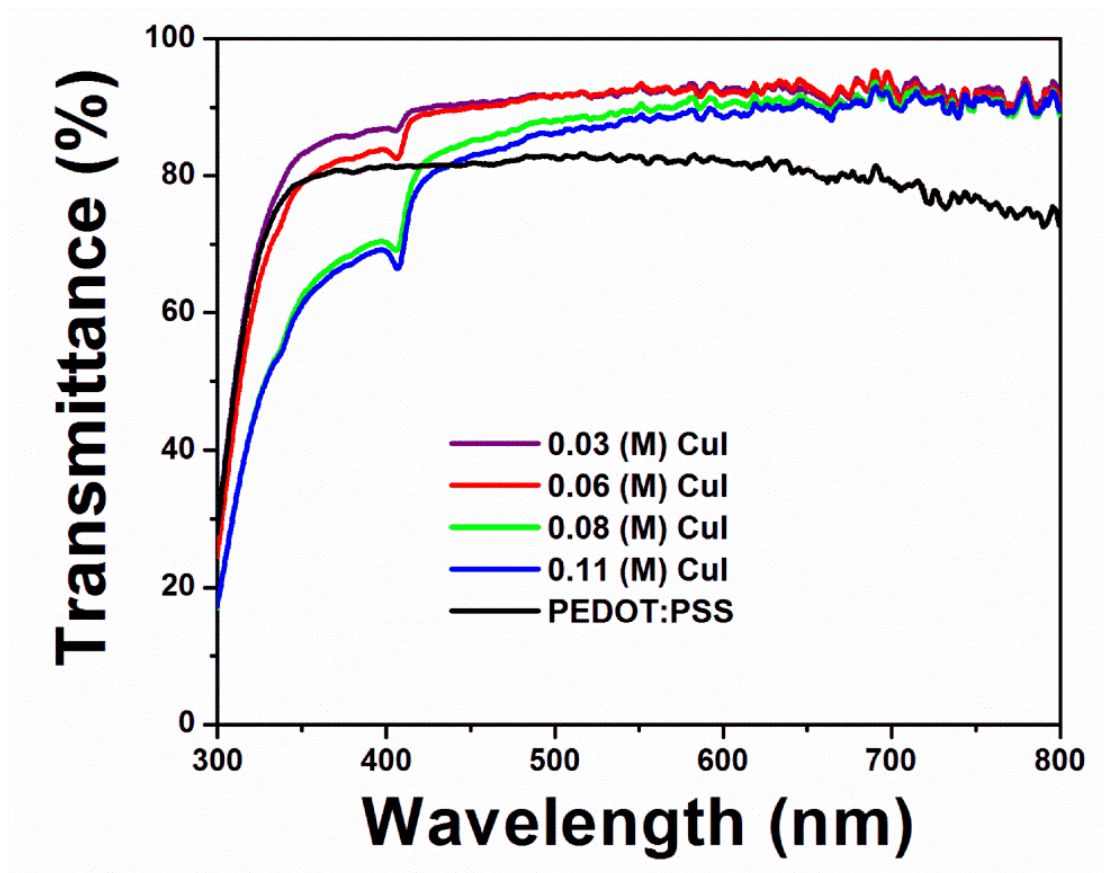
Figure 4.1 **Optical transmission spectra of PEDOT:PSS and thin films of CuI on glass substrates.**

Figure 4.2 shows XRD patterns regarding the structure of as-deposited and annealed CuI thin films on glass substrate. The spin coating and annealing of CuI films are done inside a glove in order prevent the oxidation of CuI to copper oxide. The JCPDS card 83-1137 is used to identify the cubic γ-phase of CuI [25]. The CuI peak at 25.5° (2θ) corresponds to the (111) reflection of the cubic structure of copper iodide. The as deposited CuI films show broad (111) peak which indicates that the film consists of nanometer sized grains. After annealing for 10 min at 80 °C, the full width at half-maximum (FWHM) of the CuI (111) peak decreases slightly which indicates grain growth. Moreover, a

37

considerable increase in the intensity of the CuI (111) peak is observed and another weak peak at 52.3° (2θ) corresponding to the (222) is found which also indicates that the crystallinity of the CuI film is improved after the annealing process at 80 °C.
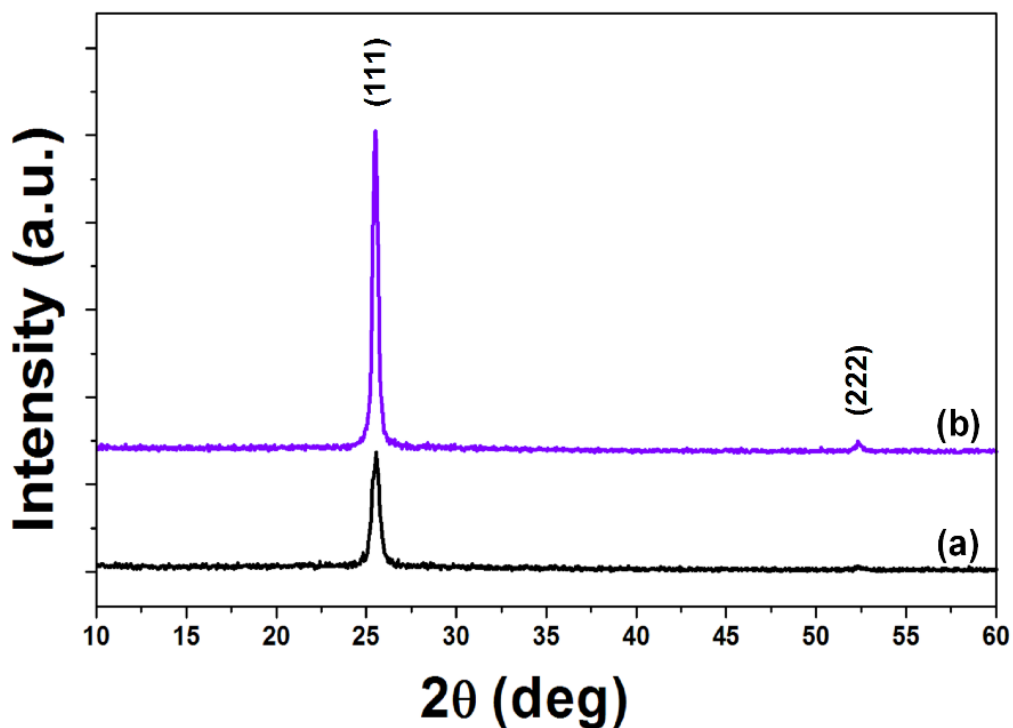
Figure 4.2   XRD patterns of (a) as-deposited and (b) annealed CuI thin films on glass substrate.

The device structure of the OSCs and the schematic energy diagram of the materials in devices are illustrated in Fig. 4.3. The energy level diagram in Fig. 4.4 suggests that CuI represents a suitable hole transport layer in P$_3$HT:PC$_{61}$BM type BHJ solar cells. The morphology of the interfacial layers plays an important role in both charge collection and transport in organic photovoltaic devices.
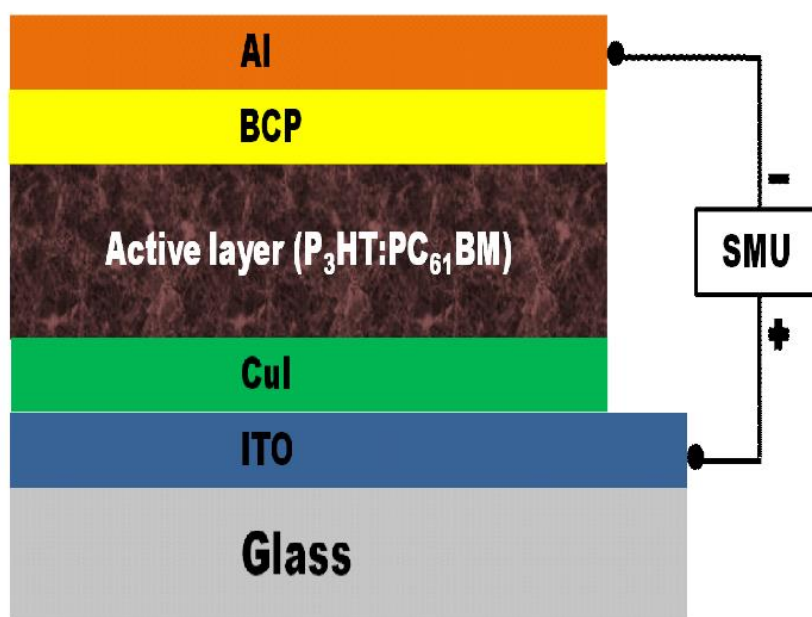
Figure 4.3   **Schematic of the OSC devices with CuI hole transport layer**
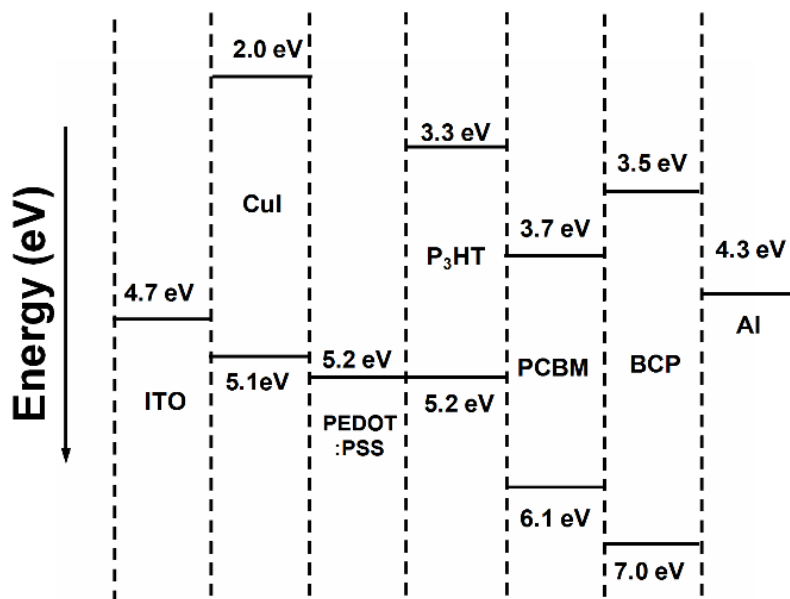
Figure 4.4   **Energy level diagram of different components of the OSC devices.**

Figure 4.5 shows 2×2 μm^2 tapping mode AFM images of the different CuI layers on ITO. Greater surface roughness of a layer will impede formation of an intimate contact with the active layer which results in a reduced charge transport efficiency at the interface, as a consequence, decrease the device performance. The surface root-mean-square roughness of the CuI layer on ITO formed using a 0.03(M) solution is ~1.25 nm. On increasing the concentration of the precursor solution to 0.06(M), the surface roughness further increases to ~5.53 nm and indicates the formation of thicker CuI layer that unevenly coats the ITO layer. The 0.08(M) and 0.11(M) solutions generate surface roughness of ~3.50nm and ~3.62nm implying a uniformly covered ITO surface.
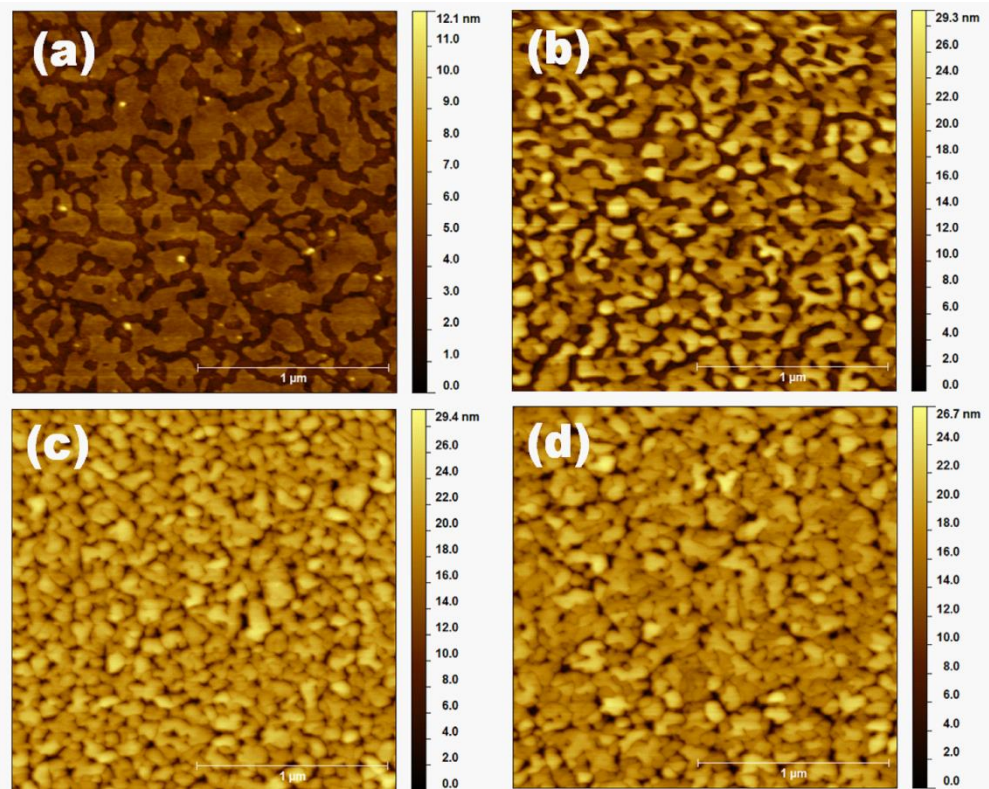
Figure 4.5 2×2 μm^2 tapping mode AFM images of (a) ITO/CuI (0.03 (M)), (b) ITO/CuI (0.06 (M)) (c) ITO/CuI (0.08 (M)) and (d) ITO/CuI (0.11 (M)).

Figure 4.6 shows the current density–voltage (J–V) characteristics of organic bulk heterojunction solar cells in dark and under AM 1.5 global solar irradiation with intensity of 100 mW/cm^2. The dark J−V curves show a typical diode behavior in the devices. It was found that the dark current density in CuI devices was higher when compared to the PEDOT:PSS based devices with the additional increase in voltage in the forward bias region.
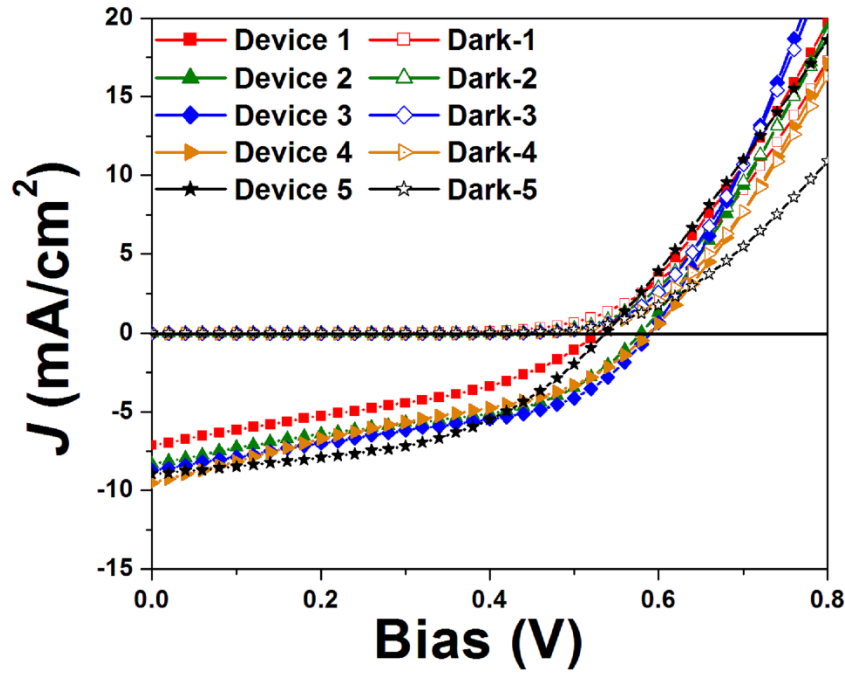
Figure 4.6   *J-V* **characteristics of the OSC devices.**

The short-circuit current (J_{sc}), open-circuit voltage (V_{oc}), fill factor (*FF*), and power conversion efficiency (PCE) of the OSCs with different concentrations of CuI values are summarized in Table 4.1. It should be noticed here that the PCE first increases to a maximum and then decreases signifying two contending and opposite mechanisms in play. Further investigations reveal that the short circuit current density and open circuit voltage do not change significantly; however, there are some differences in the FF.

TABLE 4.1   Device parameters of organic solar cells under illumination with different amount of CuI hole transport layer spin coated onto ITO electrodes.

Device	HTL	V_{oc}(V)	J_{sc} (mA/cm^2)	FF(%)	PCE(%)	R_s ($\Omega.cm^2$)	R_{sh} ($k\Omega.cm^2$)
1	0.03(M) CuI	0.53	7.11	37	1.39	8.8	0.09
2	0.06(M) CuI	0.58	8.33	43	2.08	8.5	0.09
3	0.08(M) CuI	0.59	8.71	44	2.25	5.6	0.13
4	0.11(M) CuI	0.59	9.53	34	1.91	8.2	0.08
5	PEDOT:PSS	0.54	8.98	48	2.33	13.9	0.33

The FF is mostly influenced by series resistance (R_s) and shunt resistance (R_{sh}) of the solar cell device. The series and shunt resistances are often used to understand the nature of the films and their interfacial properties. To achieve a high FF, the series resistance should decrease, while the shunt resistance should approach a high value. A decrease in R_{sh} is observed due to recombination of charge carriers near donor-acceptor (D/A) interface and at the electrodes. The series resistance arises due to the resistivities of the electrodes, metal–organic contacts, active layer, and the hole extraction layers. According to Table 4.1, the devices with CuI as the hole transport layer exhibited lower R_s when compared with the device based on PEDOT:PSS layer. However, the R_{sh} of the CuI based devices decreases drastically indicating high current leakage compromising the PCE. With the increase in concentration of CuI precursor solution from 0.03(M) to 0.08(M), the

R_s is found to decrease from 8.8 to 5.6 $\Omega.cm^2$; however, further increase in the concentration to 0.11(M) again results in an increase in R_s to 8.2 $\Omega.cm^2$ indicating that 0.08(M) is the optimum concentration of CuI to be used. The highest shunt resistance for the CuI based device is shown by device 3, the value of which is half that of the PEDOT:PSS based control device.

The increase in short-circuit current density with increase in the concentration of CuI solution is an indication of a good contact between the organic materials and the underlying CuI layers. The highly hydrophobic surface of CuI layers as determined by Shao and coworkers also suggests its compatibility with the organic P3HT:PC$_{61}$BM active layer [27]. It can be seen that, the control device (Device 5) with PEDOT:PSS as anode buffer layer demonstrates a J_{sc} of 8.98 mA/cm^2, V_{oc} of 0.54 V, and a fill factor (FF) of 48%, resulting in a PCE of 2.33%. The different devices with CuI as anode buffer layer were spin coated from different concentrations of CuI solutions. Among the different CuI anode layer based devices, Device 3 (spin coated from 0.08(M) CuI solution) showed the best PCE of 2.25 % with a J_{sc} of 8.71 mA/cm^2, a V_{oc} of 0.59 V and a FF of 44%. Device 4 (spin coated from 0.11(M) CuI solution) showed the highest J_{sc} of 9.53 mA/cm^2 and a V_{oc} of 0.59 V; however, the FF reduces considerably to 34% resulting in a significant decrease in PCE to 1.91%.

Results of Kelvin probe measurements performed on the modified ITO surfaces coated with different concentrations of CuI solutions and compared to bare ITO are shown in Table 4.2 and provide a measure of work function. It is observed that the effective work function of modified ITO surfaces are higher than bare ITO surface indicating efficient hole injection in the CuI based organic solar cell devices. The highest efficiency is observed

43

for the layer coated with 0.08(M) CuI solution. However further increasing the concentration to 0.11(M) results in a slight lowering of the effective work function.

TABLE 4.2   Work function values of bare ITO and ITO covered with CuI layer prepared by spin-coating different concentrations of CuI precursor solution and measured using a kelvin probe microscope

CuI concentration (M)	Work Function (eV)
0	4.71
0.03(M)	4.75
0.06(M)	4.87
0.08(M)	4.95
0.11(M)	4.82

Cheng *et al.* reports that for very thin films of CuI on ITO an electron transfer process occurs from ITO to the CuI layer inducing a dipole layer at ITO/CuI interface [29]. The resulting dipole layer raises the work function of the ITO surface, which diminishes the hole collection barrier in the OSCs [29]. The EQE result of the device 3 (CuI based device) and 5 (PEDOT:PSS based device) shown in Fig. 4.7 demonstrates an efficient photoconversion efficiency with values over 55% in the range of wavelengths between 400 and 600 nm.
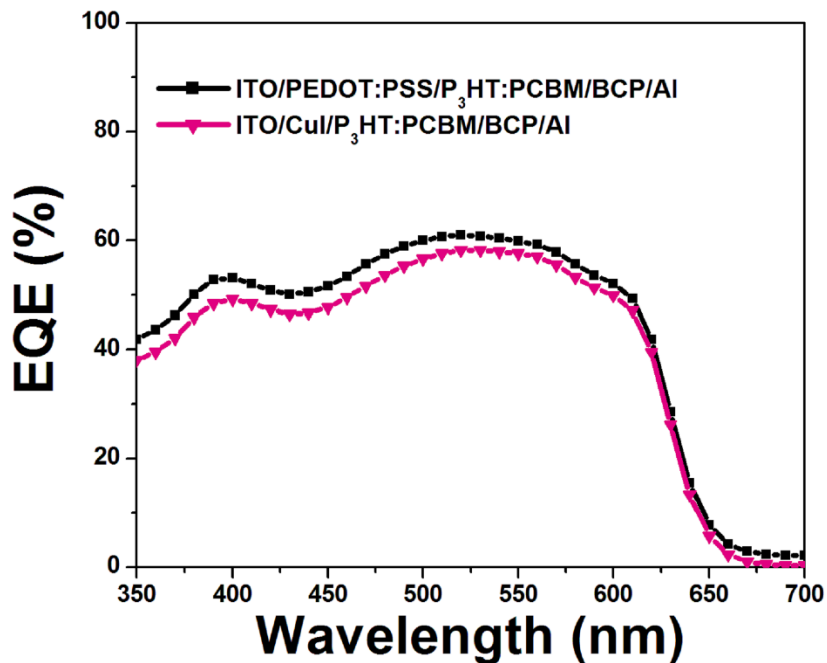
Figure 4.7   External quantum efficiency (EQE) measurement of the

P3HT:PC61BM devices 3 and 5.

4.4.   Conclusion

In conclusion, our preliminary work demonstrates that a solution processed CuI hole transport layer is a viable alternative to the acidic and more expensive PEDOT:PSS. This work implies that CuI is a promising hole transport layer material and can probably reduce the fabrication time of polymer solar cells in low-cost roll-to-roll manufacturing. The amount of CuI in the solution has been optimized here.

CHAPTER 5

IMPROVED EFFICIENCY OF P$_3$HT: PC$_{61}$BM SOLAR CELLS BY

INCORPORATION OF SILVER OXIDE INTERFACIAL LAYER

5.1. Introduction

The use of organic solar cells (OSCs) as a renewable electrical energy source offers a great technological advantage because of its cost-effective and low temperature fabrication process [1-4]. Over the past two decades OSC devices have witnessed a steady evolution as evidenced by the development of new designs, newer materials and interfacial layers which now exhibit very high power conversion efficiencies (PCEs) [5-10]. Bulk-heterojunction (BHJ) structures in OSCs are one of the most promising alternatives to the more expensive silicon solar cells. For optimal functioning of OSCs, efficient charge carrier extraction from the active layer to the respective electrodes is essential [8]. This is highly controlled by the character of the interfaces of each layer. One approach of efficient charge extraction is to match the highest occupied molecular orbital (HOMO) and the lowest unoccupied (LUMO) energies of the active layer with the work functions of the anode and cathode, respectively [11, 12]. Previous investigations show that the performance improvement of an organic solar cell through the introduction of self-assembled monolayers of molecules on ITO substrates with dipole moment of appropriate direction and magnitude [13, 14]. This method effectively changes the work function of ITO and decreases the injection barrier between ITO and the HOMO level of the active layer in organic solar cells. Another approach shows that the formation of an interfacial energy step could improve the charge collection efficiency in organic photovoltaic devices and thereby increase their efficiency [15, 16].

In OSCs, a blend of regioregular poly(3-hexylthiophene) (P3HT) and the fullerene derivative [6,6]-phenyl-C61 butyric acid methyl ester (PC$_{61}$BM) is the most widely researched donor and acceptor materials [17]. The blend of these two materials (P3HT:PC$_{61}$BM) forms a phase-separated (BHJ) nanostructure that offers a large interfacial area for efficient exciton dissociation [18]. A thin poly(3,4-ethylenedioxythiophene):poly(styrenesulfonate) (PEDOT:PSS) layer on top of the anode is commonly used as an anode contact. This is because the work function of PEDOT:PSS matches well with the HOMO of P3HT and thus can effectively extract holes from the active layer. Besides, the thin film of PEDOT:PSS planarizes the ITO surface without significantly affecting the light absorption by the active layer [19]. Other benefits of using PEDOT:PSS include its high electrical conductivity and low temperature solution processability which makes it an ideal hole transport material in flexible organic solar cell devices. Even though PEDOT:PSS has been used widely as hole transport layer, its electrical inhomogeneity [20] prevents it to be an efficient electron blocking layer [21]. Moreover, the acidic and hygroscopic nature of PEDOT:PSS can result in degraded device performance [22, 23]. Metal oxides like MoOx, VOx, NiOx and WOx have been used as a substitute to PEDOT:PSS; however, these metal oxides form rough interfaces which can result in degraded device performances [24-26].

In this work, OSC devices with a AgOx interfacial layer added in between the ITO and PEDOT:PSS and their properties are investigated. The AgOx and PEDOT:PSS layers form a composite hole transport layer. Increased fill factor (FF) and power conversion efficiency (PCE) of the solar cell devices are obtained with the implementation of the AgOx interfacial layer. The interfacial modification also results in improved shunt

47

resistances suggesting lesser charge recombination due to cascading hole transport process. Moreover, this technique reduces the physical contact of PEDOT:PSS with ITO layer by the introduction of the AgOx thin film.

5.2.   Experimental details

5.2.1. *Reagents and materials*

PEDOT:PSS (Clevious PVP AI 4083) was purchased from H.C. Stark Company. The electron donor material regioregular poly (3-hexylthiophene) (P$_3$HT) was purchased from Reike Metals, Inc. The electron acceptor material [6,6]-phenyl C61 butyric acid methyl ester (PC$_{61}$BM) and 1,2-dichlorobenzene were purchased from Sigma Aldrich. All these commercially available chemicals were used as-received without further purification.

5.2.2. *Electrode modification*

All devices in this work were prepared on patterned ITO (40Ω sq^{-1}) coated glass substrates. The substrates were cleaned in sequential ultrasonic baths of acetone, methanol, and isopropanol, followed by ultraviolet ozone (UVO) treatment for 15 min. Silver oxide (AgOx) layer was then deposited on top of ITO by first depositing 1 nm thick Ag metal by thermal evaporation at a pressure of ~10^{-7} Torr followed by UVO treatment for 1 min. This led to the formation of silver oxide as confirmed by X-ray photoelectron spectroscopy (XPS) analysis. The optical transmittance of bare ITO and AgOx modified ITO electrodes were measured using Ocean Optics double channel spectrometer (model DS200) in a wavelength range of 300–800 nm. The oxidation state of Ag in the modified ITO electrode was determined by XPS using a VG-220IXL spectrometer with monochromatic Al *Kα* radiation (1486.6 eV, line width = 0.8 eV). The pressure in the analyzing chamber was kept

48

at a level of 10^{-9} Torr while recording the spectrum. The spectrometer had an energy resolution of 0.4 eV. All the binding energies were corrected with reference to C (1s) at 284.6eV.

5.2.3. *OSC fabrication*

Electron donor material P3HT and electron acceptor material $PC_{61}BM$ were weighed (1:1 w/w) and dissolved in 1,2-dichlorobenzene (DCB) in a nitrogen-filled glove box.
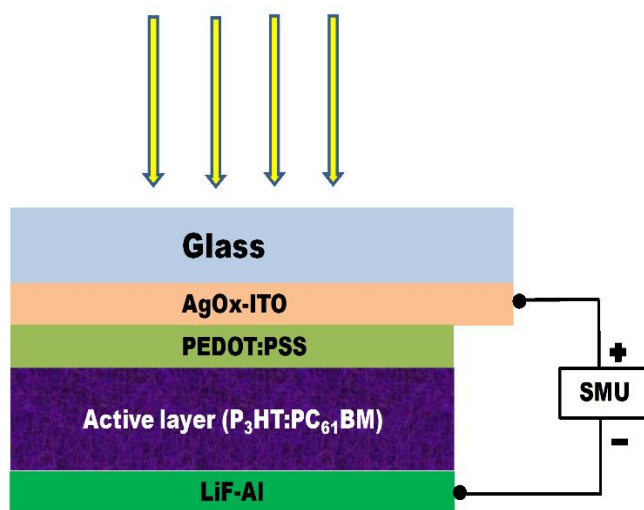
Figure 5.1   Schematic configuration of the organic solar cells device.

The solution was stirred at room temperature for a minimum of 12 hours. The PEDOT:PSS solution was spin-coated at 5000 rpm for 60 s onto freshly prepared electrodes, followed by baking on a hot plate at 150 ^{O}C from 15 min. Photoactive layers were then spin-coated from P3HT:$PC_{61}BM$ blends at 600 rpm for 1 min, then annealed for 30 min at 120 ^{O}C on a hot plate inside the glove box. This corresponded to layer thickness of 250 nm. Finally,

each devices were completed by thermal deposition of 0.7 nm of LiF followed by 80 nm thick Al cathodes in vacuum (about 1×10^{-6}Torr). A shadow mask was used during thermal evaporation to define an active area of 0.2 cm^2. Both type of devices (control and AgOx modified) were then transferred to the solar simulator for testing. The schematic of the device with AgOx interfacial layer is shown in Fig. 5.1.

5.2.4. Device testing

Current density-voltage (J-V) measurements were performed under simulated AM 1.5 global solar irradiation (100 mW/cm^2) using a xenon-lamp solar simulator (Spectra Physics, Oriel Instruments, USA). The light source was calibrated with a standard Si photodiode reference cell (Hamamatsu Photonics, Japan) prior to measurement. The external quantum efficiency (EQE) of the devices was determined as a function of wavelength from the photocurrent generated in the device from an incident monochromatic light source using an Optronic Lab OL750 series spectroradiometer. The EQE was determined by comparing this photocurrent to the monochromatic beam intensity measured using a calibrated Si photodetector.

5.3.   Results and Discussion

For samples consisting of UVO-treated 1 nm Ag on ITO, XPS analysis is utilized to analyze the different oxidation states of the AgOx thin film. Figure 5.2 shows a wide range spectrum and high-resolution Ag3d$_{5/2}$ and O 1s spectra for AgOx thin films on ITO. The Ag 3d$_{5/2}$ signal can be deconvoluted into two peaks, and the corresponding binding energies observed for the AgOx films are 367.8 eV and 368.2eV, which are consistent with those of AgO and Ag$_2$O, respectively [27]. The estimated percentages of the two

deconvoluted peaks (Ag^{2+} to Ag^+ ratio 72:28) indicates that Ag^{2+} is the dominant silver oxidation state in the AgOx thin films after ozonization. Deconvolution of the O 1s spectrum gives information regarding the chemical state of oxygen in the AgOx films on ITO. The silver oxide (AgOx) is a p-type semiconductor with its work function ranging between 4.7-5.2 eV depending on the processing conditions [28].
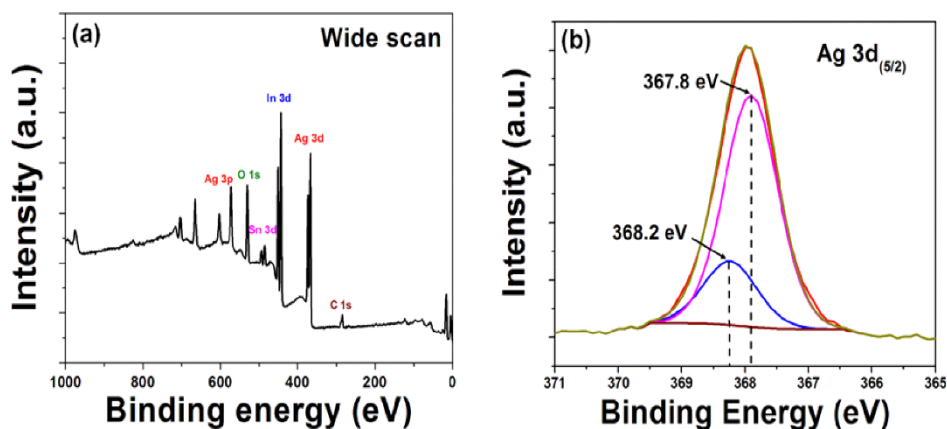
Figure 5.2   (a) Full scan XPS showing Ag 3d, In 3d and Sn 3d peaks for AgOx film on the top of ITO substrate (b) the deconvoluted peaks of Ag 3d$_{5/2}$ with binding energies at 367.8 eV and 368.2eV for Ag $^{+2}$ and Ag $^{+1}$, respectively.

The energy band diagram showing the cascade type hole transport due to this hybridization is represented in Fig. 5.3. Interfacial morphology plays a crucial role in both charge collection and transport in organic photovoltaic devices. Greater surface roughness over the electrode surface can cause formation of defects which can decrease the device efficiency [29].
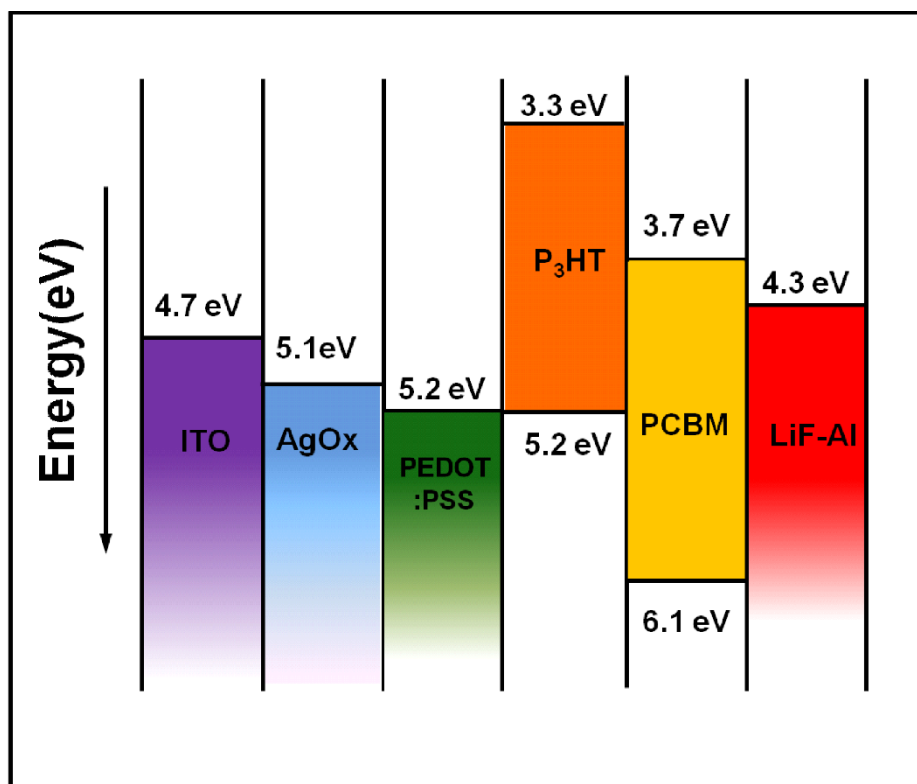
Figure 5.3   Energy level diagram for a P₃HT:PC₆₁BM bulk-heterojunction solar cell with AgOx interfacial layer. The published values of valence band, conduction band, and the Fermi level energies of the different materials are shown here.

Figure 5.4 shows the 4×4 µm^2 tapping mode AFM images of bare ITO and AgOx modified ITO. The root-mean-square (rms) roughness of a bare ITO substrate was 0.5 nm; while, the rms roughness of ITO substrates with AgOx on top increased to a value of 4.2 nm. Thus, adding the AgOx layer increased the surface morphology significantly. It should be noted here that ITO layer is not fully covered by AgOx completely due to the formation of Ag islands during evaporation.
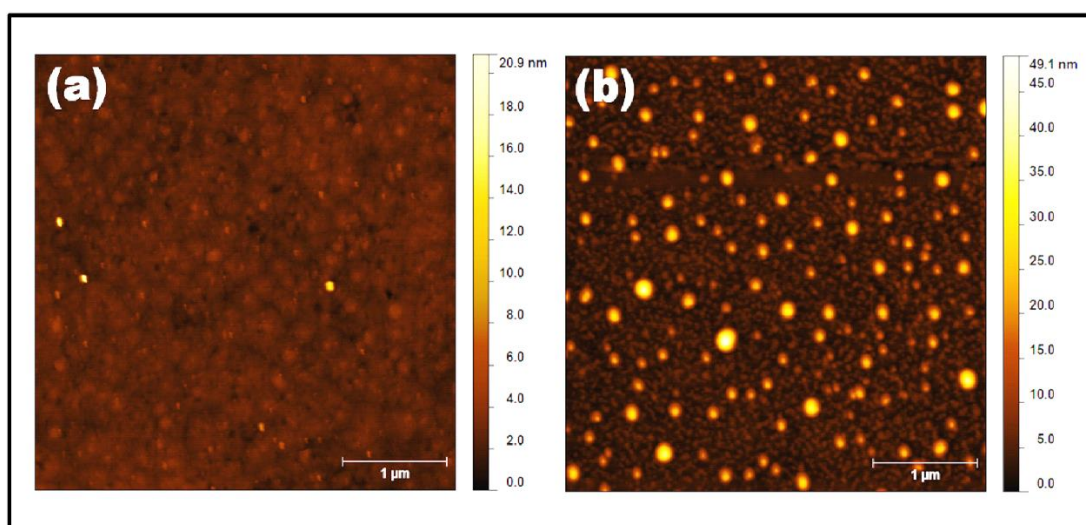
Figure 5.4   AFM surface images of (a) bare ITO and (b) AgOx modified ITO (scan size: 4µm×4µm).

Previous investigations by our group and other groups suggest that the absorption band of P3HT:PC$_{61}$BM blend (1:1 weight ratio) is 400-600 nm and the maximum absorption wavelength for annealed films are ~510 nm [30, 31]. Figure 5.5 shows the optical transmittance of bare ITO and AgOx/ITO layer over the range 400−800 nm. For this range, the average transmittance of the ITO coated glass substrate is about 77%. Upon insertion of the thin AgOx layer the average transmittance slightly reduces to 74% which

results in the reduction in number of absorbed photons passing through the anode and correspondingly decrease photocurrent generation.
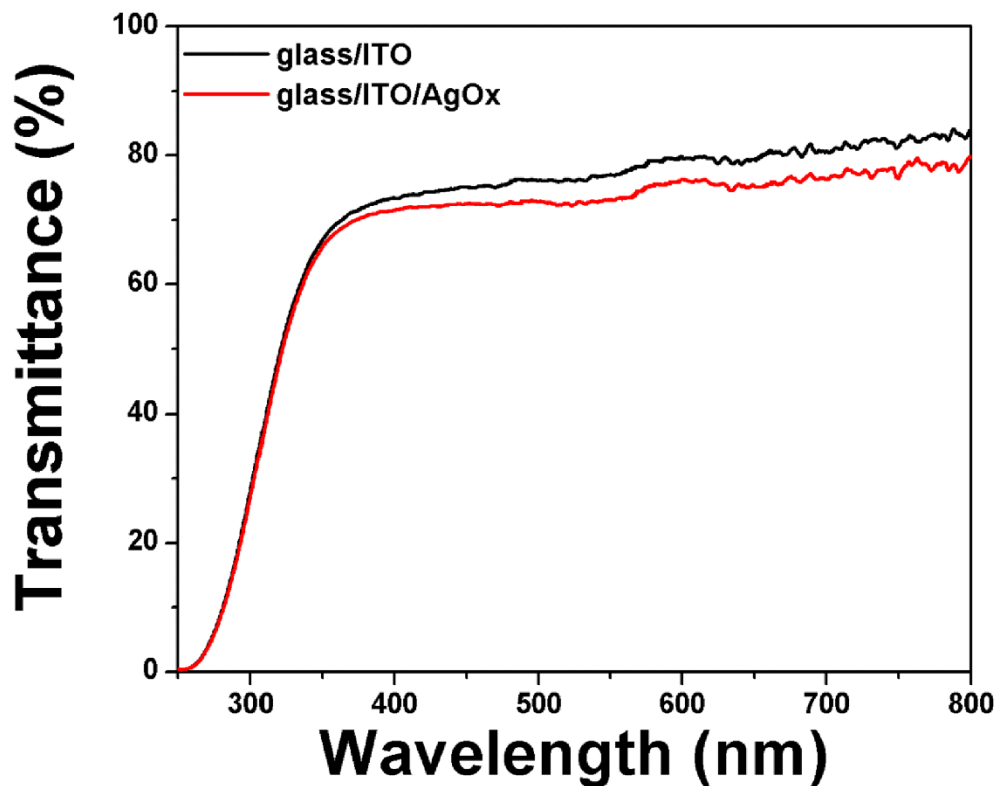
Figure 5.5   Optical transmittance of bare ITO and AgOx/ITO films.

Figure 5.6(a) shows the forward bias current density–voltage (*J-V*) characteristics under darkness where current density is significantly enhanced at a given voltage in case of devices consisting of AgOx as the interfacial layer. The *J-V* characteristics for the devices under AM 1.5G illuminations with an overall intensity of 100 mW/cm^2 is shown in Fig. 5.6(b). As expected, the open circuit voltage (*Voc*) value remains almost the same since the active layer fabrication condition and the cathode layer deposition remain constant. The control device with ITO/PEDOT:PSS anode demonstrated a PCE of 1.74%.

The open circuit voltage (*Voc*) and the current density (*Jsc*) of the control devices were 0.60 V and 8.76 mA/cm^2, respectively. Although the *Voc* and *Jsc* for the devices contenting an AgOx interfacial layer decreased very slightly to 0.58V and 8.64 mA/cm^2, respectively there was a moderate increase in the fill factor (*FF*) of these devices which led to the increase in the PCE. The *FF* in devices consisting of the AgOx interfacial layer was 36% higher when compared to the control devices.
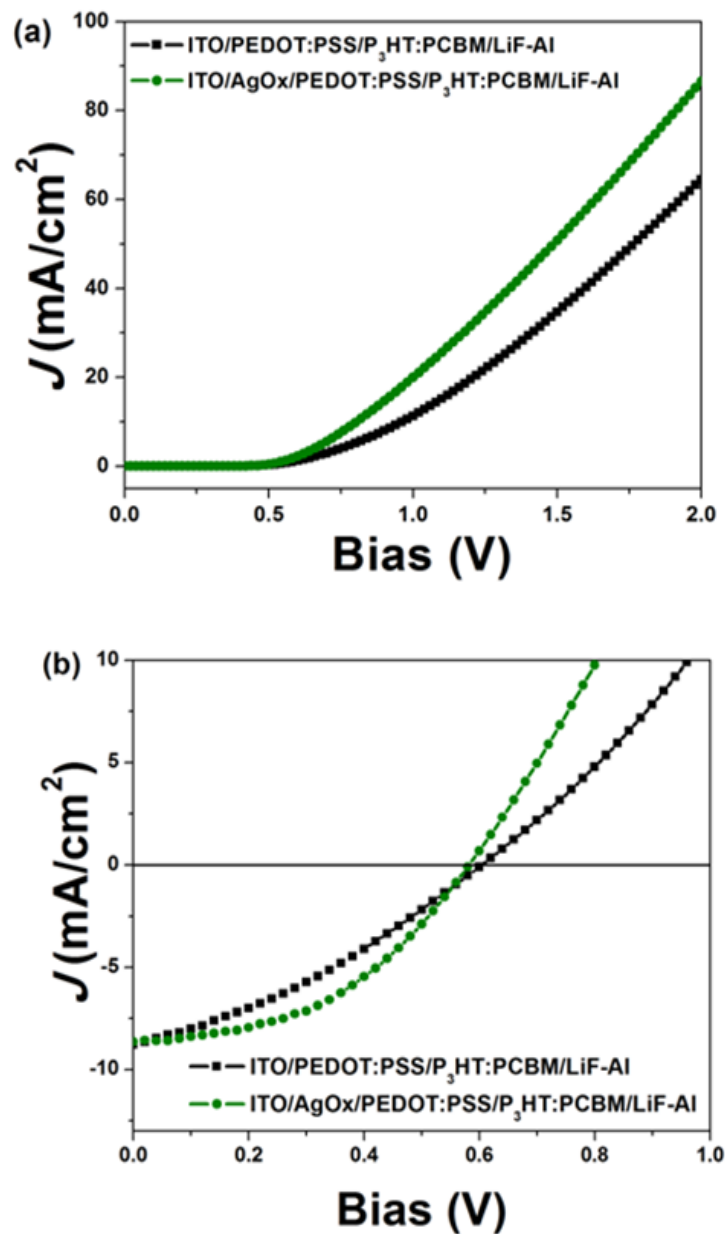
Figure 5.6   Current-density (*J-V*) characteristics of the bulk-heterojunction solar cell with bare ITO and AgOx/ITO anode layer (a) in dark and (b) under illumination (AM 1.5, 100 mW/cm²).

Figure 5.7 shows the EQE results of the devices with and without AgOx interlayer. In the range between 400 and 600 nm, both devices show efficient photoconversion efficiency with EQE values over 50%. However, the application of AgOx shows a slight decrease in the donor contribution to EQE (between 400 nm and 600 nm) and results in slight decrease in the short circuit current (as shown in Table 5.1).
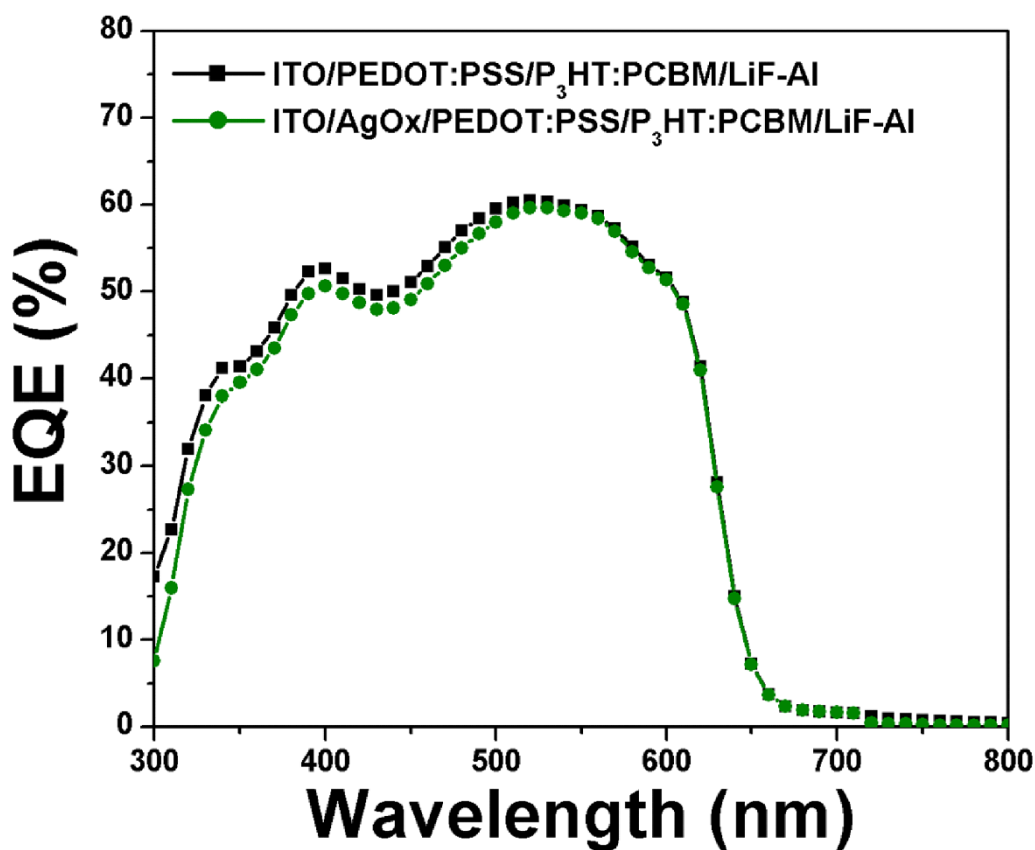
Figure 5.7   External quantum efficiency (EQE) measurement of the P3HT:PC61BM devices using bare ITO and AgOx/ITO anodes.
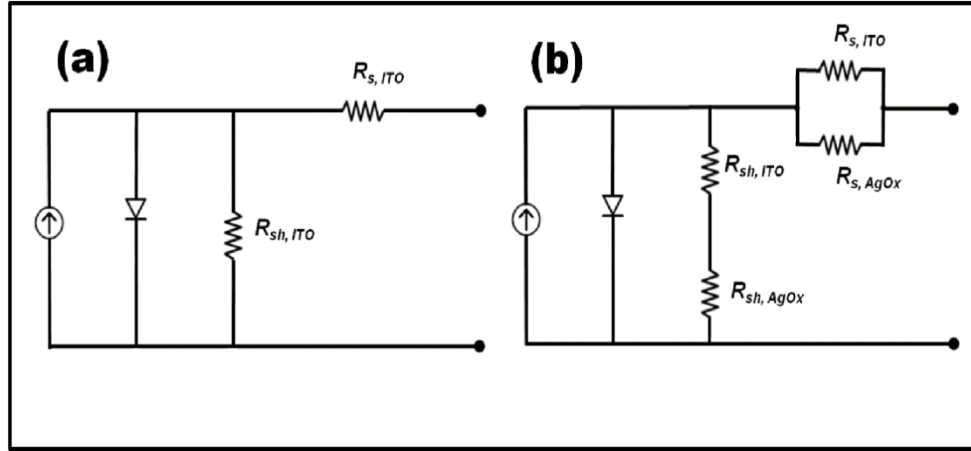
Figure 5.8 Equivalent circuit model for solar cells (a) ITO/PEDOT:PSS/P$_3$HT:PC$_{61}$BM/LiF/Al (b)ITO/AgOx/PEDOT:PSS/P$_3$HT:PC$_{61}$BM/LiF/Al.

When placed under simulated solar illumination, an OSC solar cell may be modeled by an equivalent circuit (EC). This circuit is typically constructed using a single-diode in parallel with a current source as shown in Fig. 5.8 and described in Eq. 5.1 [32]:

$$J = J_{ph} - J_o \left(\exp \left[\frac{q(V + JR_s)}{nk_BT} \right] - 1 \right) - \frac{V + JR_s}{JR_{sh}} \qquad 5.1$$

where J is the current density across the load, J_{ph} is photo-current, J_o is the saturation current under reverse bias, R_S is the series resistance, R_{sh} is the shunt resistance, n is the ideality factor, q is the electronic charge, k$_B$ is Boltzmann's constant and T is the temperature in Kelvin. The source J_{ph} results from the excitation of excess carriers by solar radiation and is proportional to the number of dissociated excitons prior to any recombination. The R_{sh} and R_s are important factors in solar cell devices and are used to quantify the quality of the films and their interfaces. In ideal solar cell devices, the series resistance is close to zero while the shunt resistance approaches a high value. The R_{sh} is

58

due to recombination of charge carriers near donor-acceptor (D/A) interface and at the electrode and is modeled as a leakage current. The charge recombination is a significant parameter and is dependent on ability of the active material to transport separated charge to the electrodes. Series resistance also reflects the ease in which the carrier responds to the electrostatic field (*i.e.,* the mobility) in each specific transport layer and is heavily influenced by the defects and scattering mechanisms. Hence the series resistance depends on the resistivities of the active layer, hole-extraction layer, metal–organic contacts and electrodes. The influence of the interfacial layer on the shunt resistance of the device can be observed in the *J–V* curves around the V_{OC} and around J_{SC}. From the Fig.5.6b, R_s and R_{sh} are evaluated as:

$$R_S = \left(\frac{dV}{dJ}\right)_{V=V_{OC}} \qquad\qquad 5.2$$

$$R_{sh} = \left(\frac{dV}{dJ}\right)_{J=J_{SC}} \qquad\qquad 5.3$$

The shunt and series resistances values are summarized in Table 5.1 for the AgOx device and the reference device. It is should be noted that the solar cell devices with the AgOx interfacial layer had a higher R_{sh} value of 586 Ωcm^2 when compared to the control device which has a shunt resistance value of 150 Ωcm^2. The R_s value also decreases in case of solar cell devices with AgOx interfacial layer. This indicates that the AgOx promotes lower contact resistances of our devices by creating an interfacial step in between PEDOT:PSS and ITO. The lowering of the series resistance has been attributed to the connection of $R_{s,}$ $_{AgOx}$ (series resistance of the device due to addition of AgOx interfacial layer) in parallel to $R_{s, ITO}$ (series resistance in ITO only device). Similarly, the increase in shunt resistance has

been attributed to the $R_{sh, AgOx}$ in series with $R_{sh, ITO}$, where $R_{sh, AgOx}$ and $R_{sh, ITO}$ are shunt resistances in AgOx based devices and ITO only devices, respectively.

TABLE 5.1. Device parameters of organic solar cells having bare ITO and AgOx modified ITO electrode.

Anode	V_{oc}(V)	J_{sc} (mA/cm^2)	FF(%)	PCE(%)	R_s(Ωcm^2)	R_{sh}(Ωcm^2)
ITO	0.60	8.76	33	1.74	28	150
AgOx/ITO	0.58	8.64	45	2.25	18	587

In a previous investigation by Koide *et al.* [32], they compared equivalent circuits for dye-sensitive solar cells to that for the conventional solar cells (see Fig. 5.8 and included additional capacitive and resistive elements in the total series resistance. After considering that the OSC operates in the DC conditions, they found that the only difference was in the configuration of the series resistance elements. Similarly, our model ignored any capacitive elements and observed a difference in both the series resistance and shunt resistance elements. Future work will focus on optimization of the AgOx thickness and the implementation of more sophisticated equivalent circuit models that will help to elucidate the effect of new interfacial layers incorporation. These new models will also be used to characterize and optimize the performance of materials selection and device performance.

5.4.   Conclusions

Incorporation of a AgOx interfacial layer together with PEDOT:PSS effectively extract holes efficiently from the cell by the creation of an interfacial energy step, thus reducing the charge recombination tendency. The devices with the AgOx interfacial layer demonstrated a 2.25% increase in their PCE. This increase was a result of the increase of the fill factor from 33% of the control devices to 45% in the AgOx modified devices even though they displayed a lower *Voc* and *Jsc*. Comparison of the equivalent circuits for the AgOx based device and conventional OSC, revealed that the only difference was in the configuration of the resistance elements.

CHAPTER 6

EFFECT OF Ag LAYER THICKNESS ON THE ELECTRICAL TRANSPORT AND

OPTICAL PROPERTIES OF ZnO/Ag/MoO$_X$ TRANSPARENT COMPOSITE

ELECTRODES AND THEIR USE IN P$_3$HT: PC$_{61}$BM-BASED ORGANIC SOLAR

CELLS

6.1.   Introduction

Developing a new transparent electrode system for photovoltaic devices to replace

indium tin oxide (ITO) is of paramount importance due to the scarcity of indium which

will eventually increase the fabrication costs of future organic solar cells (OSCs) or hybrid

solar cell where glass substrate works as a window to the incident sunlight. Transparent

composite electrode (TCE) consisting of dielectric/metal/dielectric thin films has been

studied in the anticipation of increasing conductivity without significant losses in

transmittance [1-4]. A variety of research has been done using silver (Ag) as the embedded

layer formed through simple sputtering or evaporation because Ag has the lowest room

temperature   resistivity   among   all   metallic   interfacial   layers.   Poly(3,4-

ethylenedioxythiophene):poly(styrenesulfonate) (PEDOT:PSS) is a widely used hole

transport layer (HTL) in OSCs because of its several advantages which include surface

planarization of ITO and high optical transparency [5]. However, the acidic nature of

PEDOT:PSS causes migration of indium from ITO anode into the PEDOT:PSS layer and

also into the active layer of OSCs [6]. In order to address this problem, many studies on

metal-oxide HTLs (WO$_3$ [7], NiO$_x$ [8], V$_2$O$_5$ [9] and MoO$_3$ [9]) as an alternative to

PEDOT:PSS have been studied. In this work, we discuss the effect of Ag mid-layer

thickness on the optoelectrical properties of ZnO/Ag/MoO$_x$ composite electrode and their

application in P$_3$HT:PC$_{61}$BM organic solar cells. The resulting device structure consists of ZnO/Ag/MoO$_x$/P$_3$HT:PC$_{61}$BM/LiF/Al. It should be noted here that the top layer of sputtered MoO$_x$ has been used as a HTL in an attempt to replace PEDOT:PSS. In our experiments, a typical OSC device based on HTL MoO$_x$ (ITO/MoO$_x$/P$_3$HT:PC$_{61}$BM/LiF/Al) was also fabricated and tested for comparison purposes.

6.2.   Experimental details

The glass substrates were cleaned in sequential ultrasonic baths of acetone, methanol, and isopropanol, respectively. ZnO/Ag/MoO$_x$ multilayer structure was deposited on the substrate (2.5×2.5cm^2) at room temperature using combination of RF and DC sputtering method using a constant argon flow. The thickness of the ZnO layer was 20 nm while that of Ag layer was varied between 7, 9 and 11nm. This was followed by deposition of 10 nm MoO$_x$ by RF sputtering on top of ZnO/Ag and ITO films. Photoactive layer was spin-coated from P$_3$HT:PC$_{61}$BM blends (weight ratio of 1:1) dissolved in 1,2-dichlorobenzene at 600 rpm for 1 min, which corresponded to a layer thickness of 250 nm. A LiF(0.7nm)/Al(80nm) cathode was deposited on top of the active by thermal evaporation through a shadow mask at a pressure of $1×10^{-7}$ Torr to produce an active area of 0.2 cm^2.The four-point-probe technique was used to measure sheet resistance of the ZnO/Ag/MoO$_x$ electrode. The optical transmittance of the electrodes was measured in the wavelength range of 350–800 nm. Morphologies of constant underlying ZnO layer with different Ag thicknesses were characterized using field emission scanning electron microscopy (FESEM). Current density-voltage (J-V) measurements were carried under

simulated AM 1.5 global solar irradiation (100mW/cm^2) using a xenon-lamp solar simulator.

6.3.   Results and discussion

Figure 6.1 shows FESEM images of the Ag layers sputtered onto ZnO layer with different Ag thicknesses and is clearly indicative of formation of Ag network.
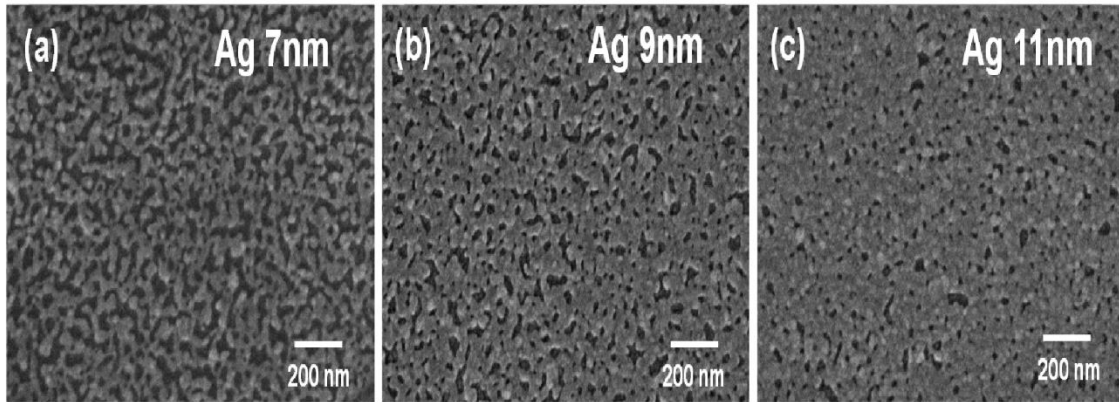
Figure 6.1   FESEM images of Ag layers with thicknesses of (a) 7nm (b) 9nm and (c) 11nm deposited on top of ZnO layer.

The FESEM images represent the evolution of Ag layers as a function of film thickness and portray its potential impact on the electrical conductivity of the ZnO/Ag/MoO$_x$ electrodes. The effect of Ag mid-layer on the optoelectrical properties of multilayer thin films was also studied thoroughly and found that the most critical factor that influences the performance in a composite electrode system is the control of the mid-metal (silver) layer. The effect of Ag mid-layer on the opto-electrical properties of multilayer thin films was studied thoroughly and found that the most critical factor that influences the performance in a composite electrode system is the morphology of the mid-metal (silver) layer. The Ag film growth on crystalline surface follows the Stranski-Krastanov model while on

amorphous oxides like ZnO, it usually follows the island growth mechanism as described by the Volmer-Weber model [10, 11]. During the initial phases of Ag deposition, metallic nuclei of Ag are formed on the ZnO layer. Further deposition leads to nuclei growth and formation of isolated islands. As the thickness of film increases, the isolated islands continue to grow and subsequently merge with every possible adjacent islands. For a 7 nm-thick Ag layer (Figure 6.1(a)), a series of Ag islands and some of them have started to coalesce by increasing contact between islands. As Ag thickness is increased from 7 to 9 nm, all islands coalesce together resulting in the formation of a conductive network. Further Ag deposition induces removal of the space between the network and a continuous Ag film formation occurs for Ag thicknesses greater than or equal to 11nm (Figure 6.1(c)).

Table 6.1 summarizes the sheet resistance and average transmittance of the discussed transparent composite electrodes. Both sheet resistance and transparency decreases with increasing Ag layer thickness. Bare ZnO is highly resistive and hence cannot be used as an electrode material until it contains indium or aluminum dopant in order to get high enough conductivity close to ITO. When a 7 nm Ag film is deposited on top of resistive ZnO, the sheet resistance of the composite film drops considerably and becomes comparable to bare ITO. As the Ag thickness is increased from 7 nm to 9 nm, the sheet resistance gradually decreases down from 57 Ω/sq to 18 Ω/sq. Further increasing the Ag thickness results in the formation of a continuous Ag film and the sheet resistance is recorded to be 11Ω/sq.

The FESEM study shows that the silver layer thickness plays an important role in the morphology of the metal films which in turn influences the conduction mechanism. A detailed study on the conduction mechanism of metal thin films (continuous and

65

discontinuous metal layers) on amorphous oxide surfaces was done by Bieganski *et al* [12].

In case of continuous silver, when all the islands are connected, the resistance (R^m) of the

metallic resistor of length L_1 and width s_1 is given by:

$$R^m = \frac{\rho_{Ag} L_1}{s_1 t}(1 + \alpha_{Ag} T) \qquad\qquad 6.1$$

where, ρ_{Ag} is the resistivity of silver, T is the temperature, α_{Ag} is the temperature coefficient

and t is the thickness of the silver layer. However, in case of discontinuous thin film metal

layers on amorphous oxide surfaces, charge carrier conduction takes place by four different

mechanisms which include (i) metal conduction, (ii) conduction through oxide surface (iii)

quantum tunneling and (iv) thermally activated tunneling. In this case the ratio of metal

surface to the total surface plays an important role in determining the conductivity. The

resistance (R^o) provided by the oxide surface is given by:

$$R^o = \frac{R^o_{sq} L_2}{s_2} \exp\left(\frac{E_a}{k_B T}\right) \qquad\qquad 6.2$$

where, (R^o_{sq}) denotes resistance per square offered by the oxide, L_2 and s_2 are length and

width of the resistor, respectively, E_a is the activation energy of the oxide resistance and k_B

is the Boltzmann's constant. The quantum tunneling resistance (R^t) and the thermally

activated tunneling resistance (R^{ta}) is given by equation 6.3 and 6.4, respectively [12]:

$$R^t = \frac{h^2 L_2}{e^2 (2m\phi)^{1/2} t s_2} \exp\left(\frac{4\pi L_2}{h}(2m\phi)^{1/2}\right) \qquad\qquad 6.3$$

$$R^{ta} = A \exp\left(\frac{E_c}{k_B T}\right) \qquad\qquad 6.4$$

where, e and m denotes electronic charge and mass respectively, h is the Plank's constant, ϕ is the potential barrier height for oxide-Ag system, A is constant and E_c indicates the Coulomb activation energy [12].

Although increasing the Ag layer thickness decreases the sheet resistance of ZnO/Ag/MoO$_x$ composite electrodes, the transmittance of TCE must also be considered as sunlight arriving the photoactive layer is critical to produce excitons. The transmittance of ITO (control electrode) exhibiting high conductivity is shown in Fig.6.2. Transmittance spectra for the ZnO/Ag/MoO$_x$ composite electrode system for three different Ag thicknesses are compared to bare ITO film. The average transmittance of bare ITO film is over 80%. However, in case of ZnO/Ag/MoO$_x$ composite electrodes transmittances drop significantly. The average transmittance for all TCEs is in the range of 60%-50%. The variation in transmittance with silver thickness is different for shorter wavelengths and longer wavelengths as can been seen in Fig. 6.2. In the wavelength range above 600 nm, as the thickness of the silver layer increases, the transmission decreases.
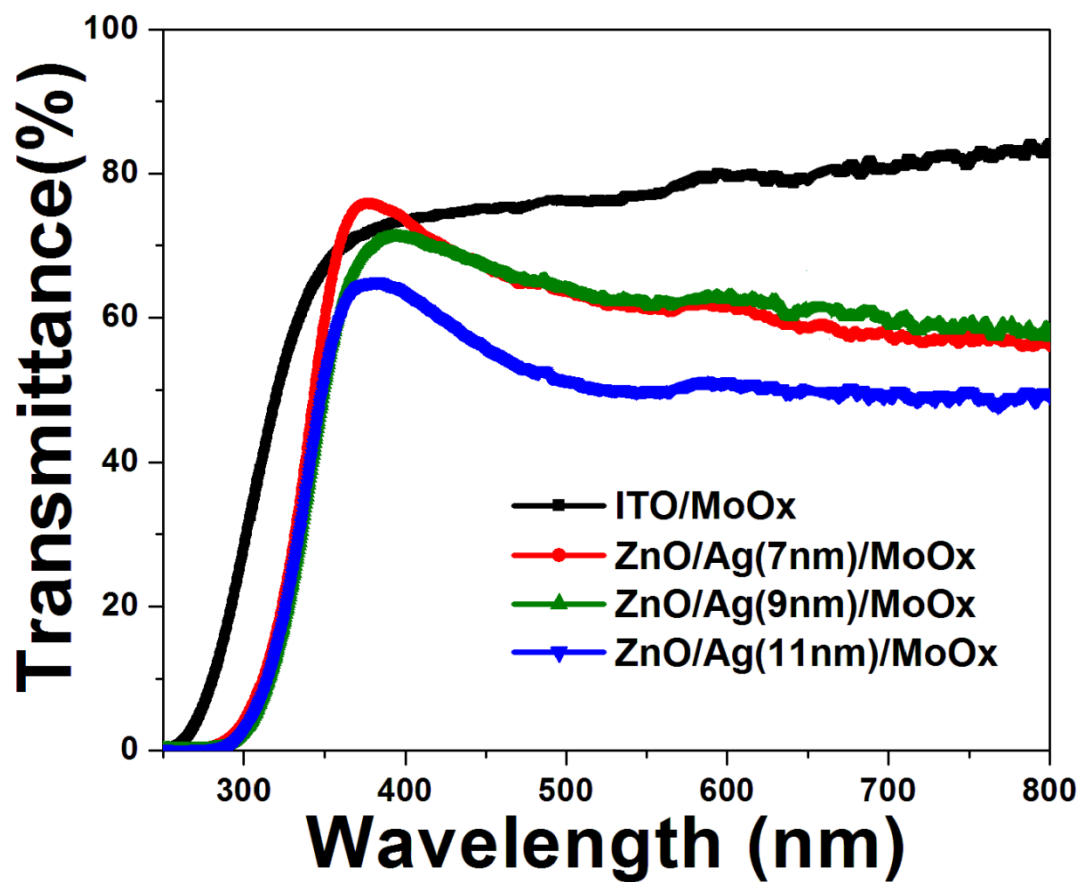
Figure 6.2   Optical transmittance of ITO and ZnO/Ag/MoOx thin films

A figure of merit (FOM) as defined by Haacke [13] was calculated and listed in Table 6.1 for each electrode employed in this study. It shows that the composite electrode having 9 nm-thick Ag layer has the best figure of merit amongst the others reported here.

TABLE 6.1   Sheet resistance and average transmittance of ZnO/Ag/MoOx electrodes with different Ag thickness and ITO electrode for comparison.

Anode	$R_{sh}(\Omega/sq)$	$T_{avg}(\%)$	FOM
ITO(150nm)	20	79	4.7×10^{-3}
ZnO/Ag (7nm)/MoOx	57	61	1.3×10^{-4}
ZnO/Ag (9nm)/MoOx	18	61	3.9×10^{-4}
ZnO/Ag (11nm)/MoOx	11	51	1.1×10^{-4}

Figure 6.3 shows current density–voltage (J–V) characteristics of OSCs consisting of bare ITO and ZnO/Ag/MoO$_x$ composite electrodes on glass substrate as the anode material, having varying thicknesses of the Ag layer, obtained under 100mW/cm^2 intensity of AM 1.5 global solar irradiation.
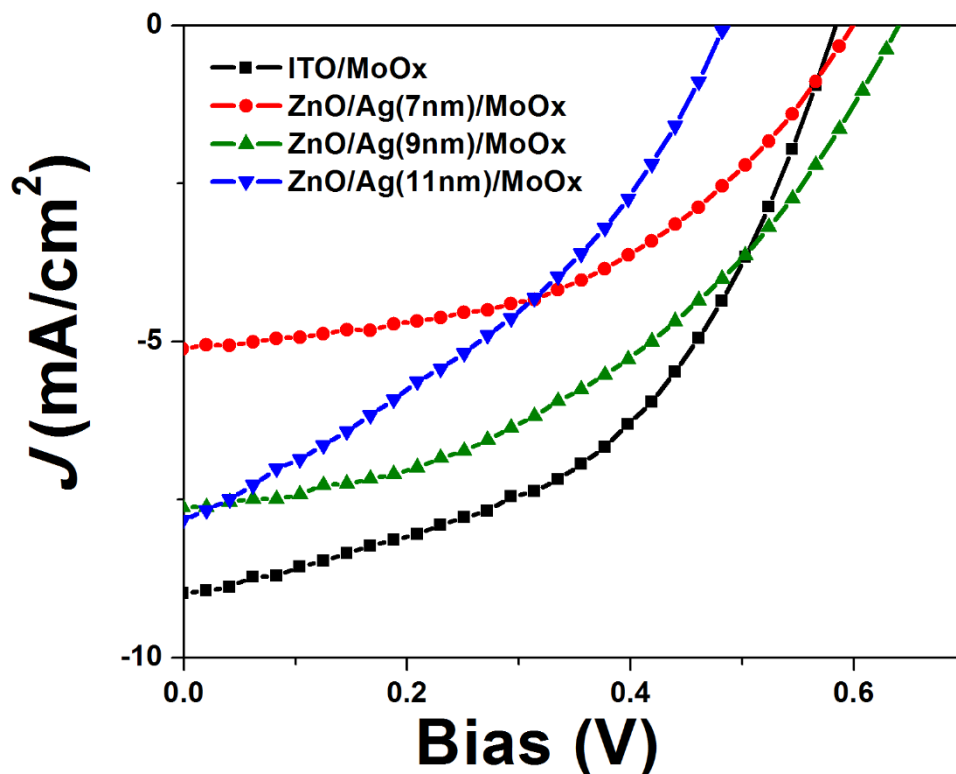
Figure 6.3   Current density–voltage (air mass 1.5 G condition with incident light power intensity of 100 mW/cm^2) characteristics of organic solar cell devices fabricated on transparent composite electrodes.

The short circuit current density (J_{sc}), open-circuit voltage (V_{oc}), fill factor (FF) resulting in power conversion efficiency (PCE) obtained from J–V curves are summarized in Table 6.2 The OSC on ITO substrate shows a V_{oc} of 0.58 V, a J_{sc} of 8.98 mA/cm^2, a FF of 48% and PCE of 2.52%. However, in comparison to the device fabricated on ITO substrate, the best photovoltaic performance is found in the OSC on TCE with the best FOM. The OSC on the composite electrode with silver thickness of 9nm performs a V_{oc} of 0.59 V, a J_{sc} of 7.62 mA/cm^2, a fill factor of 42% resulting in PCE of 1.92%.

TABLE 6.2   Device parameters of organic solar cell with TCE having different Ag thickness and ITO as reference electrode

Anode	$V_{oc}(V)$	J_{sc} (mA/cm^2)	FF(%)	PCE(%)
ITO(150nm)/MoOx	0.58	8.98	48	2.52
ZnO/Ag(7nm)/MoOx	0.55	5.05	47	1.31
ZnO/Ag(9nm)/MoOx	0.59	7.62	42	1.90
ZnO/Ag(11nm)/MoOx	0.44	7.67	36	1.21

6.4   Conclusions

In conclusion, we have evaluated the characteristics of indium-free ZnO/Ag/MoO$_x$ composite electrode deposited by in situ RF/DC sputtering method at room temperature and illustrated its application as an anode in OSCs. This fabrication process represents a route for low-cost organic electronic and photovoltaic devices. The important TCE parameters that determine the optoelectrical properties were the thickness and morphology of the mid-metallic (Ag) layer. Initial growth of Ag islands to the formation of continuous Ag film has also been discussed. The organic photovoltaic device showing the best performance has a PCE of 1.92% which is still lower than the 2.52 % for ITO-based OSC due to the reduced transmittance of the composite electrode. Although, the results shown here are surely not the best possible but has shown a promising way to make precise and low-cost anode for organic electronic devices. In a field of transparent conducting electrode, our contribution brings light to device engineers and satisfies great needs of an alternative to ITO in the rapidly growing field of organic photovoltaics. Moreover it also

allows us to develop a new device architecture which requires less process steps and easier

process method.

CHAPTER 7

OPTIMIZATION OF THE ZINC OXIDE ELECTRON TRANSPORT LAYER IN

$P_3HT:PC_{61}BM$ ORGANIC SOLAR CELLS BY ANNEALING AND YTTRIUM

DOPING

7.1   Introduction

Until today the civilized society is almost entirely dependent upon fossil fuels for

nearly every part of its existence. However, it becomes quiet unpleasant to realize that at

some point the fossil fuels are going to be extinct or become too expensive for an average

person to use it [1]. Moreover, the uncontrolled use of fossil fuels has also increased carbon

dioxide (CO_2) emissions causing increased average global temperature [1]. This has led to

the increasing demand for cheap, renewable and clean energy source across the globe and

organic solar cells (OSCs) are one of the promising solutions [2-5]. In OSCs, a blend of

regioregular poly(3-hexylthiophene) (P_3HT) and the fullerene derivative [6,6]-phenyl-C61

butyric acid methyl ester ($PC_{61}BM$) forms a phase-separated (BHJ) nanostructure which

offers a large interfacial area for efficient exciton dissociation and is also the most widely

researched donor and acceptor materials [5]. Recently, Guo *et al* fabricated and

characterized $P_3HT:PC_{61}BM$ based OSCs under AM0 (stands for air mass zero)

illumination for testing its potential use in space applications [6]. These materials have the

potential to be manufactured cheaply as flexible large area sheets with low-cost materials

at low temperature using roll-to-roll processes [7-11]. However, in order to become

marketable and start to make an impact in power generation, several obstacles must first

be overcome such as lower efficiencies than commercially available Si solar cells and

relatively short OSC lifetimes due to degradation [12-16].

In case of OSC devices the energy level alignment at the interfaces between each layer plays a crucial role in determining the short circuit current (J_{sc}), open circuit voltage (V_{oc}), and fill factor (FF) [17]. For example, in case of OSCs, the presence of non-ohmic contacts in between electrode and the organic layers may result in a lower V_{oc}, while application of interfacial layers resulted in enhanced V_{oc} [17-20]. Furthermore, interfacial layers helps in the improvement of the charge collection efficiency and decrease in the interfacial contact resistance which leads to smaller series resistance (R_s) and larger shunt resistance (R_{sh}) [17, 21, 22].

In the inverted structure of OSCs, a high work function metal like silver is used as a hole collecting electrode, while the n-type metal oxides such as SnO_2, TiO_2 and ZnO are used as the electron transport layer (ETL) [23-25]. Among the metal oxides, ZnO serves as an excellent ETL due to its high electron mobility, good transparency, availability, non-toxicity, and hole blocking properties [25]. Pure ZnO has been widely used in organic/polymer based solar cells, perovskite based solar cells and dye sensitized solar cells [26-28]

Recently, in order to increase the device performance of inverted solar cells, several groups have studied the use of metal doped n-type buffer layers. Metal doping is an efficient technique to modify the optical and electrical properties of ZnO layers [29]. Dopant atoms such as Al, Ga, In, Sn, Ta and Y have been explored as potential n-type dopants for ZnO; because, they can replace the Zn sites in the ZnO crystal and generate free electrons [30-35].

Here we report the effects of ZnO processing temperature on the photovoltaic properties of inverted solar cells with the structure of ITO/ZnO/P$_3$HT:PC$_{61}$BM/MoO$_x$/Ag/Al. The best device performance is observed with the ZnO layers annealed at 150 °C despite the fact that higher temperatures leads to improvement in thin film crystallinity and electron mobility [36]. We further investigated the use of yttrium as a doping impurity to enhance the electron transport properties in the ZnO films. The efficiency of solar cells has further been improved by using optimized concentration of yttrium ions in the ZnO (YZO) film enabling them to become excellent electron transport layers.

7.2   Experimental Details

7.2.1. Preparation of zinc oxide and yttrium-doped zinc oxide precursor solution:

ZnO and yttrium doped ZnO precursor solution was prepared by dissolving 0.5 M zinc acetate dihydrate ((Zn(CH$_3$CO$_2$)$_2$.2H$_2$O) in N,N-dimethylformamide (99.8%, Sigma–Aldrich) with monoethanolamine (MEA) as chelating agent (stabilizer). YCl$_3$.6H$_2$O in different amounts was added into the solution and the mixture solution was then stirred on a hot plate at 60 °C for about 1 h until the solution changed to a clear transparent solution. This solution was then aged for a day before further use.

7.2.2 Device Fabrication: All devices in this work were prepared on 40Ω sq^{-1} ITO coated glass substrates. The substrates were cleaned in sequential ultrasonic baths of acetone, methanol, and isopropanol, followed by ultraviolet ozone (UVO) treatment for 10 min. The ZnO/YZO precursor solution was spin coated at 3000 rpm for 60s onto cleaned patterned ITO substrate. The precursor solutions was then subjected to heat treatment at various temperatures for an hour (discussed later) on a hot plate in order to convert the precursor

75

materials into ZnO/YZO. Immediately prior to the active layer ($P_3HT:PC_{61}BM$) deposition, ultraviolet ozone (UVO) treatment for 2 min was performed on the ZnO/YZO layers to remove organic residues that might be present on the ZnO/YZO surface. Photoactive layers were then spin-coated from $P_3HT:PC_{61}BM$ blends dissolved in 1, 2- dichlorobenzene (DCB) in 1:1 weight ratio at 600 rpm for 1 min. The photoactive layer (150 nm) was then dried at 150 °C for 15 min. In addition, after spin-coating, the photoactive layer was left inside the N_2 filled glove box for 24 h to increase P_3HT ordering. The device structure was completed by evaporating MoOx (10nm)/Ag (10 nm)/Al (70 nm).

7.2.3. Characterization of the ZnO layer: X-ray diffraction (XRD) patterns were recorded at room temperature using a Philips X'PertPro diffractometer equipped with a Cu Kα radiation (λ = 1.54056 Å). A working voltage of 45kV was employed with a filament current of 40mA. Surface morphology of the ZnO layers on ITO was acquired by using atomic force microscopy (AFM). The optical transmittance of glass/ITO/ZnO and ITO/YZO thin films were measured using Ocean Optics double channel spectrometer (model DS200) in a wavelength range of 300–800 nm.

7.2.4. Device Characterization: Current density-voltage (*J-V*) measurements were performed under simulated AM 1.5 global solar irradiation (100 mW/cm^2) using a xenon-lamp solar simulator (Spectra Physics, Oriel Instruments, USA). The light source was calibrated with a standard Si photodiode reference cell (Hamamatsu Photonics, Japan) prior to measurement

7.3   Results and Discussion

7.3.1   *Effect of annealing temperature on ZnO thin films and corresponding solar cell performance*

Figure 7.1 demonstrates the electronic structure of the inverted solar cells. In this inverted structure, electrons are transferred from $PC_{61}BM$ to the ITO/ZnO cathode and holes in P_3HT towards the MoOx/Ag/Al anode. Organic stabilizers like monoethanolamine (MEA) used during ZnO film formation needs to be removed before the deposition of the active layer (P_3HT: $PC_{61}BM$) to enhance the electronic contact between the ETL and the active layer as well as that among ZnO grains [37]. Earlier reports suggest that a short UVO treatment can effectively remove the organic capping agents and improve electronic coupling among the ZnO grains thus improving solar cell efficiency [37-39]. Nevertheless, prolonged UVO treatment reduces the number of free electrons in the conduction band by filling the oxygen atom vacancies with an adverse effect on the device performance [40].
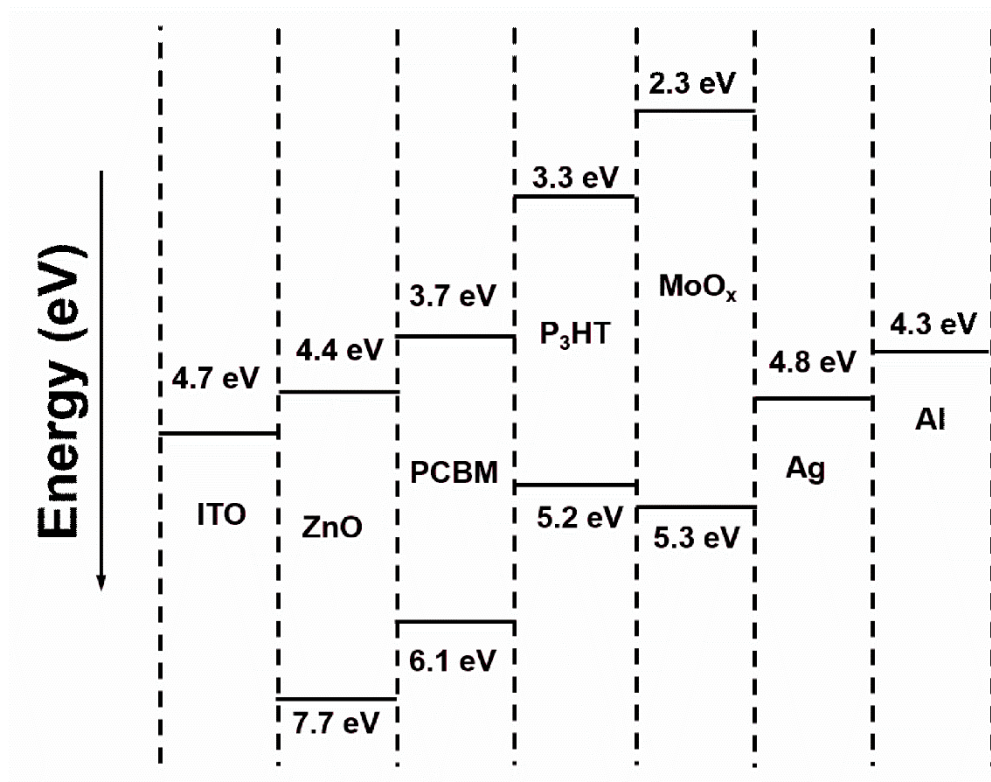
Figure 7.1   Energy level diagram of different components of the devices

Table 7.1 summarized the data derived from the *J–V* characteristics of the solar cell devices fabricated using solution processed ZnO layer annealed at different temperatures. By inspecting the device properties we were able to observe effect of annealing the ZnO layer after spin coating. The OSCs utilizing ZnO ETL annealed at 50 °C exhibited a PCE of 1.28% with a V_{oc} of 0.59 V, a J_{sc} of 7.78 mA cm^{-2}, and a fill factor (FF) of 27.8%. The OSCs fabricated with ZnO layers annealed at 150 °C showed significant improvement in the PCE by ~70% to 2.18% (V_{oc} = 0.60 V, J_{sc} = 8.72 mA cm^{-2}, and FF = 41.7%). Higher temperature annealing treatments of ZnO layer however showed continuous depreciation in cell performance, and the PCE became 1.00% for the cells with ZnO annealed at 450 °C.

78

TABLE 7.1   Device parameters of ZnO based inverted organic solar cells under illumination (average of five devices)

ZnO anneal Temperature (^{O}C)	V_{oc} (V)	J_{sc} (mA/cm^2)	FF(%)	R_{sh} ($\Omega.cm^2$)	R_s ($\Omega.cm^2$)	PCE(%)
50	0.59	7.78	27.8	130	39	1.28
150	0.60	8.72	41.7	510	13	2.18
300	0.60	8.76	32.9	150	28	1.73
450	0.48	6.64	31.4	92	9	1.00

In solar cell devices, R_{sh} and R_s are important parameters and often used to quantify the quality of the films and their interfaces. In an ideal situation, the series resistance is close to zero while the shunt resistance approaches a large value. The R_s depends on the resistivity of the different layers in the OSC and electrodes while the R_{sh} depends on recombination of charge carriers occurring near the different interfacial layers and at the electrode [21]. We thus hypothesize here that the excessive heat treatment can modify the surface properties of the ZnO layer, affecting the performance of the cells. At first instance it is expected that a higher crystallinity will lead to better electron transport and reduced R_s. In fact the R_s value of the device decreases when ZnO layer is annealed from 50 °C to 150 °C and the PCE increased. However, further increasing the annealing temperature from 150 °C to 450 °C results in a drop in the R_{sh}, indicating higher leakage current resulted from higher surface roughness of ZnO ETLs. Table 7.1 suggests that only optimum thermal treatment of the ITO covered ZnO layer is beneficial for the cell performance whereas excessive annealing of the ZnO layer deteriorates the device performance.

To investigate the effect of different annealing temperature on the surface roughness of the ZnO thin films, samples annealed at 150 °C and 450 °C are investigated

by AFM. Figure 7.2(a) and (b) are AFM images of the single layer ZnO film on glass substrates prepared by annealing at 150 °C and 450 °C, respectively. The ZnO film annealed at 450 °C is comparatively rougher with a root-mean square (rms) roughness of 5.7 nm than the film annealed at 150 °C (rms of 2.2 nm). In organic solar cell structures the smoother surface is expected to facilitate a uniform interfacial contact between the ETLs and active layers, thus increasing the electron collection efficiency.
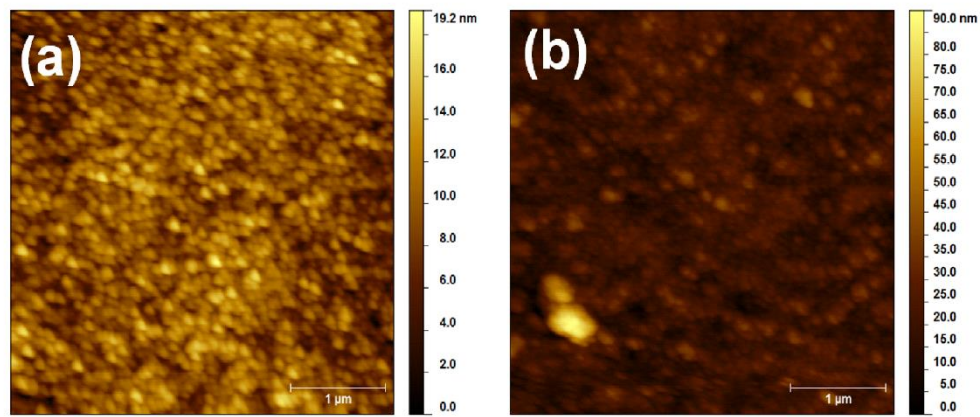
Figure 7.2   4×4 µm^2 tapping mode AFM images of single layer ZnO film on glass substrates annealed at (a) 150 °C and (b) 450 °C, respectively.

The structure of the ZnO was verified by spin coating the precursor solution multiple times on glass substrates followed by annealing on a hot plate for 150 °C, 300 °C and 450 °C. The structure of the ZnO films were evaluated using x-ray diffraction (XRD) method. The precursor solution was spin coated on glass substrate six times followed by annealing at different temperatures for 1 hour. Figure 7.3 shows the XRD patterns of ZnO thin films on glass substrates and confirms that samples annealed at 150 °C had amorphous structures, whereas samples annealed at 300 °C and 450 °C shows a pronounced ZnO peak at 34.4° (2θ) corresponding to the (002) reflection of the hexagonal cubic wurtzite structure

80

(JCPDS card No. 79-2205) [41]. The *c*-axis lattice constant of ZnO films was found to be 0.52 nm.
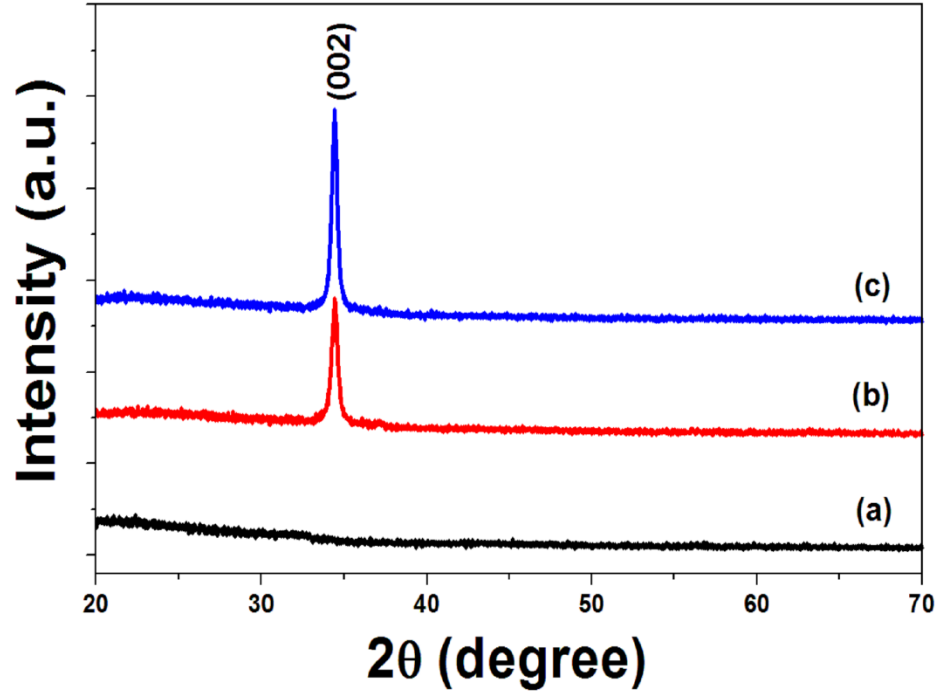
Figure 7.3   XRD patterns of ZnO on glass substrate prepared by annealing at (a) 150 °C (b) 300 °C and (c) 450 °C.

The optical transmittance of glass/ITO/ZnO films annealed at different temperatures shows good optical transmittance in the visible region. Figure 7.4 shows no significant difference in transmittance values regardless of the annealing temperature except the one annealed at 450 °C which might be due to degradation of ITO [42].
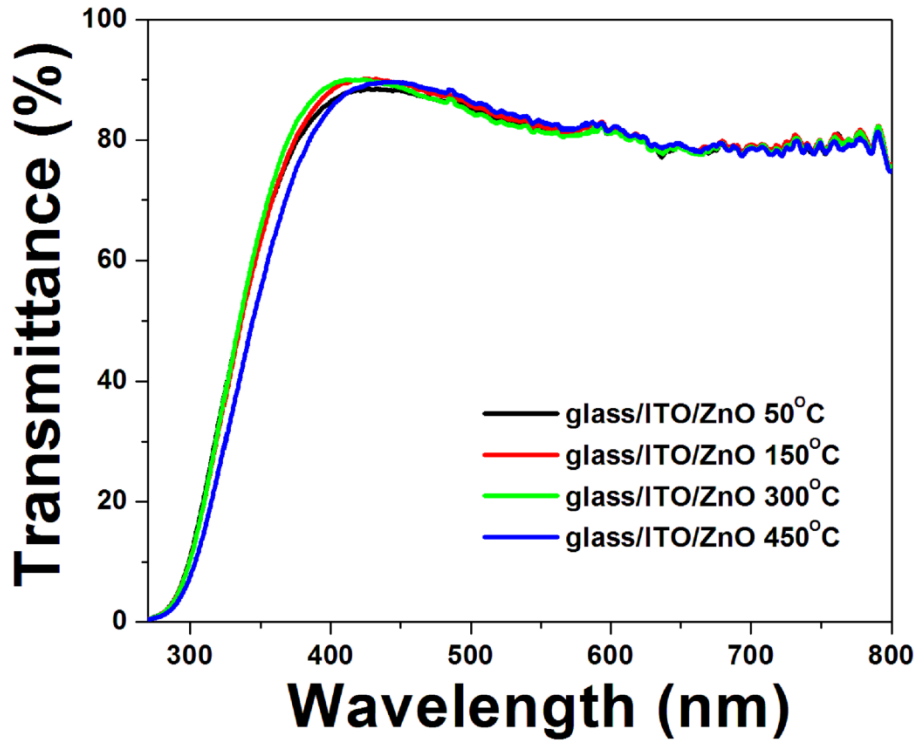
Figure 7.4   Optical transmission spectra of sol-gel prepared single layer ZnO on ITO coated glass substrates annealed at different temperatures.

7.3.2   Effect of yttrium doping of ZnO thin films on the efficiency of OSCs

It has been reported previously that the resistivity of ZnO films further decreases after doping with yttrium ions; however, excessive doping leads to increase in the resistivity of the films [33, 43]. At low doping concentrations Y^{3+} ion substitutes the Zn^{2+} lattice sites as donors, resulting in an increased number of charged carriers, but beyond a

critical limit carrier concentration saturates and resistivity starts to rise due to enhanced scattering from the dopant ions [44]. Thus, to investigate the effects of doping in zinc oxide for the inverted OSCs, different concentrations of the n-type dopant (Y^{3+}) was added to the zinc oxide precursor solution and spin coated on top of ITO layer, followed by annealing at 150 °C on a hot plate inside the glove box. Fig. 7.5 illustrates the UV-Vis absorption spectra of various YZO thin films and indicates that the transmittance spectra have no significant difference regardless of the amount of yttrium added. All the ZnO/YZO films have good optical transmittance in the visible region. It might be because the YZO films are very thin and could be considered as completely transparent. Thus the introduction of various amounts of yttrium in ZnO layers has no significant effect to the UV-Vis absorption spectra.
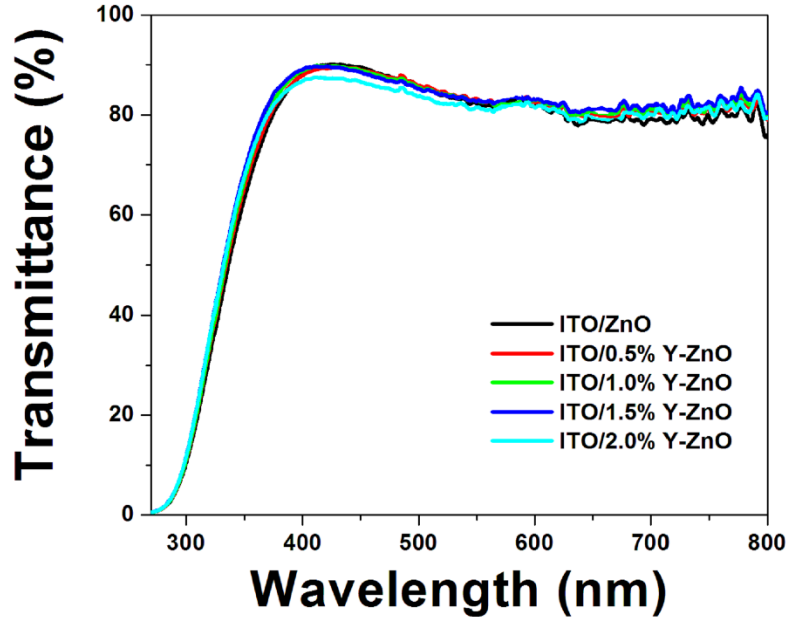
Figure 7.5   Optical transmission spectra of sol-gel prepared ZnO and Y-doped ZnO layers on ITO coated glass substrates

The *J–V* characteristics of the P₃HT:PC₆₁BM based OSCs fabricated using ETLs of ZnO and YZO are shown in Fig. 7.6 and the data derived from it is illustrated in Table 7.2. As reported earlier the OSC device with ZnO exhibits a J_{sc} of 8.72 mA cm^{-2}, V_{oc} of 0.60 V, FF of 41.7% and PCE of 2.18%. The OSC incorporating an ETL composed of 0.5 at.% Y-doped ZnO exhibits an improved photovoltaic response with J_{sc} of 9.19 mA cm^{-2}, Voc of 0.59 V, FF of 49.2% and thus a PCE of 2.66%. The efficiency of the inverted organic solar cell fabricated with 1.0 at. % Y-doped ZnO exhibited the best photovoltaic performance among all the devices, with PCE of 2.85%, J_{sc} of 9.81 mA cm^{-2}, V_{oc} of 0.59 V and FF of 49.3%. Further increase in the yttrium concentration beyond 1 at. % leads to slight depreciation of the device performance as evident from their PCE values.
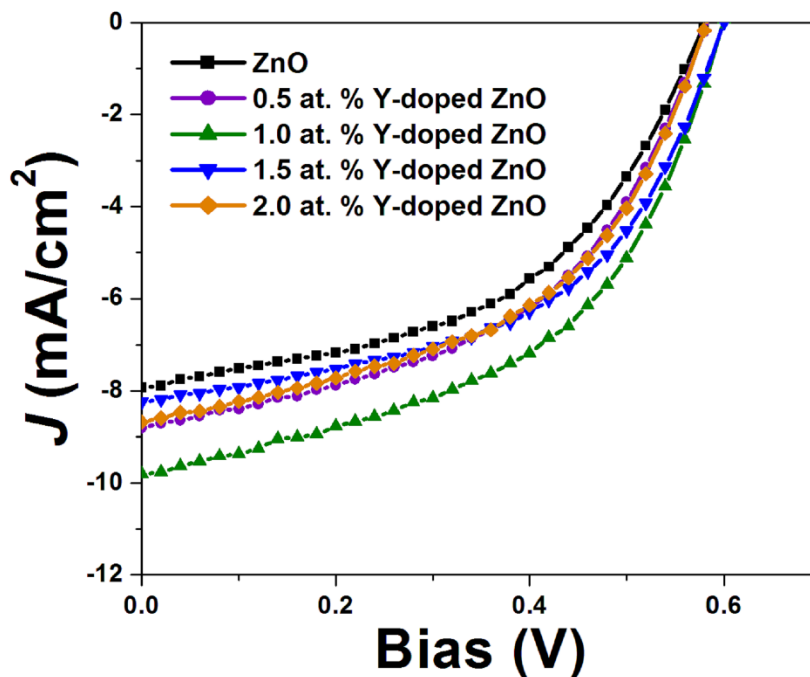
Figure 7.6   Current density-voltage (J–V) characteristics of the ZnO and Y doped ZnO based OSC devices under illumination.

It is observed that increasing the Y-concentration from 0 to 1.0 at. % leads to improvement in the solar cell performance by ~30%. The increase in fill factor from 41.7% to 49.3% has also been attributed to improved electron–hole mobility in the device [45]. This significant enhancement of the PCE in YZO based devices could be attributed to the improved mobility of the YZO ETLs as compared to the ZnO ETL, thus increasing the J_{sc}. Moreover, the R_s value of all the YZO based devices are significantly lower than the ZnO based devices resulting in increased PCE values. These results indicate that power conversion efficiency of the ZnO based devices can be improved through Y-doping of the ZnO layer, however; it is also noted that exceeding the Y doping beyond 1.0 at. % leads to the decrease in the device performance.

TABLE 7.2 **Device parameters of Y doped ZnO based inverted organic solar cells under illumination (average of five devices)**

ETL	V_{oc}(V)	J_{sc}(mA/cm^2)	FF(%)	R_{sh}(Ω.cm^2)	R_s(Ω.cm^2)	PCE(%)
ZnO	0.60	8.72	41.7	510	13	2.18
0.5% YZO	0.59	9.19	49.2	283	7	2.66
1.0% YZO	0.59	9.81	49.3	254	6	2.85
1.5% YZO	0.60	8.98	51.5	334	9	2.77
2.0% YZO	0.60	8.99	50.3	258	6	2.71

7.4 Conclusions

In this study, the performance of ZnO ETLs in ITO/ZnO/P$_3$HT:PC$_{61}$BM/MoOx/Ag/Al structures with optimized annealing conditions was reported through characterization of the surface morphology, thin film crystallinity, and optical and device properties. It was found that the proper ZnO annealing condition plays a dominant role in determining the device performance for sol–gel processed ZnO.

Based on these findings, an approach to fabricate and optimize high-efficiency P$_3$HT:
PC$_{61}$BM solar cells was determined by using yttrium-doped zinc oxide as the ETL. Our
results in this work suggest that such a doping approach can provide a brilliant solution for
the enhancement of PCE in organic solar cells, however optimum doping conditions should
be maintained to observe best device performance. This study showed that by doping an
optimized amount of yttrium into zinc oxide layer resulted in a 30% enhancement of PCE.
This implies that interfacial engineering is a promising approach for manipulating the
efficiency of organic/polymer based solar cells in low-cost roll-to-roll manufacturing.

CHAPTER 8

CONCLUSIONS AND FUTUTRE WORK

8.1   Conclusions

There is a critical need for low-cost, large area, organic solar cells. However to fully enable this technology's use in harvesting the sun's energy, the low efficiency of organic solar cells has to be eradicated. The aim of this work was to enhance the efficiency of organic solar cells based on regioregular poly(3-hexylthiophene) (P3HT) used as donor and fullerene derivative [6,6]-phenyl-C61-butyric acid methyl ester ($PC_{61}BM$). Efforts were taken to introduce new hole and electron transport materials for organic and organic/inorganic hybrid solar cells. Additional attempt was made to replace the expensive ITO based electrodes with oxide/metal/oxide based trilayered electrodes.

In chapter 3 it has been demonstrated here that a self-assembled monolayer of HMDS on ITO electrodes can enhance the efficiency of organic solar cells when compared to a device fabricated on bare ITO thin film. The surface morphology of the bare ITO and HMDS modified ITO are also comparable. These results encourage the use of a more efficient photoactive system to obtain higher PCEs to fabricate the organic solar cells using HMDS modified ITO electrodes.

Preliminary results demonstrated in chapter 4 suggests that solution processed CuI hole transport layer is a viable alternative to the acidic and more expensive PEDOT:PSS. This work implies that CuI is a promising hole transport layer material and can probably reduce the fabrication time of polymer solar cells in low-cost roll-to-roll manufacturing. The amount of CuI in the solution has been optimized in the work.

Chapter 5 demonstrates the incorporation of a AgOx interfacial layer together with PEDOT:PSS effectively extract holes efficiently from the cell by the creation of an interfacial energy step, thus reducing the charge recombination tendency. Silver oxide was formed by oxidizing a thin film of silver in an ultraviolet ozone chamber. The devices with the AgOx interfacial layer showed increase efficiency compared to the controlled device. This increase was a result of the increase of the fill factor from 33% of the control devices to 45% in the AgOx modified devices even though they displayed a lower *Voc* and *Jsc*.

In chapter 6, the opto-electrical properties of $ZnO/Ag/MoO_x$ composite electrodes are demonstrated. The electrodes have been deposited by in situ RF/DC sputtering method at room temperature. The electrodes have further been used as an anode in organic solar cells. This fabrication process represents a route for low-cost organic electronic and photovoltaic devices. The important electrodes parameters that determine the optoelectrical properties were the thickness and morphology of the mid-metallic (Ag) layer. Initial growth of Ag islands to the formation of continuous Ag film has also been discussed. The organic photovoltaic device showing the best performance has a PCE of 1.9% which is still lower than the 2.52 % for ITO-based OSC due to the reduced transmittance of the composite electrode. Although, the results shown here are surely not the best possible but has shown a promising way to make precise and low-cost anode for organic electronic devices.

8.2   Future Work

A lot of work with an attempt to increase the efficiency of solar cells has been reported so far by using different materials as hole transport or electron transport materials or my doing interfacial modifications. However, surface modifications of these buffer layers using different self-assembled monolayers (SAM) have not been reported a lot. It is

anticipated that systematic improvement of the efficiency of bulk heterojunction solar cells is possible by using SAM which modifies the work function of the oxides. The understanding of electron withdrawing and electron donating groups to be used as SAM will be used to select molecules for proper work function modification. Metal oxides have the flexibility to be modified by carboxylic acids, alcohols, thiols etc. which makes it easier to tune the interfacial properties and study their effect in the BHJs efficiency. MoOx will be used as the hole transport/electron blocking layer for a conventional organic solar cell structure while ZnO/YZO will be used as the electron transport/hole blocking layer for an inverted solar cell structure. For conventional structures, MoOx surfaces (used as hole transport layers) can be modified with para-substituted benzoic acids with different type of substituent to form SAM. For inverted structures, ZnO/YZO used as electron transport layer will be modified in a similar way as described for MoOx.

Fabricating cheap and stable electrodes consisting of cheap metals like aluminum and copper is also of foremost importance to reduce the cost of manufacturing. The different composite electrodes to be studied for organic solar cells are: ZnO/Cu/MoOx, ZnO/Al/MoOx, ZnO/Al/AlOx, ZnO/Cu/CuOx. Metals after certain thickness becomes opaque to visible light, however thin metal films have sufficient transparency towards visible light. Thus proper thickness optimization of Al, Cu, Al-Cu alloys to be used as transparent electrodes is also very essential.

REFERENCES

Chapter 1

1)   P. V. Kamat, J. Phys. Chem. C, 111, 2834 (2007).

2)   C. B. Hartfield, Nature 387, 121 (1997).

3)   M. S. Dresselhaus, I. L. Thomas, Nature, 414, 332 (2001).

4)   S. A. Holditch, R. R. Chianelli, MRS Bulletin, 33, 317 (2008).

5)   H. Matthews, N. Gillett, P. Stott, K. Zickfeld, Nature 459, 829 (2009).

6)   M. Meinshausen, N. Meinshausen, W. Hare, S. C. B. Raper, K. Frieler, R. Knutti, D. J. Frame, M. R. Allen, Nature 458, 1158 (2009).

7)   D. P. van Vuuren, M. Meinshausen, G.-K. Plattner, F. Joose, K. M. Strassmann, S. J. Smith, T. M. L. Wigley, S. C. B. Raper, K. Riahi, F. de la Chesnaye, M. G. J. den Elzen, J. Fujino, K. Jiang, N. Nakicenovic, S. Paltsev, J. M. Reillyo, Proc. Natl Acad. Sci. USA 105, 15258 (2008).

8)   P. Friedlingstein, R. M. Andrew, J. Rogelj, G. P. Peters, J. G. Canadell, R. Knutti, G. Luderer, M. R. Raupach, M. Schaeffer, D. P. van Vuuren and C. Le Quéré, Nature Geoscience, 7, 709 (2014).

9)   M. A. Green, K. Emery, Y. Hishikawa, W. Warta and E. D. Dunlop, Prog. Photovolt: Res. Appl. 23, 805 (2015).

10)   H. J. Moller, *Semiconductors for solar cells*; Artech House: Boston, 1993.

11)   N. W. Aschcroft, N. D. Mermin, *Solid State Physics*; Brooks Cole: New York, 1976.

12)   W. Shockley, H. J. Queisser, *J Appl. Phys. 32,* 510(1961)

13)   H. Hoppe and N. S. Sariciftci, J Mater. Res. 19, 1924 (2004).

14)   G.A. Chamberlain: Organic solar cells: A review. *Solar Cells* 8, 47 (1983).

15)   C. W. Tang, Appl. Phys. Lett., 48, 183 (1986).

16)   A. Goetzberger, C. Hebling, and H-W. Schock. *Mater. Sci. Eng. R* 40, 1 (2003).

17)   C. J. Brabec, Sol. Energy Mater. Sol. Cells, 83, 273 (2004).

18)   *Semiconducting Polymers*, edited by G. Hadziioannou and P.F. van Hutten (Wiley-VCH, Weinheim, 2000).

19)   B. Ratier, J.-M. Nunzi, M. Aldissi, T. M Kraft, E. Buncel, Polym. Int. 61, 342 (2012).

20)   D. L. Morel, A .K. Gosh, T. Feng, E. L. Stogryn, P. E. Purwin, R. F. Shaw, and C. Fishman, Appl. Phys. Lett. 32, 495 (1978).

21)   C. Winder and N. S. Sariciftci, J. Mater. Chem.14, 1077 (2004).

22)   G. Yu and A. J. Heeger, J. Appl. Phys. **78,** 4510 (1995).

23)   J. D. Servaites, M. A. Ratner, T. J. Marks, Energy Environ. Sci., 4, 4410 (2011).

24)   B. ORegan, M. Gratzel, Nature, 352, 737 (1991)

25)   N.S. Sariciftci, L. Smilowitz, A.J. Heeger, F. Wudl, Science, 258, 1474 (1992).

26)   G. Li, V. Shrotriya, J. Huang, Y. Tao, T. Moriarty, K. Emery, Y. Yang, Nature Materials 4, 864 (2005).

27)   H. C. Lee, O. O. Park, Vacuum 75, 275 (2004).

28)   A. El Hichou, A. Kachouane, J. L. Bubendorff, M. Addou, J. Ebothe, M. Troyon, A. Bougrine, Thin Solid Films 458, 263 (2004).

29)   Y. H. Kim, C. Sachse, M. L. Machala, C. May, L. Muller-Meskamp, K. Leo, Adv. Funct. Mater. 21 1076 (2011).

30)   B. Zimmermann, M. Glatthaar, M. Niggemann, M. K. Riede, A. Hinsch, A. Gombert, Sol. Ener. Mater. Sol. Cells 91 374 (2007).

31)   J. Wu, H. A. Becerril, Z. Bao, Z. Liu, Y. Chen, P. Peumans, Appl. Phys. Lett. 92, 263302 (2008).

32)   H.-K. Park, J.-W. Kang, S.-I. Na, D.-Y. Kim, H.-K. Kim, Sol. Energy Mater. Sol. Cells 93 1994 (2009).

33)   J.-A. Jeong, H.-K. Kim, Sol. Energy Mater. Sol. Cells 93 1801 (2009).

34)   S.-W. Cho, J.-A. Jeong, J.-H. Bae, J.-M. Moon, K.-H. Choi, S.W. Keong, N.-J. Park, J.-J. Kim, S.H. Lee, J.-W. Kang, M.-S. Yi, H.-K. Kim, Thin Solid Films 516 7881 (2008).

35)   A Indluru, T. L. Alford, J. Appl. Phys. 105, 123528 (2009).

36) A. C. Arias, M. Granstrom, D. S. Thomas, K. Petritsch, R. H. Friend, Phys. Rev. B: Condens Matter 60, 1854 (1999).

37) M. P. De Jong, L. J. Van IJzendoorn, M. J. A. De Voigt. Appl. Phys. Lett 77, 2255 (2000).

38) S. Han, W. S. Shin, M. Seo, D. Gupta, S. J. Moon, S. Yoo, Org. Electron. 10, 791 (2009).

39) M. D. Irwin, D. B. Buchholz, A. W. Hains, R P. H Chang, T. J. Marks, PNAS 105, 2783 (2008).

40) V. Shrotriya, G. Li, Y. Yao, C. W. Chu, Y. Yang, Appl. Phys. Lett. 10, 073508 (2006).

Chapter 2

1) P. W. Atkins, *Physical Chemistry;* Oxford University Press: Oxford, 1994

2) H. Hoppe, N. S. Sariciftci, J. Mater. Res.19, 1924 (2004).

3) S. Gunes, H. Neugebauer, N. S. Sariciftci, Chem. Rev. 707, 1324 (2007).

4) V. Coropceanu, J. Cornil, D. A. da Silva Filho, Y. Olivier, R. Silbey, J.-L. Bredas, Chem. Rev. 107, 926 (2007).

5) C. D. Dimitrakopoulos, P. R. L. Malenfant, Adv. Mater. 14, 99 (2002).

6) B. Singh, N. S. Sariciftci, Ann. Rev. Mater. Res. 36, 199 (2006)

7) D. B. Mitzi, J. Mater. Chem. 14, 2355 (2004)

8) C. Kittel, *Introduction to Solid State Physics, 8th ed*.; Wiley: New York, 2005.

9) H. Hoppe, N. S. Sariciftci, D. Meissner, Mol. Cryst. Liq. Cryst. 385, 113 (2002).

10) G. D. Scholes, G. Rumbles, Nat.Mater. 5, 683 (2006).

11) M. Pope, C. E. Senberg, Electronic Processes in Organic Crystals and Polymers; Oxford University Press, Inc.New York, 2002.

12) J.J.M. Halls, K. Pichler, R.H. Friend, S.C. Moratti, A.B. Holmes. Appl. Phys. Lett. 68, 3120 (1996).

13) T. Stubinger, W. Brutting, J. Appl. Phys. 90, 3632 (2001).

14) R. A. Street, Appl. Phys. Lett. 93, 133308 (2008).

15)   G. Yu and A. J. Heeger , J. Appl. Phys. 78, 4510 (1995)

16)   S. Shaheen, C. Brabec, and N. S. Sariciftci, Appl. Phys. Lett. 78, 841 (2001).

17)   J. Xue, S. Uchida, B. Rand, and S. Forrest, Appl. Phys. Lett. 84, 3013 (2004)

18)   M. Jorgensen and F. Krebs, J. Org. Chem. 69, 6688 (2004)

19)   A. M. Ramos, M. T. Rispens, J. K. J. van Duren, J. C. Hummelen, R. A. J. Janssen, J. Am. Chem. Soc. 123, 6714 (2001).

20)   D. Beljonne, J. Am. Chem. Soc. 125, 8625 (2003)

21)   R. A. J. Janssen, J. Am. Chem. Soc. 126, 10611 (2004)

22)   E. W. Meijer, J. Am. Chem. Soc. 126, 10021 (2004)

23)   E. W. Meijer, J. Am. Chem. Soc. 127, 11763 (2005)

24)   J. Xue, S. Uchida, B. P. Rand, and S. Forrest, Appl. Phys. Lett. 85, 5757 (2004)

25)   S. J. Fonash, *Solar Cell Device Physics*, 2nd ed.; Academic Press: Burlington, 2010.

26)   J. Nelson, *The Physics of Solar Cells*; Imperial College Press: London, 2003.

27)   W. Cai, X. Gong, Y. Cao, Sol. Energy Mater. Sol. Cells, 94, 114 (2010).

28)   B. P. Rand, D. P. Burk, S. R. Forrest, Phys. Rev. B 75, 115327 (2007).

29)   J Peet, A. J. Heeger, G. C. Bazan, Acc. Chem. Res. 42, 1700 (2009).

30)   A. Moliton, J.-M. Nunzi, Polym. Int. 55, 583 (2006).

31)   S Das, T. L. Alford, J. Appl. Phys. 116, 044905 (2014).

Chapter 3

1)   B. O'Regan, M. Gratzel, Nature 352, 737 (1991).

2)   F. C. Krebs, Solar Energy Materials and Solar Cells 93, 394 (2009).

3)   J. Ouyang, C.-W. Chu, F.-C. Chen, Q. Xu, Y. Yang, Advanced Functional Materials 15 203 (2005).

4)   N. S. Sariciftci, L. Smilowitz, A. J. Heeger,F. Wudl, Science 258, 1474 (1992).

5)   H. Hoppe, N. S. Sariciftci, Journal of Materials Research 19, 1924 (2004).

6) H. Spanggaard, F. C. Krebs, Solar Energy Materials and Solar Cells 83, 125 (2004).

7) M. K. Nazeeruddin, A. Kay, I. Rodicio, R. Humphry-Baker, E. Muller, P. Liska, N. Vlachopoulos, M.Gratzel, Journal of the American Chemical Society 115, 6382 (1993).

8) Y. Lin, Y. Li, X. Zhan, Chemical Society Reviews 41, 4245 (2012).

9) C. J. Brabec, N. S. Sariciftci, J. C. Hummelen, Advanced Functional Materials 11, 15 (2001).

10) F. C. Krebs, Organic Electronics 10, 761 (2009).

11) J. Y. Kim, K. Lee, N. E. Coates, D. Moses, T.-Q. Nguyen, M. Dante, A. J. Heeger, Science 317, 222 (2007).

12) M. T. Dang, L. Hirsch, G. Wantz, Advanced Materials 23, 3597 (2011).

13) M. S. A. Abdou, F. P. Orfino, Y. Son, S. Holdcroft, Journal of American Chemical Society 119, 4518 (1997).

14) S. Gunes, H. Neugebauer, N. S. Sariciftci, Chemical Reviews, 107 1324 (2007).

15) Z. Liang, Q. Zhang, O. Wiranwetchayan, J. Xi, Z. Yang, K. Park , C. Li ,G. Cao, Advanced Functional Materials 22, 2194 (2012).

16) M. Jorgensen, K. Normann, F. C. Krebs, Solar Energy Materials and Solar Cells, 92, 686 (2008).

17) P. Chen, Y. Li, X. Zhan, Nanotechnology, 24, 484008 (2013).

18) H. Ma, H. L. Yip, F. Huang, A. K.-Y. Jen, Advanced Functional Materials, 20, 1371 (2010).

19) L. A. Majewski, J. W. Kingsley, C. Balocco, A. M. Song, Applied Physics Letters, 88, 222108 (2006).

20) C. C. Hsiao, C. H. Chang, M. C. Hung, N. J. Yang, S. A. Chen, Applied Physics Lett. 86, 223505 (2005).

21) J. S. Kim, J. H. Park, J. H. Lee, J. Jo, D. Y. Kim, K. Cho, Applied Physics Letters, 91, 112111 (2007).

22) S. K. Hau, H. L. Yip, O. Acton, N. S. Baek, H. Ma, A. K.-Y Jen, Journal of Materials Chemistry, 18, 5113 (2008).

23) K. Yamamoto, S. Ochiai, X. Wang, Y. Uchida, K. Kojima, A. Ohashi, T. Mizutani, Thin Solid Films, 516, 2695 (2008).

24)   S. Obata, Y. Shimoi, Physical Chemistry Chemical Physics, 15 9265 (2013).

Chapter 4

1)   N. S. Sariciftci, L. Smilowitz, A. J. Heeger, F. Wudl, Science 258, 1474 (1992).

2)   F. C. Krebs, Sol. Energy Mater. Sol. Cells 93, 394 (2009).

3)   J. Ouyang, C.-W. Chu, F.-C. Chen, Q. Xu, Y. Yang, Adv. Funct. Mater. 15, 203 (2005).

4)   B. ORegan, M. Gratzel, Nature 352, 737 (1991).

5)   P. Dutta, Y. Xie, M. Kumar, M. Rathi, P. Ahrenkiel, D. Galipeau, Q. Qiao, V. Bommisetty, J. Photonics Energy 1, 011124 (2011).

6)   H. Spanggaard, F. C. Krebs, Sol. Energy Mater. Sol. Cells 83, 125 (2004).

7)   M. K. Nazeeruddin, A. Kay, I. Rodicio, R. Humphry-Baker, E. Muller, P. Liska, N. Vlachopoulos, M.Gratzel, J. Am. Chem. Soc. 115, 6382 (1993).

8)   Y. Lin, Y. Li, X. Zhan, Chem. Soc. Rev. 41, 4245 (2012).

9)   H.-K. Park, J.-W. Kang, S.-I. Na, D.-Y. Kim, H.-K. Kim, Sol. Energy Mater. Sol. Cells 93, 1994 (2009).

10)   Y.-Y. Choi, H.-K. Kim, H.-W. Koo, T. -W. Kim, S.-N. Lee, J. Vac. Sci. Technol. A 29, 061502 (2011).

11)   L.M. Chen, Z. Hong, G. Li, Y. Yang, Adv. Mater. 21 (2009) 1434–1449.

12)   F. Yang, S.R. Forrest, ACS Nano 2, 1022 (2008).

13)   C. J. Brabec, N. S. Sariciftci, J. C. Hummelen, Plastic solar cells, Adv. Funct. Mater. 11, 15 (2001).

14)   F.C. Krebs, Org. Electron. 10, 761 (2009).

15)   J. Y. Kim, K. Lee, N. E. Coates, D. Moses, T.-Q. Nguyen, M. Dante, A. J. Heeger, Science 317, 222 (2007).

16)   M. T. Dang, L. Hirsch, G. Wantz, Adv. Mater. 23, 3597 (2011).

17)   T. -W. Lee, Y. Chung, Adv. Funct. Mater. 18, 2246 (2008)

18)   A. Yakimov, S. R. Forrest, Appl. Phys. Lett. 80, 1667 (2002)

19) M. Jorgensen, K. Normann, F. C. Krebs, Sol. Energy Mater. Sol. Cells 92, 686 (2008).

20) M. P. De Jong, L. J. Van IJzendoorn, M. J. A. De Voigt, Appl. Phys. Lett. 77, 2255 (2000).

21) M. D. Irwin, D.B. Buchholz, A.W. Hains, R.P.H. Chang, T.J. Marks, PNAS 105, 2783 (2008).

22) K. Takanezawa, K. Tajima, K. Hashimoto, Appl. Phys. Lett. 93, 063308 (2008).

23) D. Y. Kim, G. Sarasqueta, F. So, Sol. Energy Mater. Sol. Cells 93, 1452 (2009).

24) S. Inudo, M. Miyake, T. Hirato, Phys. Status Solidi A 210, 2395 (2013).

25) D. A. Keen, S. Hull, J. Phys. Condens. Matter 7, 1793 (1995).

26) Y. Zhou, T. Taima, T. Miyadera, T. Yamanari, M. Kitamura, K. Nakatsu, Y. Yoshida, Nano Lett. 12, 4146 (2012).

27) S. Shao, J. Liu, J. Zhang, B. Zhang, Z. Xie, Y. Geng, L. Wang, ACS Appl. Mater. Interfaces 4, 5704 (2012).

28) P. M. Sirimanne, M. Rusop, T. Shirata, T. Soga, T. Jimbo, Chem. Phys. Lett. 366, 485 (2002).

29) C. H. Cheng, J. Wang, G. T. Du, S. H. Shi, Z. J. Du, Z. Q. Fan, J. M. Bian, M. S. Wang, Appl. Phys. Lett. 97, 083305 (2010).

Chapter 5

1) C. J. Brabec, N. S. Sariciftci, J. C. Hummelen, Adv. Funct. Mater. 11, 15 (2001).

2) F. C. Krebs, Sol. Energy Mater. Sol. Cells 93, 394 (2009).

3) H. Y. Chen, J. Hou, S. Zhang, Y. Liang, G. Yang, Y. Yang, L. Yu, Y. Wu, G. Li, Nat. Photonics 3, 649 (2009).

4) J. Y. Kim, K. Lee, N. E. Coates, D. Moses, T.-Q. Nguyen, M. Dante, A. J. Heeger, Science 317, 222 (2007).

5) H. Ma, H. L. Yip, F. Huang, A. K.-Y. Jen, Adv. Funct. Mater. 20, 1371 (2010).

6) Z. He, C. Zhong, S. Su, M. Xu, H. Wu, Y. Cao, Nat. Photon.6, 591 (2012).

7) G. Li, R. Zhu, Y. Yang, Polymer solar cells, Nat. Photonics 6, 153 (2012).

8)   H. Spanggaard, F. C. Krebs, Sol. Energy Mater. Sol. Cells 83, 125 (2004).

9)   S.-I. Na, S.-S. Kim, J. Jo, D.-Y. Kim, Adv. Mater. 20, 4061 (2008).

10)   Y. J. Cho, J. Y. Lee, B. D. Chin, S. R. Forrest, Org. Electron. 14, 1081 (2013).

11)   C. J. Brabec, S. E. Shaheen, C. Winder, N. S. Sariciftci, P. Denk, Appl. Phys. Lett. 80, 1288 (2002).

12)   C. M. Ramsdale, J. A. Barker, A. C. Arias, J. D. MacKenzie, R. H. Friend, N. C. Greenham, J. Appl. Phys. 92, 4266 (2002).

13)   S. Khodabakhsh, B. M. Sanderson, J. Nelson, T. S. Jones, Adv. Funct. Mater. 16, 95 (2006).

14)   J. S. Kim, J. H. Park, J. H. Lee, J. Jo, D. Y. Kim, K. Cho, Appl. Phys. Lett. 91, 112111 (2007).

15)   M. -Y. Chang, C. -S. Wu, Y. -F. Chen, B. -Z. Hsieh, W. -Y. Huang, K. -S. Ho, T. -H. Hsieh, Y. -K. Han, Org. Electron 9, 1136 (2008).

16)   J. Subbiah, D. Y. Kim, M. Hartel, F. So, Appl. Phys. Lett. 96, 063303 (2010).

17)   M. T. Dang, L. Hirsch, G. Wantz, Adv. Mater. 23, 3597 (2011).

18)   W. C. H. Choy (ed.), *Organic Solar Cells: Materials and Device Physics* (Springer, London, 2013), pp 5.

19)   A. C. Arias, M. Granstrom, D. S. Thomas, K. Petritsch, R. H. Friend, Phys. Rev. B 60, 1854 (1999).

20)   L. S. C. Pingree, B. A. MacLeod, D. S. Ginger, J. Phys. Chem. C 112, 7922 (2008).

21)   H. Yan, P. Lee, N. R. Armstrong, A. Graham, G. A. Evmenenko, P. Dutta, T. J. Marks, J. Am. Chem. Soc. 127, 3172 (2005).

22)   M. Jørgensen, K. Norrman, F. C. Krebs, Sol. Energy Mater. Sol. Cells 92, 686 (2008).

23)   E. Voroshazi, B. Verreet, A. Buri, R. Muller, D. Di Nuzzo, P. Heremans, Org. Electron. 12, 736-744 (2011).

24)   V. Shrotriya, G. Li, C.-W. Chu, Y. Yang, Appl. Phys. Lett. 88, 073508 (2006).

25)   M.D. Irwin, B. Buchholz, A.W. Hains, R.P.H. Chang, T.J. Marks, PNAS 105, 2783 (2008).

26)   M. Vasilopoulou, A. Soultati, D. G. Georgeiadou, T. Stergiopoulos, L. C. Palilis, S. Kennou, N. A. Stathopoulos, D. Davazoglou, P. Argitis, J. Mater. Chem. A. 2, 1738 (2014).

27)   W. Wei, X. Mao, L. A. Ortiz, D. R. Sadoway, J. Mater. Chem. 21, 432 (2011).

28)   U. K. Barik, S. Srinivasan, C. L. Nagendra, A. Subrahmanyam, Thin Solid Films 429, 129 (2003).

29)   G. Li, V. Shrotriya, Y. Yao, Y. Yang, J. Appl. Phys. 98, 043704 (2005).

30)   K. -S. Lee, J. -W. Lim, H. -K. Kim, T. L. Alford, G. E. Jabbour, Appl. Phys. Lett. 100, 213302 (2005).

31)   V. Shrotriya, J. Ouyang, R. J. Tseng, G. Li, Y. Yang, Chem. Phys. Lett. 411, 138 (2005).

32)   N. Koide, A. Islam, Y. Chiba, L. Han, J. Photochem. Photobiol. A 182, 296 (2006).

Chapter 6

1)   H. Han, N. D. Theodore, T. L. Alford, J. Appl. Phys. 103, 013708 (2008).

2)   K. Sivaramakrishnan, T. L. Alford, Appl. Phys. Lett. 94, 052104 (2009).

3)   S. Vedraine, A. E. Hajj, P. Torchio, B. Lucas, Org. Electron. 14, 1122 (2013).

4)   Y. C. Han, M. S. Lim, J. H. Park, K. C. Choi, Org. Electron. 14, 3437 (2013).

5)   A. C. Arias, M. Granstrom, D. S. Thomas, K. Petritsch, R. H. Friend, Phys. Rev. B 60, 1854 (1999).

6)   M. P. De Jong, L. J. Van IJzendoorn, M. J. A. De Voigt, Appl. Phys. Lett. 77, 2255 (200).

7)   S. Han, W. S. Shin, M. Seo, D. Gupta, S. J. Moon, S. Yoo, Org. Electron. 10, 791 (2009).

8)   M. D. Irwin, D. B. Buchholz, A. W. Hains, R P. H Chang, T. J. Marks, PNAS 105, 2783 (2008).

9)   V. Shrotriya, G. Li, Y. Yao, C. W. Chu, Y. Yang, Appl. Phys. Lett. 10, 073508 (2006).

10)   T. Muller and H. Nienhaus, J. Appl. Phys. 93, 924 (2003).

11)   R. Koch, J. Phys.: Condens. Matter 6, 9519 (1994).

12) P. Bieganski, Vacuum 74, 211 (2004).

13) G. J. Haacke, J. Appl. Phys. 47, 4086 (1976).

Chapter 7

1) F. C. Krebs, N. Espinosa, M. Hösel, R. R. Søndergaard, M. Jørgensen, Adv. Mater. 26, 29 (2014).

2) C. J. Brabec, N. S. Sariciftci, C. Hummelen, Adv. Funct. Mater. 11, 15 (2001).

3) H. Spanggaard, F. C. Krebs, Sol. Energy Mater. Sol. Cells, 83, 125 (2004).

4) H. Hoppe, N. S. Sariciftci, J. Mater. Res. 19, 1924 (2004).

5) M. T. Dang, L. Hirsch, G. Wantz, Adv. Mater. 23, 3597 (2011)

6) S. Guo, C. Brandt, T. Andreev, E. Metwalli, W. Wang, J. Pelich, P. Muller-Buschbaum, ACS Appl. Mater. Interfaces 6, 17902 (2014).

7) F. C. Krebs, Sol. Energy Mater. Sol. Cells, 93, 394 (2009).

8) F. C. Krebs, Org. Electron. 2009, 10, 761 (2009).

9) J. Y. Kim, K. Lee, N. E. Coates, D. Moses, T. –Q. Nguyen, M. Dante, A. J. Heeger, Science 317, 222 (2007).

10) M. T. Dang, L. Hirsch, G. Wantz, Adv. Mater. 23, 3597 (2011).

11) L. M. Chen, Z. Hong, G. Li, Y. Yang, Adv. Mater. 21, 1434 (2009).

12) C. J. Schaffer, C. M. Palumbiny, M. A. Niedermeier, C. Jendrzejewski, G. Santoro, S. V. Roth, P. Muller-Buschbaum, Adv. Mater. 25, 6760 (2013).

13) U. Vongsaysy, D. M. Bassani, L. Servant, B. Pavageau, G. Wantz, H. J. Aziz, J. Photon. Energy. 4, 040998 (2014).

14) P. Dutta, Y. Xie, M. Kumar, M. Rathi, P. Ahrenkiel, D. Galipeau, Q. Qiao, V. Bommisetty, J. Photon. Energy. 1 011124 (2011).

15) U. Vongsaysy, B. Pavageau, G. Wantz, D. M. Bassani, L. Servant, H. Aziz, Adv. Energy Mater. 4, 1300752 (2014).

16) M. Jorgensen, K. Normann, F. C. Krebs, Sol. Energy Mater. Sol. Cells, 92, 686 (2008).

17) R. Steim, F. R. Kogler, C. J. Brabec, J. Mater. Chem., 20, 2499 (2010).

18) H. Xin, S. Subramaniyan, T.-W. Kwon, S. Shoaee, J. R. Durrant, S. A. Jenekhe, Chem. Mater. 24, 1995 (2012)

19) H.-Y. Chen, J. Hou, S. Zhang, Y. Liang, G. Yang, Y. Yang, L. Yu, Y. Wu, G. Li, Nat. Photonics. 3, 649 (2009).

20) J. -Y. Lee, S.–H. Kim, I. -S. Song, D.-K. Moon, D.; J. Mater. Chem. 21, 16480 (2011).

21) H. Ma, H. -L. Yip, F. Huang, A. K.-Y. Jen, Adv. Funct. Mater. 20, 1371 (2010).

22) L. -M. Chen, Z. Xu, Z. Hong, Y. Yang, J. Mater. Chem. 20, 2575 (2010).

23) B. Bob, T.-B. Song, C.-C. Chen, Z. Xu, Y. Yang, Chem. Mater. 25, 4725 (2013).

24) Z. Lin, C. Jiang, C. Zhu, Z. Zhang, ACS Appl. Mater. Interfaces, 5, 713 (2013).

25) Y. Sun, J. H. Seo, C. J. Takacs, J. Seifter, A. J. Heeger, Adv. Mater. 23, 1679 (2011).

26) Y. Ka, E. Lee, S. Y. Park, J. Seo, D.-G. Kwon, H. H. Lee, Y. Park, Y. S. Kim, C. Kim, Org. Electron. 14, 100 (2013).

27) D. Liu, T. L. Kelly, Nat. Photonics 2014, 8, 133 (2014).

28) K. Sarkar, E. V. Braden, S. Pogorzalek, S. Yu, S. V. Roth, P. Muller-Buschbaum, ChemSusChem. 7, 2140 (2014).

29) T. Minami, Semicond. Sci. Technol. 20, S35 (2005).

30) T. Minami, H. Nanto, S. Takata, Jpn. J. Appl. Phys. 23, L280 (1984).

31) Y. Cheng, L. Cao, G. He, G. Yao, X. Song, Z. Sun, J. Alloys Compd. 608, 85 (2014).

32) S. Major, K. L. Chopra, Sol. Energy Mater. 17, 319 (1988).

33) R. Kaur, A. V. Singh, R. A. Mehra, Phys. Stat. Sol. (a) 202, 1053 (2005).

34) R. D. Chandra, M. Rao, K. Zhang, R. R. Prabhakar, C. Shi, J. Zhang, S. G. Mhaisalkar, N. Mathews, ACS Appl. Mater. Interfaces 2014, 6, 773−777.

35) T. Minami, H. Sato, H. Nanto, S. Takata, Jpn. J. Appl. Phys. 24, L781 (1985).

36) J. -H. Lee, K.-H. Ko, B.-O. Park, J. Cryst. Growth, 247, 119 (2003).

37) J. M. Cho, S. -W. Kwak, H. Aqoma, J. W. Kim, W. S. Shin, S.-J. Moon, S.-Y. Jang, J. Jo, Org. Electron. 15, 1942 (2014).

38) Y. Kato, M. –C. Jung, M. V. Lee, Y. Qi, Org. Electron. 15, 721 (2014).

39) K. Ip, B. P. Gila, A. H. Onstine, E. S. Lambers, Y. W. Heo, K. H. Baik, D. P. Norton, S. J. Pearton, S. Kim, J. R. LaRoche, ; F. Ren, Appl. Phys. Lett. 84, 5133 (2004).

40) Q. Bao, X. Liu, Y. Xia, F. Gao, L.-D. Kauffmann, O. Margeat, J. Ackermann, M. Fahlman, J. Mater. Chem. A, 2, 17676 (2014)

41) H. P. Klug, L. E. Alexander, *X-ray Diffraction Procedures for Polycrystalline and Amorphous Materials*. Wiley, New York, 1974

42) C. Jiang, R. R. Lunt, P. M. Duxbury, P. P. Zhang, RSC Adv.4, 3604 (2014).

43) Q. Yu, W. Fu, C. Yu, H. Yang, R. Wei, Y. Sui, S. Liu, Z. Liu, M. Li, G. Wang, C. Shao, Y. Liu, G. Zou, J. Phys. D: Appl. Phys. 40, 5592 (2007).

44) X. Han, K. Han, M. Tao, J. Electrochem. Soc. 157, H593-H597 (2010).

45) J. Weickert, R. B. Dunbar, H. C. Hesse, W. Wiedemann, L. Schmidt-Mende, Adv. Mater. 23, 1810 (2011).

APPENDIX A

LIST OF ABBREVIATIONS

A	electron acceptor
AFM	atomic force microscopy
AM	air mass
BHJ	bulk-heterojunction
CB	conduction band
D	electron donor
EA	electron affinity
EBL	exciton blocking layer
ETL	electron transport layer
EQE	external quantum efficiency
FESEM	field emission scanning electron microscopy
FF	fill factor
FOM	figure of merit
FTO	fluorine doped tin oxide
HBL	hole blocking layer
HOMO	highest occupied molecular orbital
HMDS	1,1,1,3,3,3-hexamethyldisilazane
HTL	hole transport layer
ITO	indium tin oxide
LED	light emitting device
LUMO	lowest unoccupied molecular orbital
MEH	2-methoxy-5-(2-ethyl-hexyloxy)
OSC	organic solar cells
OPV	organic photovoltaics
OLED	organic light emitting diode
PCE	power conversion efficiency
PEDOT	poly(ethylene dioxythiophene)
PPV	poly(*para*-phenylene vinylene)
PSS	polystyrenesulfonate
P_3HT	poly (3-hexylthiophene)
$PC_{61}BM$	[6,6]-phenyl-C61-butyric acid methyl ester
TCE	transparent composite electrode
VB	valence band
XRD	x-ray diffraction
XPS	x-ray photoelectron spectroscopy
YZO	yttrium doped zinc oxide

APPENDIX B

LIST OF PUBLICATIONS

Journal Publications

1. *Optimization of the zinc oxide electron transport layer in $P_3HT:PC_{61}BM$ based solar cells by annealing and yttrium doping,* **Sayantan Das** and T. L. Alford, *RSC Advances,* **5** 45586 (2015).

2. *$P_3HT:PC_{61}BM$ based solar cells employing solution processed copper iodide as the hole transport layer*, **Sayantan Das,** Jea-Young Choi and T. L. Alford, *Solar Energy Materials and Solar Cells,* **255** 98 (2015).

3. *Improved efficiency of P3HT:PCBM solar cells by incorporation of silver oxide interfacial layer,* **Sayantan Das** and T. L. Alford *Journal of Applied Physics*, **116**, 044905 (2014)

4. *Effect of Ag layer thickness on the electrical transport and optical properties of ZnO/Ag/MoOx transparent composite electrodes and their use in P3HT:PC61BM-based organic solar cells* **Sayantan Das**, Hyung Woo Choi and T. L. Alford *Mater. Lett* **113** 183 (2014)

5. *Enhanced performance of polymer solar cells ($P3HT:PC_{61}BM$) by incorporation of silver oxide functional layer,* **Sayantan Das,** Hyung Woo Choi and T. L. Alford *Materials Letters* **133** 183 (2014)

6. *Self-assembled monolayer modified ITO in $P_3HT:PC_{61}BM$ organic solar cells with improved efficiency*, **Sayantan Das**, Joseph Joslin and T. L. Alford, *Solar Energy Materials and Solar Cells,* **124** 98 (2014).

7. *Enhanced conductivity of Y-doped ZnO thin films by incorporation of multiple walled carbon nanotubes*, **Sayantan Das**, R. N. P. Vemuri and T. L. Alford *Thin Solid Films*, **527** 92 (2013)

8. *Advances in 3D printing of functional nanomaterials and roll-to-roll technologies and their applications* (review article)*,* Jae-Young Choi, **Sayantan Das**, N. David Theodore, Inho Kim, Christiana Honsberg, Hyung Woo Choi, T. L. Alford, ECS Journal of Solid State Science and Technology, **4** P3001-P3009 (2015)

9. *Thermal stability of copper on Te-Ti films,* Benjamin Roos, **Sayantan Das** and T. L. Alford *Mater. Lett* **113** 100 (2013)

10. *Microwave assisted growth of copper germanide thin films at very low temperatures,* **Sayantan Das** and T. L. Alford *Applied Physics. Letters* **103** 094104 (2013)

11. *Structural and optical properties of Ag-doped copper oxide thin films on polyethylene napthalate substrate prepared by low temperature microwave annealing,* **Sayantan Das** and T. L. Alford *Journal of Applied Physics.* **113** 244905 (2013)

12.	*Effect of dopant activation via low temperature microwave annealing of ion implanted silicon,* **Sayantan Das** and T. L. Alford *Applied Physics. Letters* **103** 192103 (2013)

13.	*Enhanced electrical performance of Ag-Cu thin films after low temperature microwave processing,* **Sayantan Das**, R. N. P. Vemuri and T. L. Alford *J. Vac. Sci. Technol. B* **31** 011204 (2013)

14.	Microwave assisted growth of copper germanide thin films at very low temperatures, **Sayantan Das** and T. L. Alford *Applied Physics Letters.* **103** 094104 (2013)

15.	*Microwave assisted low temperature encapsulation of Ag films by Cu reactions using Ag-Cu structures,* **Sayantan Das** and T. L. Alford *Mater. Lett* **89** 163 (2012)

Patent Applications Filed

1.	*Thin film devices and low temperature process to make thin film devices*, U.S. Patent Application No. US 2014/0367858 A1, Sayantan Das and T. L. Alford.

2.	*Thin Film Devices and Methods for Preparing Thin Film Devices*, U.S. Patent Application No. US 2014/0272396 A1, T. L. Alford and Sayantan Das.